EXPERIMENTAL CHARACTERIZATION AND MULTI-SCALE MODELING OF TWO-DIMENSIONAL WOVEN COMPOSITES

A THESIS SUBMITTED TO
THE GRADUATE SCHOOL OF NATURAL AND APPLIED SCIENCES
OF
MIDDLE EAST TECHNICAL UNIVERSITY

BY

NUSRET CEM DİYARBAKIR

IN PARTIAL FULFILLMENT OF THE REQUIREMENTS
FOR
THE DEGREE OF MASTER OF SCIENCE
IN
METALLURGICAL AND MATERIALS ENGINEERING

JANUARY 2025

Approval of the thesis:

EXPERIMENTAL CHARACTERIZATION AND MULTI-SCALE MODELING OF TWO-DIMENSIONAL WOVEN COMPOSITES

submitted by **NUSRET CEM DİYARBAKIR** in partial fulfillment of the requirements for the degree of **Master of Science** i**n Metallurgical and Materials Engineering, Middle East Technical University** by,

Prof. Dr. Naci Emre Altun

Dean, **Graduate School of Natural and Applied Sciences**

Prof. Dr. Ali Kalkanlı

Head of the Department, **Metallurgical and Materials Eng.**

Assist. Prof. Irmak Sargın

Supervisor, **Metallurgical and Materials Eng., METU**

Prof. Dr. Ercan Gürses

Co-Supervisor, **Aerospace Engineering, METU**

Examining Committee Members:

Prof. Dr. Arcan. F. Dericioğlu

Metallurgical and Materials Eng., METU

Assist. Prof. Dr. Irmak Sargın

Metallurgical and Materials Eng., METU

Prof. Dr. Ercan Gürses

Aerospace Engineering, METU

Assist. Prof. Dr. Görkem Eğemen Güloğlu

Aerospace Engineering, METU

Prof. Dr. Bora Maviş

Mechanical Engineering, Hacettepe University

Date: 07.01.2025

I hereby declare that all information in this document has been obtained and presented in accordance with academic rules and ethical conduct. I also declare that, as required by these rules and conduct, I have fully cited and referenced all material and results that are not original to this work.

Diyarbakır, Nusret Cem

Signature :

ABSTRACT

EXPERIMENTAL CHARACTERIZATION AND MULTI-SCALE MODELING OF TWO-DIMENSIONAL WOVEN COMPOSITES

Diyarbakır, Nusret Cem
Master of Science, Metallurgical and Materials Engineering
Supervisor: Assist. Prof. Dr. Irmak Sargın
Co-Supervisor: Prof. Dr. Ercan Gürses

January 2025, 111 pages

The main aim of this thesis is to predict elastic mechanical properties of woven composites by different computational approaches. To achieve this aim, the effect of different curing routes on the mechanical properties are studied experimentally and computationally. Micromechanical modeling of composites is executed within a multi-scale framework. Autoclave and out-of-autoclave (vacuum-oven) are utilized for curing experiments to observe the differences in microstructure and hence, macro properties. The microstructures are examined using optical microscopy, scanning electron microscopy, and micro X-Ray tomography. Macromechnical properties are determined using tensile and three point bending tests. Moreover, the differences in microstructure are implemented in computational models and their effect on elastic properties are evaluated. For the simulations, mean field homogenization (MFH) with Mori-Tanaka scheme and finite element homogenization are employed. Accuracy and efficiency of these simulation work are compared with experimental data for validation. Lastly, for the finite element homogenization, mesh type and convergence studies are conducted.

Keywords: Micromechanical Modeling, Woven Composites, Mean Field Homogenization, Finite Element Homogenization, Mechanical Properties

ÖZ

İKİ BOYUTLU DOKUMA KOMPOZİTLERİN DENEYSEL KARAKTERİZASYONU VE ÇOK ÖLÇEKLİ MODELLEMESİ

Diyarbakır, Nusret Cem
Yüksek Lisans, Metalurji ve Malzeme Mühendisliği
Tez Yöneticisi: Assist. Prof. Dr. Irmak Sargın
Ortak Tez Yöneticisi: Prof. Dr. Ercan Gürses

Ocak 2025, 111 sayfa

Bu tezin temel amacı, kürleme sürecindeki farklı üretim yöntemlerinin mekanik özellikler üzerindeki etkisini belirlemek ve dokuma kompozit malzemelerin elastik mekanik özelliklerini belirli hesaplamalı yaklaşımlarla tahmin etmektir. Kompozitlerin mikromekanik modellemesi çok ölçekli bir çerçeve içinde gerçekleştirilmiştir. Bu amaçla, mikro yapı ve makro özelliklerdeki farklılıkları gözlemlemek için otoklav ve otoklav dışı (vakumlu fırın) yöntemleri kullanılmıştır. Mikro yapıdaki farklılıklar optik mikroskopi, taramalı elektron mikroskobu ve mikro x-ışını tomografisi ile incelenmiştir. Makro özellikler, çekme ve üç nokta eğme testleri ile belirlenmiştir. Ayrıca, mikro yapıdaki farklılıklar malzeme modellerine uygulanmış ve bu farklılıkların elastik özellikler üzerindeki etkisi değerlendirilmiştir. Simülasyonlarda, Mori-Tanaka şemasıyla ortalama alan homojenleştirmesi (MFH) ve sonlu eleman homojenleştirmesi kullanılmıştır. Bu simülasyon çalışmalarının doğruluğu ve verimliliği deneysel verilerle karşılaştırılmış ve doğrulanmıştır. Son olarak, sonlu eleman homojenleştirmesi için meş tipi ve yakınsama çalışmaları gerçekleştirilmiştir.

Anahtar Kelimeler: Mikromekanik Modelleme, Dokuma Kompozitler, Ortalama Alan Homojenizasyonu, Sonlu Eleman Homojenizasyonu, Mekanik Özellikler

To Assoc. Prof. Dr. Caner Şimşir, with deepest respect.

ACKNOWLEDGMENTS

I would like to express my deepest gratitude to my supervisor, Assist. Prof. Dr. Irmak Sargın, and my co-supervisor, Prof. Dr. Ercan Gürses, for their invaluable guidance, advice, constructive criticism, encouragement, and insightful support throughout this research.

I also extend my heartfelt thanks to the members of the examining committee—Prof. Dr. Arcan F. Dericioğlu, Prof. Dr. Bora Maviş, and Assist. Prof. Dr. Görkem Eğemen Güloğlu—for their valuable feedback and remarks during my thesis defense.

My deepest appreciation goes to my company and teammates at ROKETSAN A.Ş., who supported me throughout the manufacturing and testing phases of my thesis, particularly Begüm Beril İncecik, Berk Çakır, Erol Cem Özgör, Furkan Melih Günay, Gökberk Demirok, Utku Olgun, Başak Demirbaş, Tayfun Vural, Berk Polat Muammer Özkorul, Ahmet Tünay, Faruk Akkaya, Deniz Doğan and Özer Özmen.

I am also sincerely grateful to my friends Onur Demircioğlu, Umutcan Gülletutan, Eren Foya, İdris Erdem, Ural Kaan Sözeri, Onur Balak, Eda Çevik, Murathan Çuğunlular, Özde Nur Özkan and Buse Ceren Görkem, for their unwavering support and camaraderie.

Special thanks are due to Simge Uzuncan and Emre Tirben from SPM Kompozit Malzemeler A.Ş. for kindly providing the materials used in this study.

I am profoundly grateful to my beloved mother, grandmother, grandfather, and all other family members who have always believed in me and supported me throughout my life. Their constant and endless love has been the foundation of my achievements.

Last but not least, I am deeply thankful to my girlfriend and future wife, İlayda Güven, who has continuously motivated me, shared my burdens, and stood by me with unwavering support in every aspect of my life. I would also like to acknowledge her parents, who have always treated me as a part of their family.

TABLE OF CONTENTS

ABSTRACT v

ÖZ vii

ACKNOWLEDGMENTS x

TABLE OF CONTENTS xi

LIST OF TABLES xiv

LIST OF FIGURES xvi

LIST OF ABBREVIATIONS xxi

CHAPTERS

1 INTRODUCTION 1

1.1 Polymer Matrix Composites 1

1.2 2D Woven Composites 3

1.3 Production and Curing Techniques of Woven Composites 6

1.4 Micromechanical Modeling of Woven Composites 7

1.4.1 Mean Field Homogenization (MFH) 7

1.4.2 Eshelby's Inclusion Problem 8

1.4.3 Mori-Tanaka MFH Scheme 9

1.5 Homogenization Using Finite Element Analysis 11

1.6 Orthotropic Material Properties 13

1.7 Aim and Motivation of the Thesis 14

2 EXPERIMENTAL WORK 17

2.1 Woven Carbon Fiber/Epoxy Prepregs Used in the Study 17
2.2 Characterization of Composite Constituents 18
2.2.1 Fiber Characterization 18
2.2.2 Resin Characterization 19
2.3 Manufacturing of Composite Laminates Using Prepreg Lay-Up Technique 24
2.3.1 Material Preparation and Lay-up Technique 24
2.3.2 Curing and Consolidation Techniques 27
2.4 Manufacturing of Coupons and Specimens 29
2.4.1 Optical Microscopy 31
2.4.2 Unidirectional Tensile Tests 33
2.4.3 3-Point Bending Tests 35
2.4.4 Density Measurements 36
2.4.5 Fiber Content Measurements 37
2.4.6 Void Content Measurements 38
2.4.7 Scanning Electron Microscopy (SEM) 39
2.4.8 Micro Computed Tomography (Micro-CT) 39
2.4.9 Glass Transition Temperature Measurements using Rotational Rheometer Analysis with Torsion Module 40
3 RESULTS AND DISCUSSION 41
3.1 Constituent Characterization 42
3.2 Microstructural Investigation 44
3.2.1 Microstructural Investigation Using Optical Microscopy 44
3.2.2 Fiber Diameter Measurements by SEM 48

3.2.3 Void Analysis Using Micro-CT 50
3.3 Composite Characterization 57
3.3.1 Physical Properties of Composites 57
3.3.2 Tensile Properties of Composites 59
3.3.3 Flexural Properties of Composites 62
3.3.4 Rheological Behavior of Composites 65
4 MODELING, SIMULATIONS AND VALIDATION 67
4.1 Procedure for Mean Field Homogenization Technique 68
4.2 Procedure for Finite Element Homogenization Technique 71
4.3 Modeling and Simulation Work for Plain Woven Composites 73
4.3.1 Implementation of Voids to Material Models 76
4.3.2 Mesh Convergence Study 78
4.3.3 Three-Point Bending Simulations for Plain Woven Composites ... 80
4.4 Modeling and Simulation Work for Twill Woven Composites 85
4.4.1 Implementation of Voids to Material Models 88
4.4.2 Three-Point Bending Simulations for Twill Woven Composites ... 89
5 CONCLUSION 91
REFERENCES 93
APPENDICES 101
A. Statistics about void information in composite laminates 101
B. Integration Parameters for MFH Analyses 103
C. Yarn Cross Section Images 104

LIST OF TABLES

Table 2-1: Mechanical and physical properties of carbon fiber 18
Table 2-2: Dimensions of epoxy resin tensile coupons in accordance with ASTM D638-14 Type I 21
Table 2-3: Woven fabric properties used in this study 25
Table 2-4: The stacking sequences of laminates. Dashed line represents mid-plane of laminates 25
Table 2-5: Prepared coupons/specimens for further composite characterization 30
Table 3-1: Ultimate tensile strength, strain, elastic modulus and Poisson's ratio values for epoxy resin 43
Table 3-2: Density measurements for epoxy resin 44
Table 3-3: Warp and weft widths for both fabrics 45
Table 3-4: Warp and weft dimensions for plain woven fabric composites 48
Table 3-5: Warp and weft dimensions for twill woven fabric composites 48
Table 3-6: Density, fiber weight and fiber volume fraction measurements of composites 57
Table 3-7: Void content measurements for laminates 58
Table 3-8: Tensile test results for vacuum oven cured plain woven composite 59
Table 3-9: Tensile test results for autoclave cured plain woven composite 59
Table 3-10: Tensile test results for vacuum oven cured twill woven composite 61
Table 3-11: Tensile test results for autoclave cured twill woven composite 61
Table 3-12: Three-point bending test results for vacuum oven cured plain woven composite 63
Table 3-13: Three-point bending test results for autoclave cured plain woven composite 63
Table 3-14: Three-point bending test results for vacuum oven cured twill woven composites 64

Table 3-15: Three-point bending test results for autoclave cured twill woven composites 65
Table 4-1: Material models and parameters for analysis 68
Table 4-2: Material, yarn and geometry properties for plain woven composites ... 73
Table 4-3: Computed yarn properties and geometric parameters for vacuum-oven and autoclave cured plain woven composites 75
Table 4-4: Simulation and experimental results for V-P composite 75
Table 4-5: Simulation and experimental results for A-P composite 76
Table 4-6: V-P simulation results with voids included 77
Table 4-7: A-P simulation results with voids included 77
Table 4-8: Variation of mechanical properties with different meshes for V-P composites 79
Table 4-9: Material, yarn and geometry properties for twill woven composites 85
Table 4-10: Computed yarn properties and geometric parameters for V-T and A-T composites 86
Table 4-11: Simulation and experimental results for V-T composite 87
Table 4-12: Simulation and experimental results for A-T composite 87
Table 4-13: V-T simulation results with voids included 88
Table 4-14: A-T simulation results with voids included 88

LIST OF FIGURES

Figure 1-1: 3D weave examples: a) 3D through-thickness angle-interlock woven composites, b) 3D layer-to-layer angle-interlock woven composites, c) 3D through-thickness orthogonal interlock woven composites d) 3D layer-to-layer orthogonal-interlock woven composites. [6]..... 3
Figure 1-2: Schematics of different woven fabrics (a) plain weave, (b) basket weave, (c) 3×1 crowfoot, (d) 8-harness satin weave, (e) 2×2 twill weave (f) leno weave [4] 4
Figure 1-3: Definition of yarn crimp angle using geometrical model created by Peirce [16] 5
Figure 1-4: Micro-macro transition. The upper left represents microscopic scale, the upper right represents macroscopic scale, and the transition between these scales is obtained by RVE (representative volume element) [22]..... 8
Figure 1-5: Solution to the Eshelby's inclusion problem steps, sequence of imaginary cutting an ellipsoidal from an infinite material, straining it and welding it back to its place [24]..... 9
Figure 1-6: Mori Tanaka MFC scheme simple interpretation [24]. 11
Figure 1-7: Homogenization using finite element approach [57]. 12
Figure 2-1: SEM images of composite cross section for fiber diameter measurements. 19
Figure 2-2: Recommended curing cycle of VTP DA-100 epoxy resin 20
Figure 2-3: Technical drawing of epoxy resin coupons in accordance with ASTM D638-14 Type I. Dimensions are given in Table 2. [55]..... 20
Figure 2-4: Manufactured epoxy resin coupons before tensile testing..... 22
Figure 2-5: DIC specimen preparation and testing steps. Painting of the specimen surfaces are shown in (a) and (b). Specimen surface after black paint application is shown in (c). Mounted specimen is shown in (d). Light and position settings are shown in (e) and (f). 23
Figure 2-6: Tensile failure modes of the coupons 23

Figure 2-7: Vacuum bagging procedure. (a) Application of sealants to the edges of the plate and non-perforated release film. (b) and (c) Application of release films and peel ply. (d) and (e) Application of breather fabric and vacuum bag. (f) Completion of vacuuming..... 26
Figure 2-8: Schematic of composite vacuum bagging technique and consumables used 27
Figure 2-9: Different curing media for the laminates: (a) vacuum oven, (b) autoclave 28
Figure 2-10: -690 mmHg (~0.90 atm) pressure drop is measured for the laminates in vacuum oven and autoclave. 28
Figure 2-11: Removal of auxiliary materials such as the vacuum bag, peel ply, release film, and breather fabric, followed by obtaining the cured laminates 29
Figure 2-12: Precise cutting of composite plates into coupons and specimens..... 30
Figure 2-13: Prepared specimens. (a) surface to be investigated (b) rear surface and marking 31
Figure 2-14: Microstructural images of cross sections for (a) plain woven fabric/epoxy composite from warp direction (b) plain woven fabric/epoxy composite from weft direction (c) twill woven fabric/epoxy composite from warp direction (d) twill woven fabric/epoxy composite from weft direction. 32
Figure 2-15: Microstructural images of prepreg materials from top view for (a) plain woven fabric/epoxy composite (b) twill woven fabric/epoxy composite..... 33
Figure 2-16: Tabbing steps (a) preparation of adhesive and tabs. (b) and (c) grinding of tabs and composite plates (d) and (e) applying pressure to consolidate adhesive before curing in oven 34
Figure 2-17: Unidirectional tensile testing of composite coupons (a) tensile test coupons (b), (c) and (d) tensile test and strain measurement setup (e) *A-T composite coupons* and (f) *A-P composite* coupons after completion of tests..... 35
Figure 2-18: Bending test specimens and setup. (a) *V-P* specimens before the test (b) *V-P* specimens after the test (c) test fixture and setup 36

Figure 2-19: Application steps of fiber content measurement (a), (b) and (c) are remaining fibers after epoxy resin is completely dissolved (d), (e) and (f) are washing steps of the carbon fiber 38
Figure 3-1: Stress-strain curves for epoxy resin tensile tests 42
Figure 3-2: Yarn width measurements for (a) warp yarns of plain woven fabric, (b) weft yarns of plain woven fabric 46
Figure 3-3: Yarn width measurements for (a) warp yarns of twill woven fabric and (b) weft yarns of twill woven fabric 47
Figure 3-4: Fiber diameter measurements from different regions of materials..... 49
Figure 3-5: Elliptical voids and its axes representation [44] 50
Figure 3-6: Semi major axis length distribution for all laminates 51
Figure 3-7: Semi medium axis length distribution for all laminates 51
Figure 3-8: Semi minor axis length distribution for all laminates 52
Figure 3-9: Geometric mean of transversal axes distribution for all laminates 54
Figure 3-10: Elongation factor distribution for all laminates 54
Figure 3-11: Elongation factor distributions for V-P and A-P 56
Figure 3-12: Elongation factor distributions for V-T and A-T 56
Figure 3-13: Stress-strain curves for plain woven composites (a) vacuum oven cured, (b) autoclave cured 60
Figure 3-14: Stress-strain curves for twill woven composites (a) vacuum oven cured, (b) autoclave cured 62
Figure 3-15: Typical thermomechanical response of composite laminates in rotational rheometer..... 66
Figure 4-1: Isometric and cross section view with varying yarn spacing ratio. (a) YSR is 0, (b) YSR is 0.25 (c) YSR is 0.5 69
Figure 4-2: Yarn crimp ratio varying from 0 to 1. In (a), warp yarns are linear and weft yarns crimp around them (YCR=0), in (b) both warp and weft yarns crimp equally (YCR=0.5), in (c) weft yarns are linear and warp yarn crimp around them (YCR=1) 70
Figure 4-3: Representation of periodic BC [57] 72

Figure 4-4: Top view (a), side view (b) and isometric view (c) of the unit cell of woven plain fabric 74
Figure 4-5: Applied meshes for the finite element analysis of V-P composite. (a) voxel meshed fiber structure without matrix (b) voxel meshed composite structure with matrix (c) conformal meshed fiber structure without matrix (d) conformal meshed composite structure with matrix 79
Figure 4-6: Three-point bending test simulation setup (a) isometric view (b) front view 81
Figure 4-7: Meshed structure for three point-bending simulation of V-P 82
Figure 4-8: Three-point bending simulation results for plain woven composites .. 83
Figure 4-9: Major principal value of stress distribution in V-P composite beam... 83
Figure 4-10: Major principle value of stress distribution in V-P composite beam with hexahedral elements 84
Figure 4-11: Major principle value of stress distribution for V-P composite beam in static analysis with hexahedral elements 85
Figure 4-12: Top view (a), side view (b) and isometric view (c) of the unit cell of woven twill fabric 86
Figure 4-13: Three-point bending simulation results for twill woven composites . 90
Figure 4-14: Major principal value of stress distribution in V-T composite beam 90
Figure 5-1: Yarn cross section images for vacuum cured plain woven composite. (a) height measurements of warp direction, (b) width measurements of warp direction 104
Figure 5-2: Yarn cross section images for vacuum cured plain woven composite. (a) height measurements of weft direction, (b) width measurements of weft direction. 105
Figure 5-3: Yarn cross section images for autoclave cured plain woven composite. (a) height measurements of warp direction, (b) width measurements of warp direction 106

Figure 5-4: Yarn cross section images for autoclave cured plain woven composite. (a) height measurements of weft direction, (b) width measurements of weft direction. 107
Figure 5-5: Yarn cross section images for vacuum cured twill woven composite. (a) height measurements of warp direction, (b) width measurements of warp direction 108
Figure 5-6: Yarn cross section images for vacuum cured twill woven composite. (a) height measurements of weft direction, (b) width measurements of weft direction. 109
Figure 5-7: Yarn cross section images for autoclave cured twill woven composite. (a) height measurements of warp direction, (b) width measurements of warp direction 110
Figure 5-8: Yarn cross section images for autoclave cured twill woven composite. (a) height measurements of weft direction, (b) width measurements of weft direction. 111

LIST OF ABBREVIATIONS

ABBREVIATIONS

ASTM	American Society for Testing and Materials
3D	Three Dimensional
CNC	Computer Numerical Control
CoV	Coefficient of Variation
D-I	Double-Inclusion
DIC	Digital Image Correlation
DMA	Dynamic Mechanical Analysis
FEA	Finite Element Analysis
FEH	Finite Element Homogenization
gsm	Grams per Square Meter
ISO	International Standard Organization
MFH	Mean Field Homogenization
M-T	Mori-Tanaka
RVE	Representative Volume Element
UD	Unidirection

CHAPTER 1

INTRODUCTION

Composite materials (or simply composites) are natural or synthetic materials, composed of at least two constituents with distinct properties. The primary purpose of using composites is to enhance material properties by leveraging the distinct superior characteristics of their different constituents [1]. At the current level of technological development, fibers with small diameters in range of microns, are considered the best candidates for structural engineering applications. Among various fiber materials, carbon ones stand out due to their exceptionally high strength, which is attributed to the stiff C-C and C-N bonds in graphitic planes as well as their very small defect size and proportion [2]. Fibers themselves cannot be used as structural materials because of their negligible compressive strength, primarily due to issues such as buckling and surface degradation. These limitations can be overcome by infiltrating fibers within a polymer matrix, giving rise to polymer matrix composite materials [3].

1.1 Polymer Matrix Composites

Polymer matrix composites are highly advantageous for applications that require light weight materials with high strength and stiffness. Lightweight engineering is becoming increasingly important in addressing structural design challenges. As a result, composites are widely used in industries such as aerospace, defense, automotive, and sports. Their high processibility, along with good corrosion and weather resistance, further enhances their suitability for a variety of applications [4]. Composite materials primarily consist of reinforcement elements embedded within

matrices. The reinforcements, which are often fibers, are mainly responsible for carrying structural loads. The mechanical properties of composites depend on the orientation and volume fraction of these reinforcements. The matrix, on the other hand, protects the reinforcements from environmental effects, holds them together, and most importantly transmits the applied loads to the reinforcements, resulting in a material that is naturally heterogeneous and anisotropic [5].

An infinite number of combinations can be created when producing polymer matrix composites. Each matrix-reinforcement combination results in a unique material with distinct properties. It is very crucial to understand the requirements of the application and design the material accordingly. Reinforcements are generally categorized into three groups based on fiber dimensionality and orientation. Composites with aligned 1D reinforcements are called unidirectional composites. Those with 2D reinforcements are commonly referred as woven composites and are composed of woven fabrics such as plain, twill, and satin weaves. Composites with 3D reinforcements, on the other hand, are divided into 2 subcategories as angle-interlock and orthogonal interlock. These reinforcements can be supported either layer-to-layer or through-thickness, as shown in Figure 1-1 [6]. Examples of 3D composite reinforcements include non-crimp fabrics, braided fabrics, and knitted fabrics [7]. Each type of composite reinforcement offers unique advantages and disadvantages, making them suitable for specific industrial applications. In this study, 2D plain and twill woven composites are studied, and they will be introduced in greater detail in the subsequent sections.

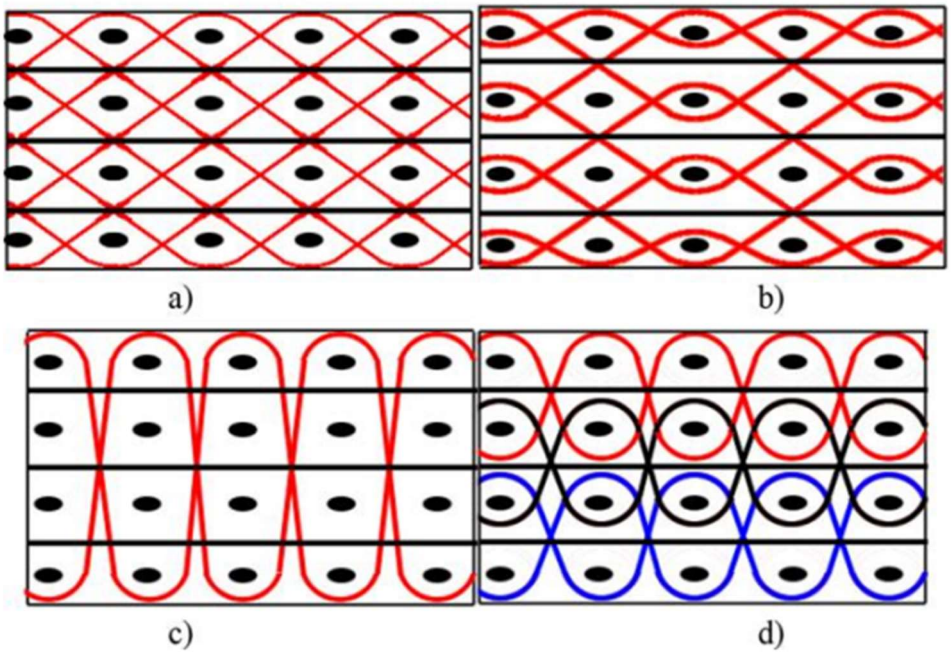


Figure 1-1: 3D weave examples: a) 3D through-thickness angle-interlock woven composites, b) 3D layer-to-layer angle-interlock woven composites, c) 3D through-thickness orthogonal interlock woven composites d) 3D layer-to-layer orthogonal-interlock woven composites. [6]

1.2 2D Woven Composites

Woven fabric composites (WFCs) or textile composites are widely used in industrial applications such as defense, aerospace, automotive, and sports due to their numerous technical advantages. For instance, carbon fiber has a higher elastic modulus than steel while maintaining significantly lower density. Although, various textile products are utilized in composites, woven fabrics are particularly important because they offer improved mechanical properties in multiple directions [8].

Woven fabrics are manufactured through a process that involves interlacing weft yarns around the warp yarns. This long-established technique serves as the foundation of WFCs. The production process begins with the preparation of yarns

which can be made from materials such as carbon, glass, aramid, basalt or polymers, depending on the desired properties of the final fabric product [9, 10].

The woven product is classified based on the weaving process. The final properties of the fabric are mainly determined by the yarn material and the weave pattern. The weave pattern is defined by how the weft yarns are interlaced with the warp yarns. For instance, if the pattern follows a 1×1 interlacement, the final fabric is classified as plain woven. Similarly, if the pattern involves a 2×2 interlacement with a shift at each step that forms a cross pattern, the fabric is classified as twill woven. Numerous weave patterns can be created to produce fabrics with diverse properties [11]. The most commonly used woven fabrics are shown in Figure 1-2 [4].

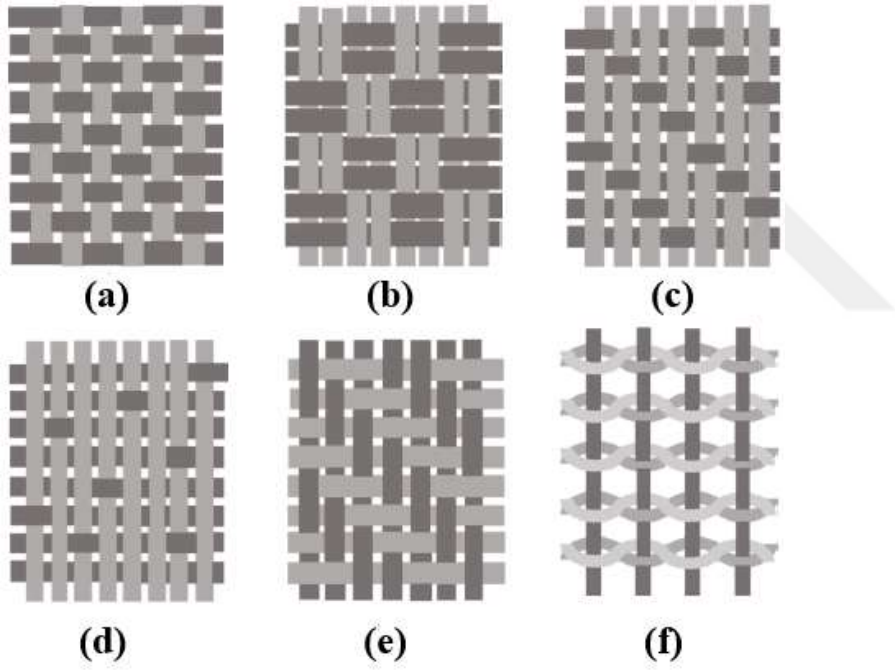


Figure 1-2: Schematics of different woven fabrics (a) plain weave, (b) basket weave, (c) 3×1 crowfoot, (d) 8-harness satin weave, (e) 2×2 twill weave (f) leno weave [4]

Each weaving pattern imparts unique properties to the final products. Properties such as drapeability, stability, porosity, crimp, smoothness, and symmetry determine mechanical behavior, both inter- and intra-fabric resin permeability, and manufacturability of WFCs. Drapeability refers to the ability of the fabric to conform to the surface of a mold and is correlated with crimp, which describes the angle

between warp and weft yarns [12]. Stability, on the other hand, measures how well a fabric retains its shape and size under loads and deformations. Among the fabrics used in structural applications, plain fabrics are often considered as the most stable [13]. Porosity is the main parameter determining the resin characteristics and void content in the final product. Fabrics that lead to higher porosity values are typically used in clothing industry, while lower porosity is preferred for structural applications [14]. Symmetry also plays a crucial role in structural applications, as symmetric fabrics provide more stable and predictable mechanical performance due to an almost equal fiber fraction in 0° and 90° directions, facilitating easier prediction of their mechanical properties through analytical and computational techniques [15].

Peirce [16] investigated the relationship between fabric geometry, structure, and their influence on the final properties of the woven fabrics, proposing several formulations. One of his geometric representations, shown in Figure 1-3, illustrated the the crimp angle between warp and weft yarns. This angle is important because the friction and structural geometry of these features essentially determine the load-carrying capacity of WFCs.

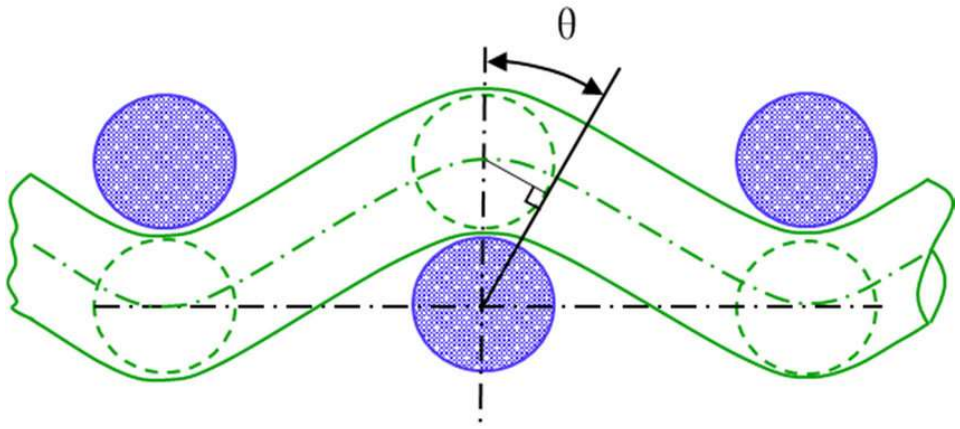


Figure 1-3: Definition of yarn crimp angle using geometrical model created by Peirce [16]

1.3 Production and Curing Techniques of Woven Composites

There are various methods for manufacturing 2D woven composite laminates. Resin transfer molding, prepreg lay-up, and vacuum-assisted resin infusion are some of the widely used traditional production tecniques. The choice of methods depends on the materials used, the desired part design, and the required tolerances. Among these, prepreg lay-up method stands out as advantageous due to homogeneous resin distribution, controlled fiber fraction, ease of manufacturing, reproducibility, and good surface quality on non-mold surfaces. In the prepreg lay-up method, a mold suitable for the desired part is used. Once the lay-up sequence is completed, the parts are cured using temperature, pressure, vacuum, microwave energy, or combination of these. For example, vacuum oven curing (also referred as vacuum bag-only curing), utilizes temperature and vacuum, whereas autoclave curing incorporates additional pressure into the process. The selection of curing method depends on prepreg material, and the desired properties of the final part.

Autoclave and vacuum oven curing are utilized in this study. The autoclave curing technique is known to provide better compaction during curing than vacuum ovens, making it the preferred choice. However, its high energy consumption and longer processing times make the autoclave route less favorable. Consequently, there is a growing trend toward achieving fully cured parts using vacuum oven curing. Prepreg manufacturers are actively developing materials specifically designed for this technique.

At present, there are many commercially available out-of-autoclave materials with specialized resin formulations. Nevertheless, studies [18, 19] indicate that curing in an autoclave still provides superior mechanical properties compared to other methods. Research efforts to develop advanced resins for out-of-autoclave curing are ongoing.

1.4 Micromechanical Modeling of Woven Composites

Micromechanical modeling is a crucial approach for understanding and predicting the mechanical properties of complex composite structures at a microscopic level. This modeling approach aims to accurately and efficiently predict effective material properties by accounting for every detail in the microstructure of composites. Modeling the complex microstructure of woven composites involves many features, such as non-linear yarn geometries, undulations, and interfaces between reinforcement and matrix. Due to the multi-scale nature of these materials, creating accurate virtual models can be particularly challenging. Various modelling techniques and approaches, generally classified into two main groups, have been employed to address this challenging issue.

The first category consists of analytical models, which use mathematical formulations to compute effective properties based on microstructural information such as volume fractions and constituent properties. The oldest and most well-known analytical model for property prediction is Voigt and Reuss Bounds [20, 21], commonly referred as the Rule of Mixtures. The Voigt model provides a linear upper bound for properties in the parallel direction of fibers, while the Reuss model defines a lower bound for transverse loading condition. Following the establishment of these bounds, many different analytical models have been introduced in literature, each with its own strengths and limitations. Despite these variations, analytical models remain some of the most efficient tools for predicting effective properties.

1.4.1 Mean Field Homogenization (MFH)

Mean field homogenization (MFH) is a powerful analytical tool for estimating effective properties of heterogeneous materials by simplifying complex interactions between distinct phases within a composite. MFH operates on the principle of averaging local stress and strain fields to estimate the macro properties. It employs a statistical approach to average properties of individual phases within the composite.

Main advantages of this approach include ease of use, speed (low CPU time), and minimal memory requirements. However, its primary limitation is that it provides only approximates volume, average stress and strain without offering detailed information on their distribution within the material. A representation for MFH procedure is shown in Figure 1-4.

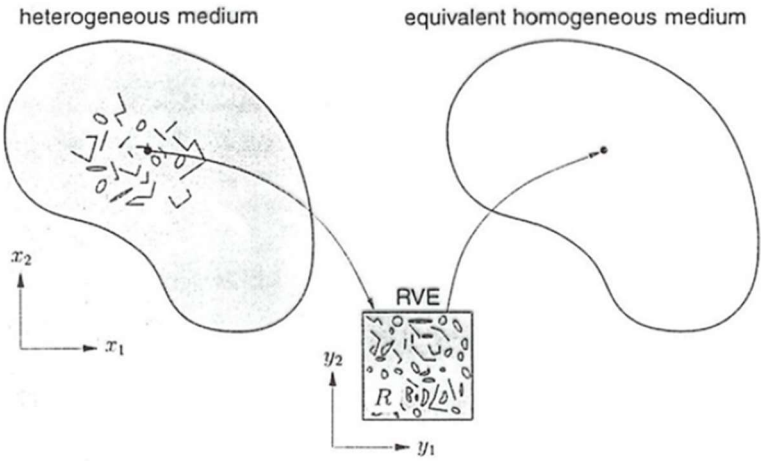


Figure 1-4: Micro-macro transition. The upper left represents microscopic scale, the upper right represents macroscopic scale, and the transition between these scales is obtained by RVE (representative volume element) [22].

1.4.2 Eshelby's Inclusion Problem

John D. Eshelby, is renowned for his solution to Eshelby's inclusion problem [23], published in 1957, which has significantly advanced MFH procedures. He provided a solution for calculating the strain field within an infinite isotropic elastic material, as illustrated in Figure 1-5. This solution demonstrates how fibers are strained within an infinite isotropic elastic matrix, making it a corner stone for analytical models of composite materials. Eshelby's solution accounted for the effect of the inclusion on the composite by considering the shape and orientation of the inclusion. Following the publication of this solution, several well-known MFH schemes, such as Mori-Tanaka, Single Inclusion, and Double Inclusion, have been developed.

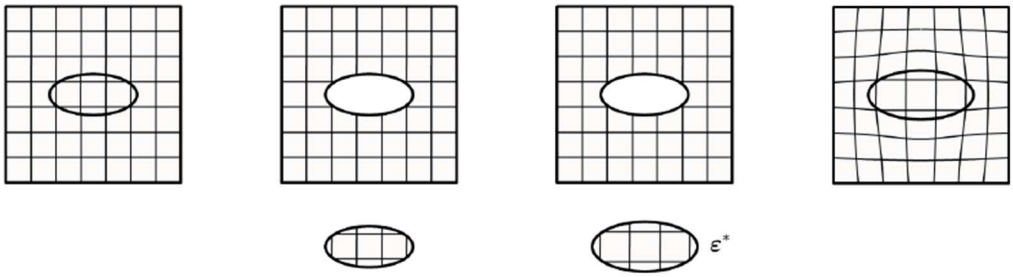


Figure 1-5: Solution to the Eshelby's inclusion problem steps, sequence of imaginary cutting an ellipsoidal from an infinite material, straining it and welding it back to its place [24].

1.4.3 Mori-Tanaka MFH Scheme

The Mori-Tanaka scheme [25] is a widely used method in the MFH procedure to estimate elastic properties of composite materials. It builds on Eshelby's solution for a single ellipsoidal inclusion and extends it to multiple inclusions. This scheme predicts mechanical properties based on the shape, size, and orientation of the inclusions while considering contributions from both the matrix and reinforcement materials [26]. It is applicable to various composite materials, including unidirectional, particle reinforced, random fiber reinforced and woven types [27]. Basic formulation of the Mori-Tanaka scheme was later refined by Benveniste [28] and the effective stiffness tensor is provided in Equation 1-1.

$$C^* = C_m + v_f\langle(C_f - C_m)T\rangle\left[v_m I + v_f\langle T\rangle\right]^{-1} \qquad (1-1)$$

In Equation 1-1, subscripts *"m"* and *"f"* stand for matrix and fiber, respectively, whereas *C*, v, T,* and *I* represent effective stiffness tensor, volume fraction, strain concentration tensor, and fourth order identity tensor, respectively. Tensor *T* is given in Equation 1-2.

$$T = \left[I + EC_m^{-1}\left(C_f - C_m\right)\right]^{-1} \qquad (1-2)$$

In Equation 2, *E* represents Eshelby's tensor, which depends solely on the shape of the inclusions and the Poisson's ratio of the matrix, making the tensor calculation computionally straightforward [29]. Additionally, for two phase composites, effective stiffness tensor is symmetrical along the diagonal if any one of the following conditions is met:

1. Inclusions are isotropic materials.
2. Inclusions are randomly oriented or aligned.
3. Inclusions are spherical in shape.

For woven composite case studied in this thesis, conditions 1 and 3 are not satisfied because carbon fibers are transversely isotropic, and yarns have an elliptical shape. However, since they are aligned in 0° and 90° directions, the effective stiffness tensors calculated using the Mori-Tanaka MFH scheme exhibits this property [28, 30, 31]. A representation for the Mori-Tanaka MFH scheme is shown in Figure 1-6. In this scheme, each individual inclusion within the representative volume element (RVE) is treated as if it is isolated within the real matrix. The material is assumed to be infinite and is subjected to strains corresponding to those in the actual RVE. While this homogenization scheme is highly successful at estimating the effective properties of two-phase composites, it is theoretically limited to fiber volume fractions of up to 30%. Nevertheless, it has been shown to successfully predict the properties of composites with higher fiber fractions in practice.

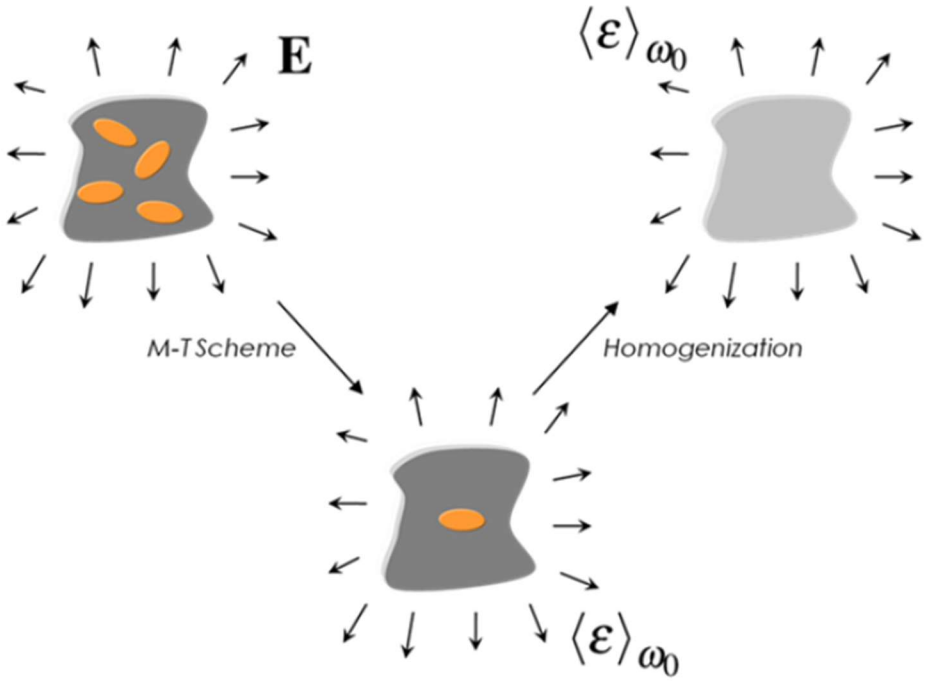


Figure 1-6: Mori Tanaka MFC scheme simple interpretation [24].

1.5 Homogenization Using Finite Element Analysis

Another approach to estimating the effective mechanical properties of woven composite materials involves the use of the Finite Element Analysis (FEA). This method, commonly referred to as computational homogenization in literature, has been described in a four-step homogenization process by Squet [32].

The first step of this scheme involves identifying a representative volume element (RVE) at the meso-scale that accurately represents the microstructure of the composite material. In this RVE, the composite material is modeled using precise geometric features and the material properties of its constituents. Constructing the RVE is a critical step, as macro boundary conditions are directly applied to it in subsequent stages. The RVE must be large enough to capture all relevant information but small enough to maintain computational efficiency. It should incorporate geometric parameters, such as the cross-sectional shape and path of yarns, their position within the structure, and the undulation function. If any geometric parameter

cannot be accurately modeled within the RVE, simplifying assumptions can be made to reduce the complexity of the simulations [33].

After constructing the RVE, the macro-to-micro transition is performed, and boundary conditions are applied to the RVE to run simulations. Once the computations are complete, the macroscopic response of the composite is determined based on the deformed microstructure of the RVE. Outputs such as displacements, loads, and homogenized macro-scale material properties are obtained, completing the micro-to-macro transition. Finally, the relationship between input and output parameters is analyzed in detail. A schematic representation of the homogenization scheme using finite element approach is shown in Figure 1-7.

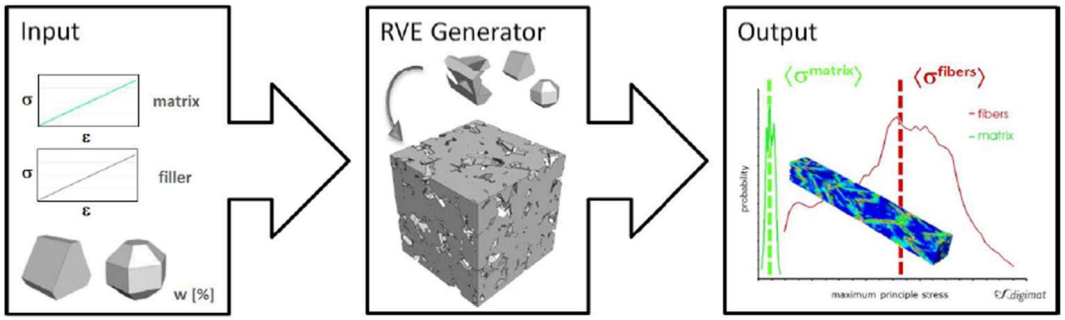


Figure 1-7: Homogenization using finite element approach [57].

1.6 Orthotropic Material Properties

Woven composite materials have specially designed material properties along three principal axes, making them intrinsically orthotropic. They exhibit very high stiffness along their primary directions but are less stiff at other angles. Consequently, the constitutive elastic stiffness tensor is adjusted accordingly. Fourth-order stiffness tensors essentially have 81 (3^4) components; however, this number is reduced to 21 for anisotropic materials by utilizing major and minor symmetries. For orthotropic materials, the number can be further reduced to 9 by considering the equality of elastic constants. The stress-strain relationship for an orthotropic linear elastic in Voigt notation is presented in Equation 3.

$$\begin{bmatrix}\sigma_{11}\\ \sigma_{22}\\ \sigma_{33}\\ \sigma_{23}\\ \sigma_{13}\\ \sigma_{12}\end{bmatrix} = \begin{bmatrix}S_{11} & S_{12} & S_{13} & 0 & 0 & 0\\ S_{12} & S_{22} & S_{23} & 0 & 0 & 0\\ S_{13} & S_{23} & S_{33} & 0 & 0 & 0\\ 0 & 0 & 0 & S_{44} & 0 & 0\\ 0 & 0 & 0 & 0 & S_{55} & 0\\ 0 & 0 & 0 & 0 & 0 & S_{66}\end{bmatrix}\begin{bmatrix}\varepsilon_{11}\\ \varepsilon_{22}\\ \varepsilon_{33}\\ \varepsilon_{23}\\ \varepsilon_{13}\\ \varepsilon_{12}\end{bmatrix} \qquad (1-3)$$

The stiffness matrix presented in Equation 3 is crucial as it represents the elastic behavior of materials and is essential for mechanical and structural analysis. This matrix defines how a material responds to unit deformation and how much it deforms under specific loads. Traditionally, the stiffness matrix is determined through mechanical characterization techniques, which are often time-consuming, costly, and labor-intensive. Therefore, accurately determining the stiffness matrix using homogenization and computational methods provides a significant advantage in engineering applications.

1.7 Aim and Motivation of the Thesis

The primary aim of this thesis is to compare different computational methods for predicting the elastic properties of composite materials in terms of accuracy and efficiency. These methods are validated through experimental studies to assess their reliability. Specifically, the study examines whether computational approaches can accurately capture the mechanical property differences arising from the distinct microstructures formed by different curing methods, such as autoclave and out-of-autoclave processes. To support this, the effectiveness of these curing methods in influencing microstructural features—such as yarn geometry, cured ply thickness, and void characteristics—was also investigated experimentally. To achieve these goals, micromechanical approaches, including mean field homogenization and finite element homogenization, are employed. The final objective is to evaluate the strengths and limitations of these modeling strategies, focusing on their accuracy, ease of use, and computational efficiency.

The motivation for this study stems from the fact that mechanical characterization of composite materials requires extensive labor, time, and financial resources. Given the versatility of composite materials, which can be tailored through various lay-up orientations and matrix/reinforcement combinations, a reliable methodology for predicting mechanical properties is highly desirable. With numerous approaches available, this study focuses on identifying the most effective method for this purpose. The findings are expected to help reduce material characterization costs and provide valuable insights for the design of structural composite components used in the defense, aerospace, and automative industries.

This thesis is structured into five chapters. The Introduction outlines the research background, objectives, and motivation for investigating the mechanical properties of woven composite materials. The Experimental Work chapter provides details on the characterization of composite constituents, the manufacturing process of the laminates, and the methods used for mechanical, physical, and thermal property evaluation. In the Results and Discussion chapter, the experimental findings are

presented and analyzed, with a focus on key trends and significant observations. The Modeling, Simulations, and Validation chapters describe the multi-scale modeling approach, simulation results, and their validation against experimental data. Finally, the Conclusion summarizes the main outcomes of the study, highlights its contributions, and offers recommendations for future research.

CHAPTER 2

EXPERIMENTAL WORK

Experimental work conducted in this study is divided into three categories. First, mechanical and physical characterization of the composite constituents -fiber and resin- are performed to gather the necessary input data for analytical and numerical simulations. Second, woven composite laminates are manufactured, and their geometrical properties were measured for use in material models. Finally, a coupon-level mechanical, physical, and thermal characterization process is carried out to validate the modeling and simulation results.

2.1 Woven Carbon Fiber/Epoxy Prepregs Used in the Study

In this study, two different woven carbon/epoxy pre-impregnated materials manufactured by SPM Prepreg Systems (Türkiye) are used. Tradenames for these materials are listed below.

1. VTP DA100 CFA200 3KP RC40 HS Carbon Prepreg
2. VTP DA100 CFA245 3KT RC40 HS Carbon Prepreg

Both materials consist of the same epoxy resin as matrix, which is named as VTP DA 100. This epoxy resin is formulated by the prepreg manufacturer company, but its formulation remains undisclosed. The epoxy system used in the prepreg has reportedly good drape and tack properties, no volatile content during curing, and is suitable for processing with vacuum bagging techniques.

Woven fabrics used as reinforcement differ between plain woven fabric and twill woven fabric composites. The former prepreg incorporates a 200 gsm plain woven fabric, while the latter incorporates a 245 gsm twill woven fabric. Both fabrics are

made of standard modulus high-strength carbon fiber tows with 3K filaments, manufactured by DowAksa (Türkiye).

The prepreg materials used in this study, along with the resin and carbon fabric they contain, are obtained together from the manufacturer. To focus solely on the effects of production routes, all materials were sourced from the same production batch to minimize variations in properties.

2.2 Characterization of Composite Constituents

2.2.1 Fiber Characterization

Mechanical and physical properties of fibers are essential for micromechanical material models and must be determined. However, the fibers themselves are not directly characterized in terms of mechanical properties in this study. Instead, their properties are obtained from the manufacturer technical data sheet and listed in Table 2-1.

Table 2-1: Mechanical and physical properties of carbon fiber

Property	**Value**	**Unit**	**Standard**
Tensile Strength	3800	MPa	ISO 10618
Longitidunal Modulus	240	GPa	ISO 10618
Transverse Modulus	15	GPa	-
Longitidunal Poisson's ratio	0.20	-	-
Transverse Poisson's ratio	0.33	-	-
Shear Modulus	8.95	GPa	-
Elongation at Break	1.6	%	ISO 10618
Density	1.78	g/cm^3	ISO 10119
Tex	200	g/km	ISO 1889

Fiber diameter, another important parameter for material models, is not specified by the manufacturer. To address this, scanning electron microscopy (SEM) investigations are conducted using Thermo Scientific Phenom XL G2 Desktop SEM. 230 measurements are conducted using 11 images from different regions. Those images are given in Figure 2-1.

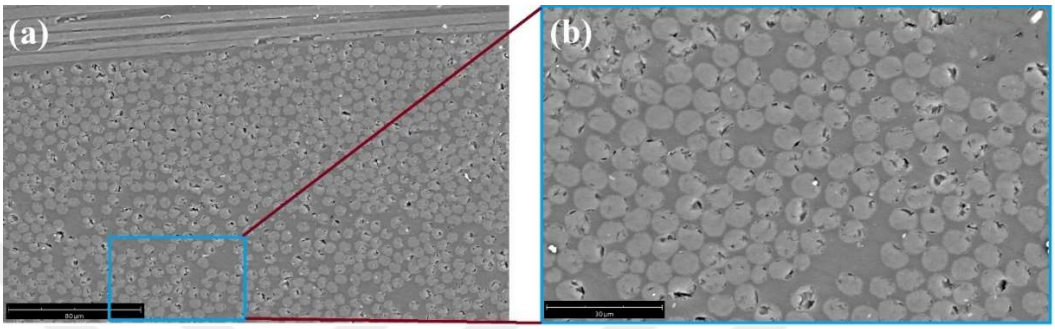


Figure 2-1: SEM images of composite cross section for fiber diameter measurements.

Using ImageJ, an image processing and analysis software, the diameters of numerous fibers are measured. The average fiber diameter is determined to be 6.84 μm with a standard deviation of 0.35 μm. This value is recorded for use in material models.

2.2.2 Resin Characterization

The matrix material, epoxy resin, is extensively characterized in terms of its mechanical and physical properties. Since this study aims to predict elastic mechanical properties of composites, the elastic properties of matrix are determined in accordance with ASTM D638-14. For this purpose, tensile coupons are prepared following Type I specification of the standard. The coupons are manufactured by pouring liquid resin into molds and curing them using an appropriate curing cycle. This curing cycle is shown in Figure 2-2.

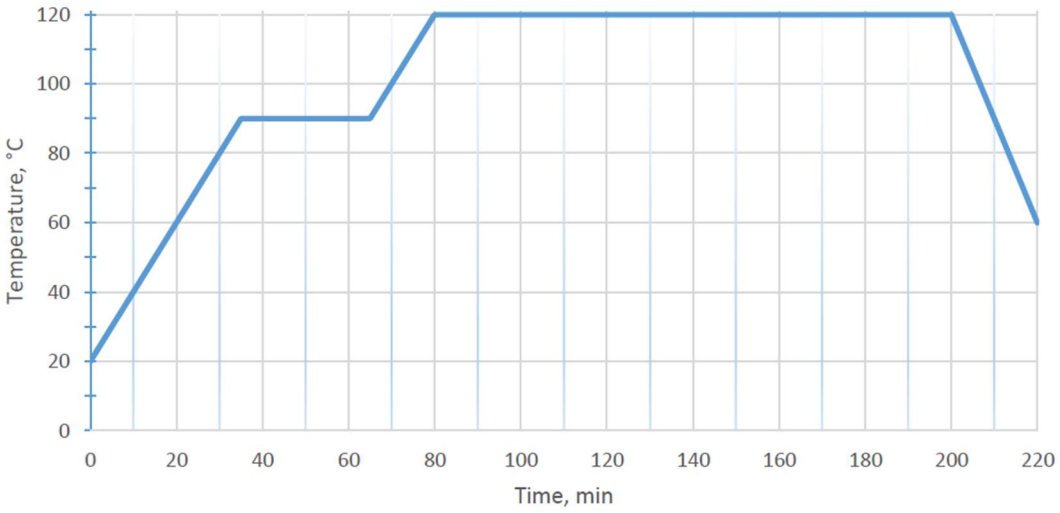


Figure 2-2: Recommended curing cycle of VTP DA-100 epoxy resin

Specimen technical drawing and the dimensions are given in Figure 2-3 and Table 2-2.

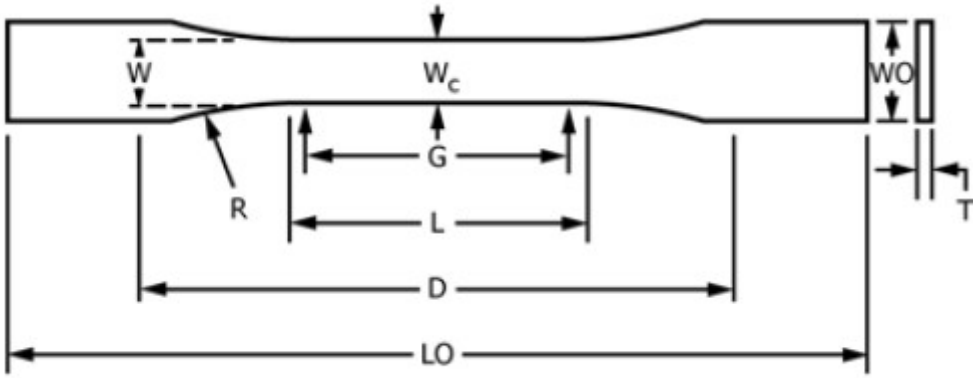


Figure 2-3: Technical drawing of epoxy resin coupons in accordance with ASTM D638-14 Type I. Dimensions are given in Table 2. [55]

Table 2-2: Dimensions of epoxy resin tensile coupons in accordance with ASTM D638-14 Type I

Feature	**Dimensions [mm]**
W - Width of narrow section	13
L - Length of narrow section	57
WO - Width overall, min	19
LO - Length overall, min	165
G - Gauge length	50
D - Distance between grips	115
R - Radius of fillet	76
W_c - Width tolerance for middle section	+0 -0.10

Manufactured epoxy resin coupons, preparared according to ASTM D638-14, are shown in Figure 2-4. Following the preparation of tensile test coupons, tests are conducted using Instron 4481 utilizing a 50 kN load cell and ARAMIS 12M Digital Image Correlation (DIC) system provided by GOM GmbH (Germany) for strain measurement. The DIC method was chosen due to its high accuracy, which is essential for determining both elastic modulus and Poisson's ratio. Unlike strain gauges, which measure strain only at their attachment area, DIC allows observation of larger surface areas to, enabling the capture of localized strains. Additionally, DIC requires less labor when compared to strain gauges. Other methods, such as advanced video extensometers or contact-type extensometers, lack the precision provided by DIC. Studies by Kwon et al. [32] and Zhang et al. [33] have also demonstrated that for fibrous composites, the DIC method is more accurate than strain gauges.



Figure 2-4: Manufactured epoxy resin coupons before tensile testing

The DIC method, however, requires specimen surfaces to be neatly prepared since it relies on image processing. Specimen surfaces should be clean, smooth, and feature a homogenous, high-contrasted point or a freckle pattern to ensure the acquisition of accurate strain measurements. To create this pattern, simple can spray paints are used. Firstly, surfaces are evenly coated with white paint, followed by a light spray of black paint to produce the necessary contrast. Preperation steps for DIC measurements are shown in Figure 2-5.

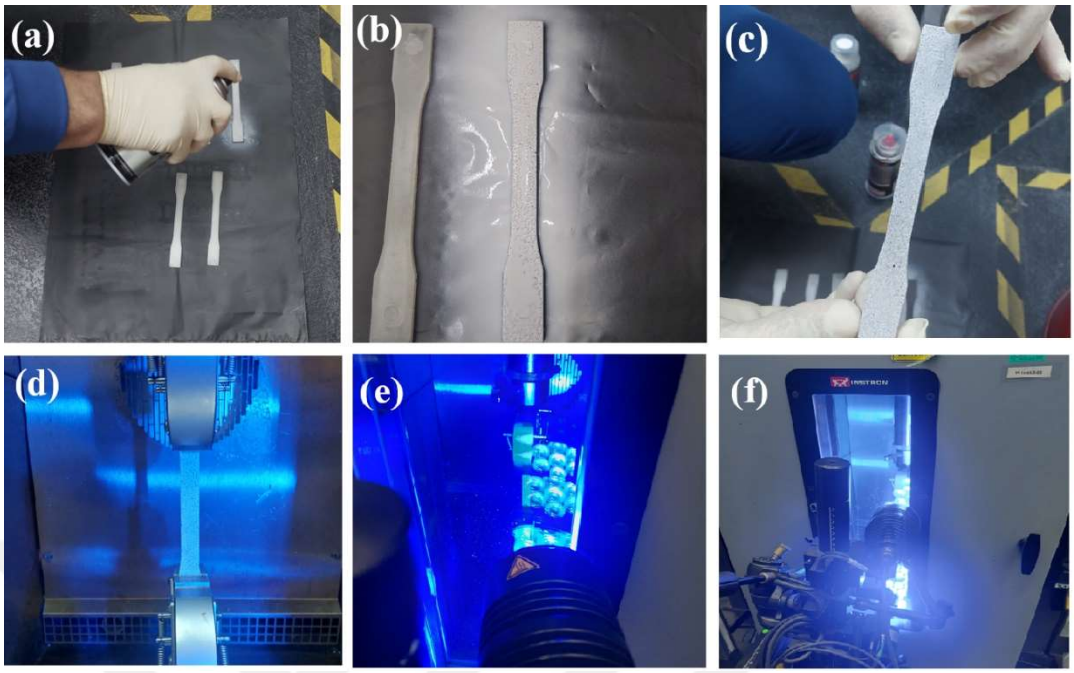


Figure 2-5: DIC specimen preparation and testing steps. Painting of the specimen surfaces are shown in (a) and (b). Specimen surface after black paint application is shown in (c). Mounted specimen is shown in (d). Light and position settings are shown in (e) and (f).

The camera angle is set to 25.32°, with all images captured at full resolution (4096 x 3000) and a snapping frequency of 2 frames per second. The obtained data is subsequently processed using ARAMIS Professional 2020 software to determine stress and strain. Fractured test coupons and failure modes are shown in Figure 2-6.

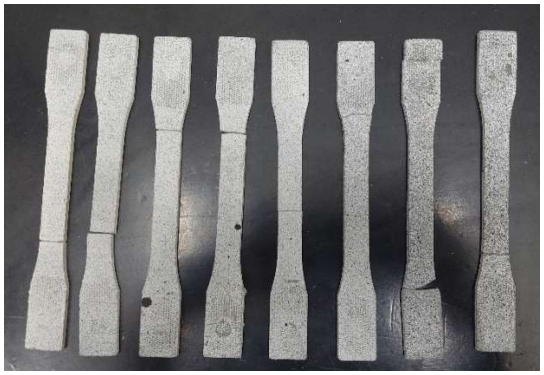


Figure 2-6: Tensile failure modes of the coupons

For tensile tests of epoxy resin, 8 specimens are prepared and tested, however two of them failed in the jaw region rather than the gauge region. Therefore, their results are excluded as they did not comply with failure mode specifications outlined in the standard. From these tests, elastic modulus and Poisson's ratio, which are the two of the most critical inputs for material models, are obtained. Further, density, another parameter for modeling, is measured using a Mettler Toledo Balance XPR305DR with an installed density kit.

2.3 Manufacturing of Composite Laminates Using Prepreg Lay-Up Technique

As mentioned before, raw material prepreg is obtained from the manufacturer in rolled form. To obtain composite coupons, four laminates are manufactured using prepreg lay-up technique onto an aluminum plate mold. In this section, the manufacturing steps of this procedure are explained.

2.3.1 Material Preparation and Lay-up Technique

Manufacturing process starts by cutting appropriately sized sections from the rolled prepreg. The sections are prepared based on the number of plies to be laid laid and the dimensions of the coupons to obtain sufficient surface area in the resulting laminate. The number of plies is determined according to the required thickness of the laminate, which is selected to meet the coupon thickness of specified in the standard. For that purpose, 10 plies of twill woven prepreg and 12 plies fof plain woven prepreg are used to achieve the necessary laminate thickness. While ply cutters are generally utilized for this task, hand cutting is also practical for simple geometries like square sections. Accordingly, 20 plies of woven twill prepreg and 24 plies of woven plain prepreg are cut into 50x50 cm^2 square pieces.

Both twill and plain woven fabrics in the prepregs used in this study are balanced, meaning they contain equal amounts of fiber in warp and weft directions. Properties of woven fabrics are given in Table 2-3.

Table 2-3: Woven fabric properties used in this study

Manufacturer Code	**Areal Weight [g/cm3]**	**Weave**	**Warp Count (/10 cm)**	**Weft Count (/10 cm)**
CFA 200 P	200	Plain	50	50
CFA 245 T	245	Twill	60	60

Even though the warp and weft count of the fabrics are identical, some plies are rotated during lamination to minimize variations in the mechanical properties of the laminate between 0° and 90°. Ply stacking sequences of laminates are given in Table 2-4.

Table 2-4: The stacking sequences of laminates. Dashed line represents mid-plane of laminates

Plain Woven Fabric-Epoxy Laminates	Twill Woven Fabric-Epoxy Laminates
0°	
90°	0°
0°	90°
90°	0°
0°	90°
90°	0°
90°	0°
0°	90°
90°	0°
0°	90°
90°	0°
0°	

Both stacking sequences are chosen to ensure a balanced and symmetric laminate. Balanced laminates have equal amounts of fiber in 0° and 90° directions, preventing in-plane shear/extension stiffness couplings. Symmetric laminates, on the other

hand, possess material and geometrical symmetry around the mid-plane of laminate, eliminating bending/extension stiffness couplings.

The stacking process is carried out as described above. During stacking, an intermediate vacuum, also called debulking, is applied to the laminate after stacking the first ply and after three plies are laminated to remove any inter-ply air bubbles. Each debulking step involves vacuuming the laminates for 15 minutes using an elastic, flexible vacuum bag. Once the stacking sequence is complete, the laminates are carefully vacuum bagged in preparation for the curing stage. Vacuum bagging procedure and configuration are shown in Figure 2-7 and Figure 2-8, respectively.

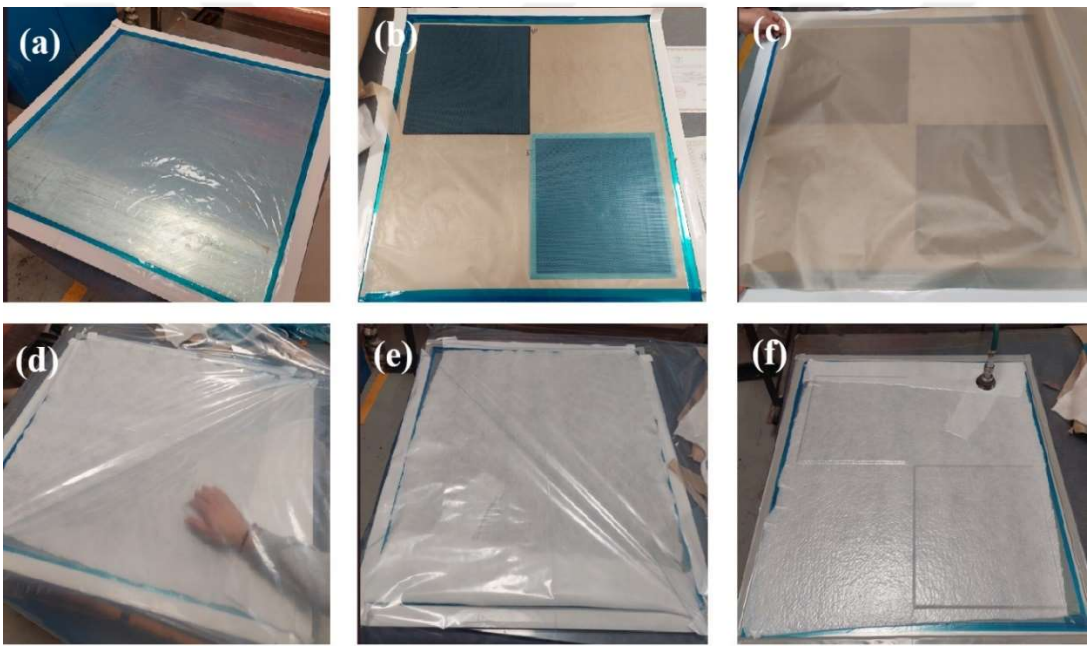


Figure 2-7: Vacuum bagging procedure. (a) Application of sealants to the edges of the plate and non-perforated release film. (b) and (c) Application of release films and peel ply. (d) and (e) Application of breather fabric and vacuum bag. (f) Completion of vacuuming

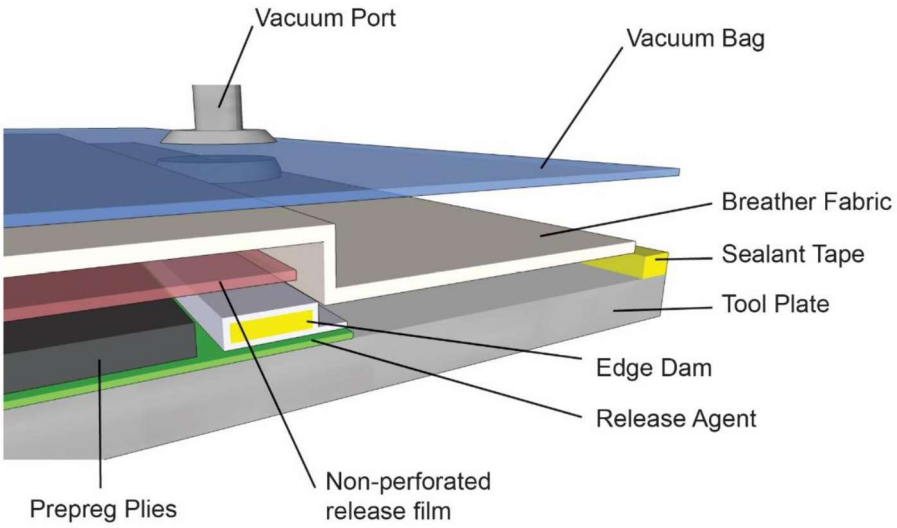


Figure 2-8: Schematic of composite vacuum bagging technique and consumables used

2.3.2 Curing and Consolidation Techniques

After the vacuum bagging, the parts are cured either in a vacuum oven or autoclave. As one of the aims of this study is to compare the mechanical properties of composite parts cured in different media, both methods are applied to each material. Hence, four laminates are fabricated using two types of prepreg materials: one set cured in a vacuum oven and the other one in autoclave. Vacuum oven and autoclave used in this study are shown in Figure 2-9.

Throughout the study, the denotation below will be used to distinguish between laminates.

- **V-P**: **V**acuum oven cured **p**lain woven fabric/epoxy composite
- **V-T**: **V**acuum oven cured **t**will woven fabric/epoxy composite
- **A-P**: **A**utoclave oven cured **p**lain woven fabric/epoxy composite
- **A-T**: **A**utoclave oven cured **t**will woven fabric/epoxy composite

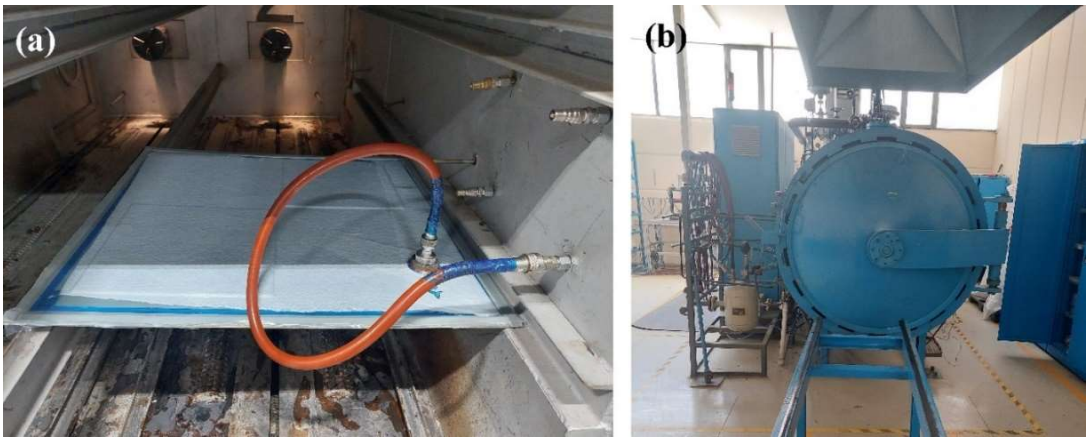


Figure 2-9: Different curing media for the laminates: (a) vacuum oven, (b) autoclave

A typical curing cycle for this prepreg material is given in Figure 2-2. For both vacuum oven and autoclave curing the given temperature cycle is followed. In both methods, a vacuum is applied to the laminates with vacuum port integrated into the vacuum bag. The key difference in autoclave is application of an external pressure of 7 bar to the laminates during the curing operation. The vacuum level is continuously monitored and recorded using pressure gauges, as shown in Figure 2-10.



Figure 2-10: -690 mmHg (~0.90 atm) pressure drop is measured for the laminates in vacuum oven and autoclave.

After curing is completed for both methods, the vacuum bag, release films, peel plies, and sealants are removed from the laminates, which are then marked for identification for further operations. These steps are shown in Figure 2-11.

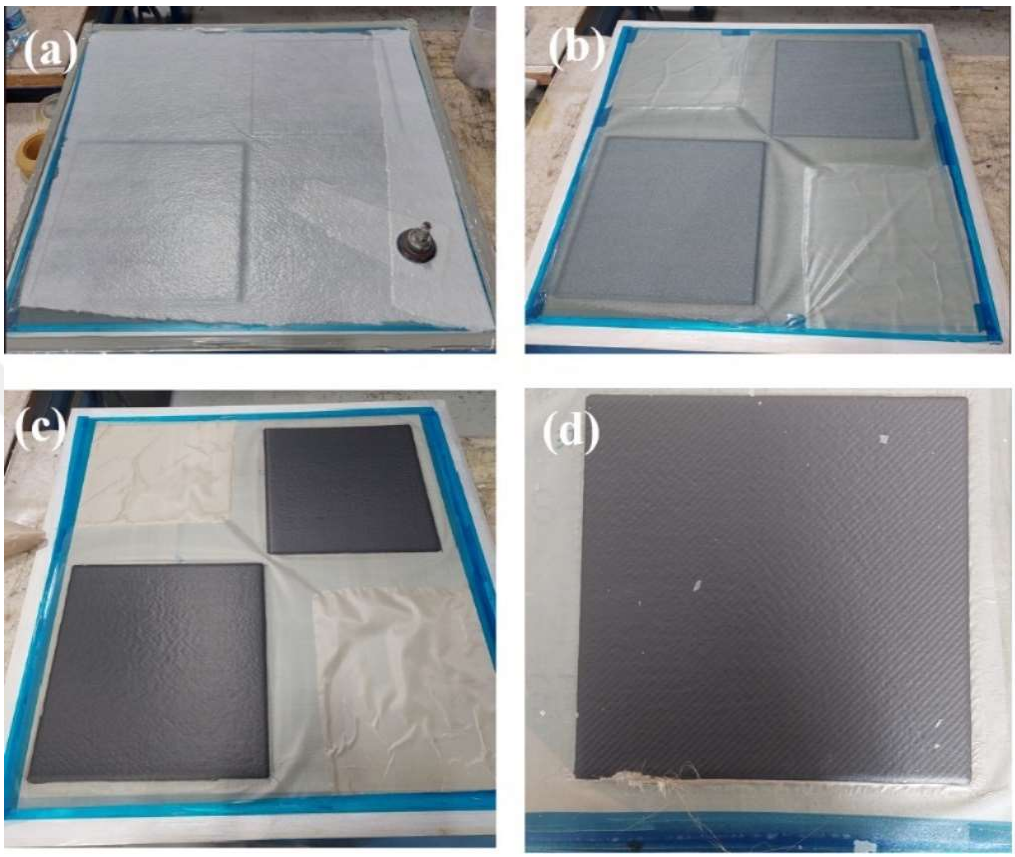


Figure 2-11: Removal of auxiliary materials such as the vacuum bag, peel ply, release film, and breather fabric, followed by obtaining the cured laminates

2.4 Manufacturing of Coupons and Specimens

Once the four cured laminates are obtained, a fine cutting operation is performed using a Labcut 5000 series composite plate saw manufactured by Extec (United Kingdom) is used. This computer numerical control (CNC) ensures high precision in preparing composite coupons and specimens. The machine used is shown in Figure 2-12.

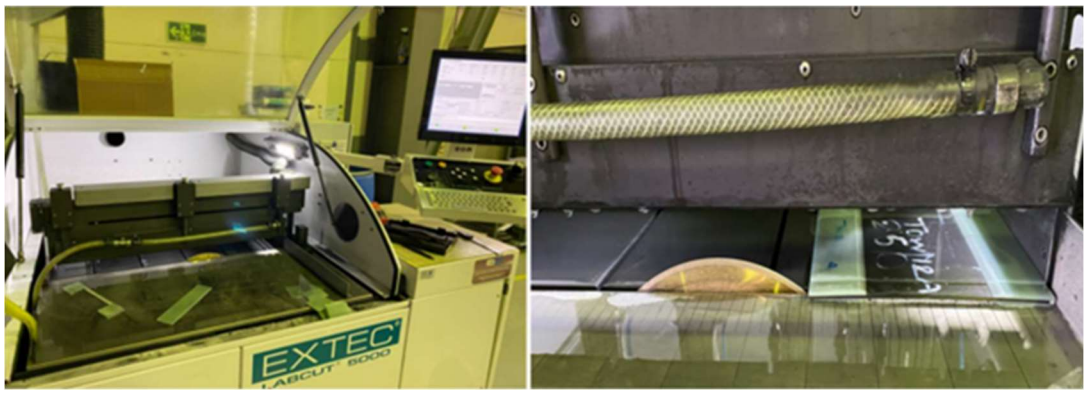


Figure 2-12: Precise cutting of composite plates into coupons and specimens

Coupons and specimens are cut for a range of analysis, including tensile tests, three-point bending tests, density measurements, fiber content measurements, optical microscopy, scanning electron microscopy, micro computed tomography, and rheometry for glass transition temperature (Tg) determination. The specimen dimensions, quantities, and relevant testing standards are tabulated in Table 2-5. Thickness of each specimen or coupon mentioned in Table 2-5 is same as the laminate thickness.

Table 2-5: Prepared coupons/specimens for further composite characterization

Test/Inspection	**Number**	**Width [mm]**	**Length [mm]**	**Standard**
Unidirectional tensile test	8	25	250	ASTM D3039
3-point bending test	8	13	50-55*	ASTM D7264
Density measurements	5	10	10	ASTM D792
Fiber content measurements	5	10	10	ASTM D3171
Optical microscopy	2	10	10	N/A
Scanning electron microscopy	2	10	10	N/A
Micro computed tomography	1	55	13	N/A
Rheometry (torsion module)	2	55	13	ASTM D7028

**Length of the specimen depends on the thickness and varies for each laminate*

2.4.1 Optical Microscopy

A microstructural investigation is conducted to gather detailed microstructural information. As the first step, cut specimens are prepared and embedded in mounting resin that cures in room temperature (VersoCit-2), manufactured by Struers (Denmark). The mixing ratio is two parts of powder and one part of liquid. All three cross sections of four different specimens are embedded in the mounting material, facilitating easier handling during grinding, polishing, and examination. Prepared specimens are shown in Figure 2-13.



Figure 2-13: Prepared specimens. (a) surface to be investigated (b) rear surface and marking

Before microscopy investigation, polishing and grinding steps are performed. First, the rear surfaces of the specimens are ground to eliminate level differences between height and to obtain a smooth and flat surface. Oncethe rear surfaces are sufficiently flat, the investigation surfaces are polished and ground using a Forcimat 102 automatic grinder, manufactured by Metkon (Türkiye). This process is repeated for each specimen using 400, 600, 1200, and 2400 grit papers, with each step lasting 300 seconds. The grit papers are rotated at 250 rpms in the clockwise direction, while the

specimens are rotated at 50 rpms in the counterclockwise direction under a vertical foce of 10 N.

After specimens are neatly prepared, microstructural investigations are performed using a Nikon ECLIPSE MA100N stereo microscope and a Nikon SMZ 745T optical microscope. These investigations provide critical information such as yarn height and width, to be used in micromechanical material models. The captured images are analyzed using ImageJ software, and the necessary stereologic dimensions are measured and compiled for statistical analysis. Selected microscopy images are shown in Figure 2-14 and Figure 2-15. At least 50 measurements of height and width are taken for each material type. Measurements are presented in the Results and Discussion section.

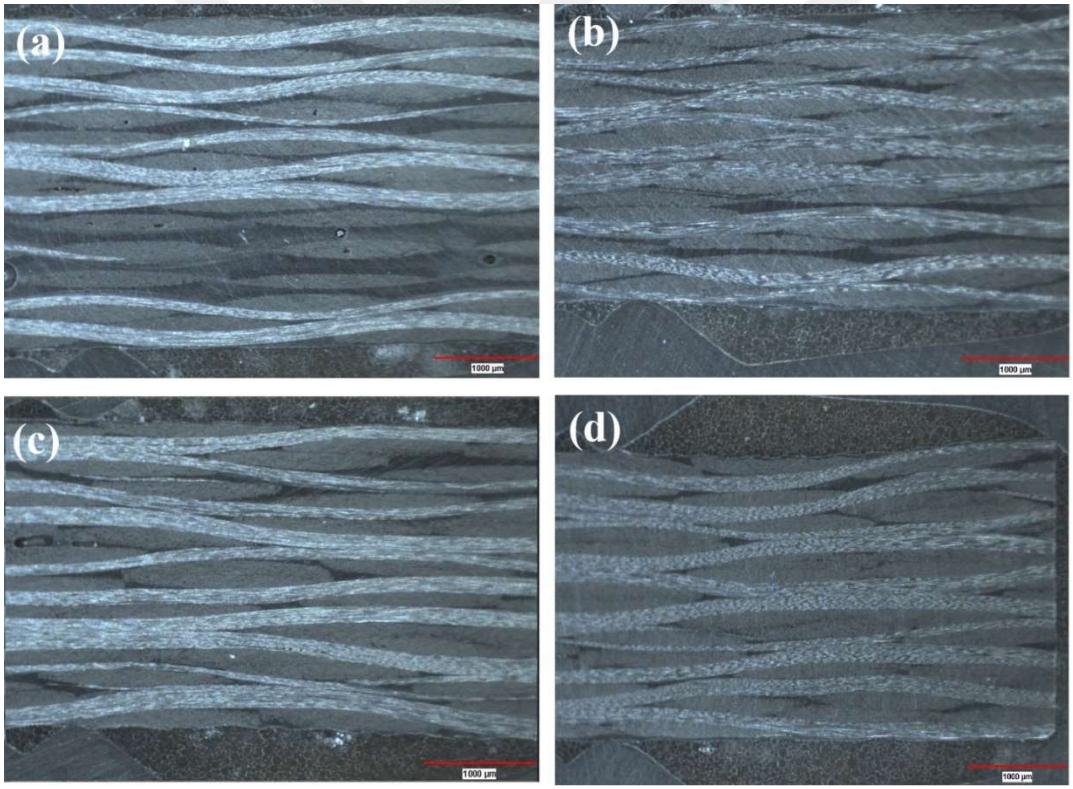


Figure 2-14: Microstructural images of cross sections for (a) plain woven fabric/epoxy composite from warp direction (b) plain woven fabric/epoxy composite from weft direction (c) twill woven fabric/epoxy composite from warp direction (d) twill woven fabric/epoxy composite from weft direction.

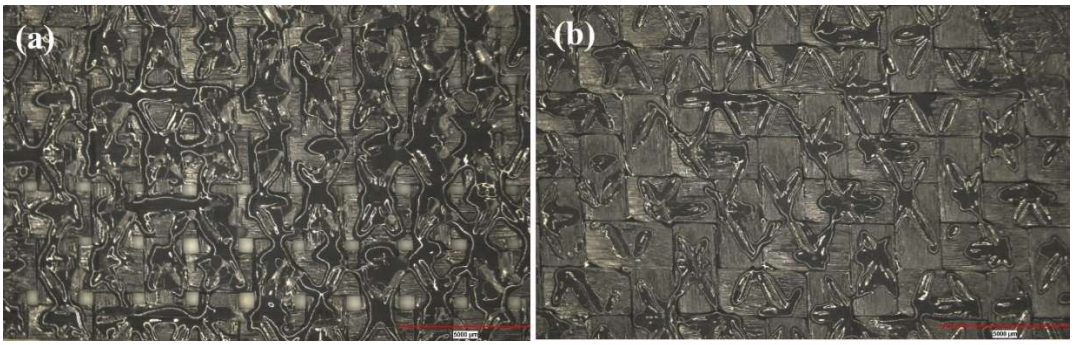


Figure 2-15: Microstructural images of prepreg materials from top view for (a) plain woven fabric/epoxy composite (b) twill woven fabric/epoxy composite

Experimental studies presented thus far aim to gather information and properties of the constituents for use in the micromechanical modeling section. Collecting accurate model inputs is crucial for creating and running reliable simulations, necessitating extensive characterization work.

2.4.2 Unidirectional Tensile Tests

The primary goal of this study is to predict elastic tensile properties of woven fabric-reinforced polymer matrix composites. Every modeling and simulation effort require verification and validation, with experimental methods being the most reliable for validation. To achieve this, unidirectional tensile tests are conducted. This section will detail the specimen preparation and tabulate the testing procedures.

Unidirectional tensile tests are conducted according to ASTM D3039 as mentioned in Table 2-5. All coupons are prepared to meet the requirements specified in this standard. The first step in coupon preparation involved cutting a rectangular plate with a height of 250 mm and a width of 210 mm. The height is determined according to the required coupon dimensions and width is determined by the number of coupons to be produced. For each laminate, eight tensile test coupons are planned. The dimensions of these coupons are also tabulated in Table 2-5.

After obtaining the rectangular composite plates, tabs are applied to the upper and lower edges. This process offers several advantages, including protection of coupons

from high grip loads, prevention of slippage during testing, and ensuring homogenous load distribution. The tab materials used are also glass fiber fabric/epoxy composites, attached to the coupons with either film or paste adhesives. In this study, Nema Grade G10 tabs with a width of 50 mm width and AF 163-2K film adhesive, manufactured by 3M (USA), are used.

The tabbing procedure starts with cutting the adhesive to match dimensions of the tabs, the surfaces of both the tabs and the composite plates place that will contact the adhesive are lightly ground with 400- grit sandpaper to increase surface area and improve adhesion. Next, the film adhesives are placed on the tabs, and the tabs are positioned on the composite plates using hand pressure. Once properly aligned, the assembly is compressed further using hydraulic pressure for 5 minutes to further enhance adhesion. Lastly, the tabs are secured, and the film adhesive is cured in an oven at 100°C for 1 hour. The tabbing procedure is shown in Figure 2-16.

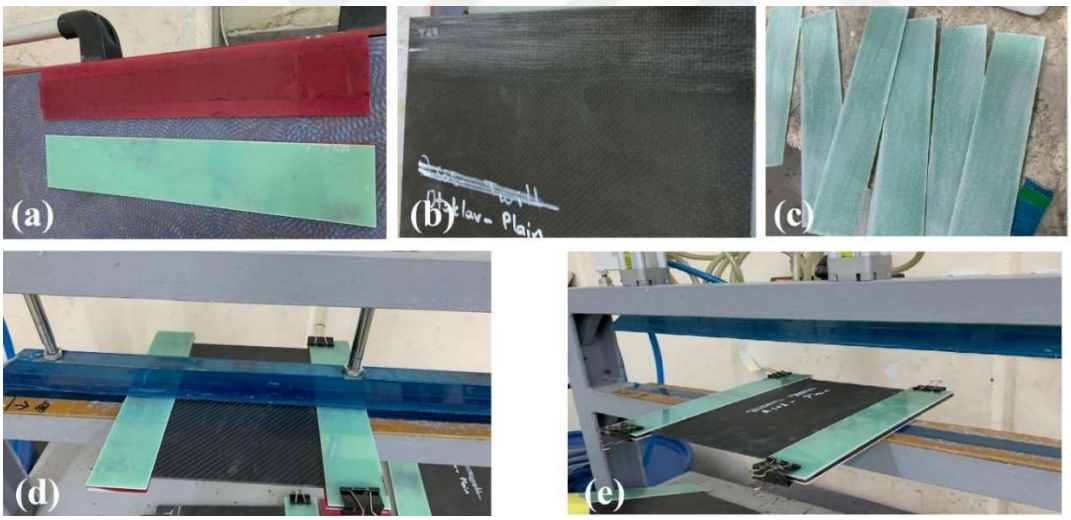


Figure 2-16: Tabbing steps (a) preparation of adhesive and tabs. (b) and (c) grinding of tabs and composite plates (d) and (e) applying pressure to consolidate adhesive before curing in oven

After the tabs are completely cured in the oven, the composite plate is sliced into tensile test coupons each with a width of 25 mm. The tensile tests are performed in the same manner as those for the epoxy resin, as described in Section 2.2.2. The same Digital Image Correlation (DIC) setup is used to capture strain data. A standard head

displacement of 2 mm/min is maintained throughout the tests. Six coupons are tested for each kind of laminate used in this study. Test setup and specimens are shown in Figure 2-17.

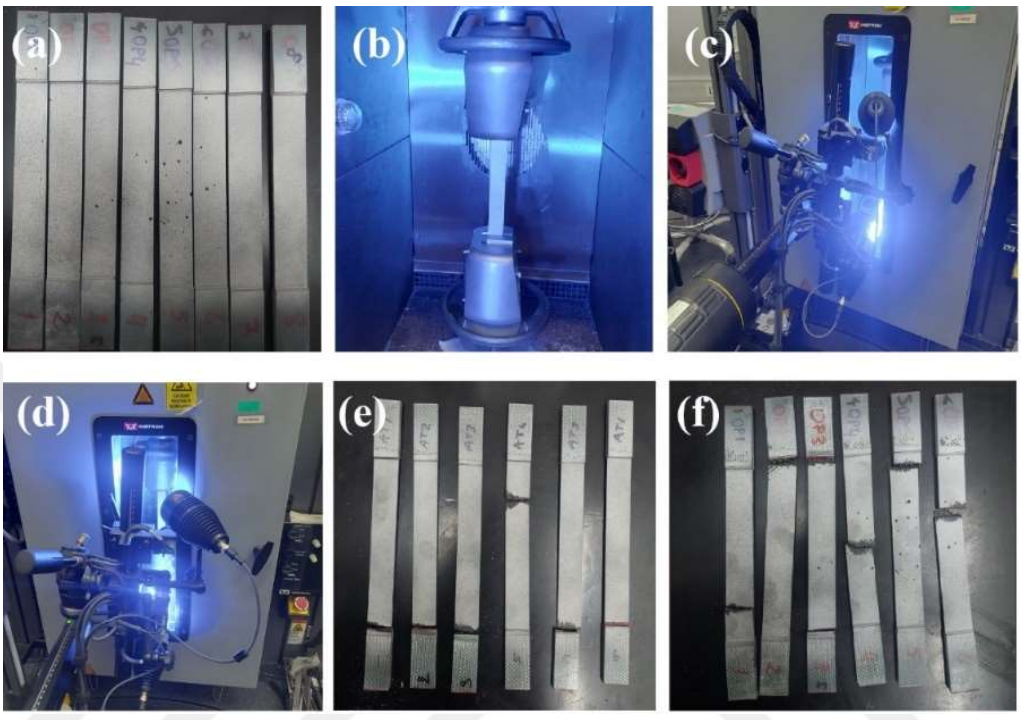


Figure 2-17: Unidirectional tensile testing of composite coupons (a) tensile test coupons (b), (c) and (d) tensile test and strain measurement setup (e) *A-T composite coupons* and (f) *A-P composite* coupons after completion of tests

2.4.3 3-Point Bending Tests

Bending loads are the most representative type of load for woven composites, as these materials are often subjected to bending stresses in their common applications. To characterize their bending and flexural performance and validate the finite element model and simulations, three-point bending tests are conduced according to ASTM D7264. This section outlines the specimen preparation and testing procedures.

For specimen preparation, a cutting saw, as previously described, is used. Eight specimens are tested for each material set. A support span-to-thickness ratio of 16:1

is chosen, resulting in a support span length of 45 mm for twill woven fabric/epoxy composites and 50 mm for plain woven fabric/epoxy composites. During testing, loads and displacements are recorded, with displacements measured based on the displacement of the Instron's own grips. The test specimens and setup are given in Figure 2-18.

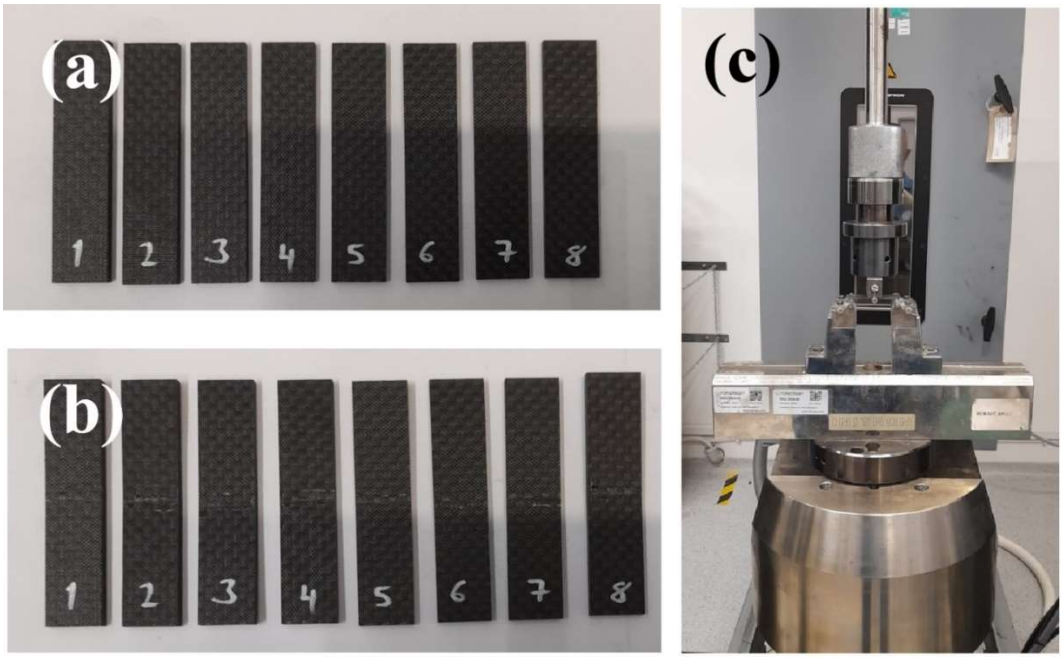


Figure 2-18: Bending test specimens and setup. (a) *V-P* specimens before the test (b) *V-P* specimens after the test (c) test fixture and setup

2.4.4 Density Measurements

Density measurements are performed prior to conducting constituent content measurements on five specimens for each material set using Archimedes method and a Mettler Toledo Balance XPR305DR with a density kit. These measurements are essential for determining theoretical fiber content and void fraction of the composites. Additionally, measuring the densities of specimens manufactured using

different curing techniques helps compare the consolidation levels of laminates. All the measurements are carried out in accordance with ASTM D792.

2.4.5 Fiber Content Measurements

Fiber or constituent content measurements are performed according to ASTM D3171 Test Method I, Procedure B, using an aqueous mixture of sulfuric acid and hydrogen peroxide. The procedure involves weighing the specimens, dissolving epoxy resin in the aqueous mixture on a hot plate, washing the remaining fibers with distilled water, drying of the fibers in an oven, and finally weighing the remaining fibers to compute the fiber weight content.

Fiber content measurements are conducted for all sets of materials, as well as for neat resin and neat fibers. The main goal of applying this procedure to neat resin is to ensure complete dissolution of the resin in the composite. For neat fibers, the goal is to quantify the amount of sizing. Sizing, a coating or a film layer around the fibers, enhances adhesion at the resin/fiber interface. It also serves as a lubricative layer during carbon fiber processing and protects the fibers from friction or other mechanical means [34, 35]. The fiber content measurement procedure is shown in Figure 2-19.

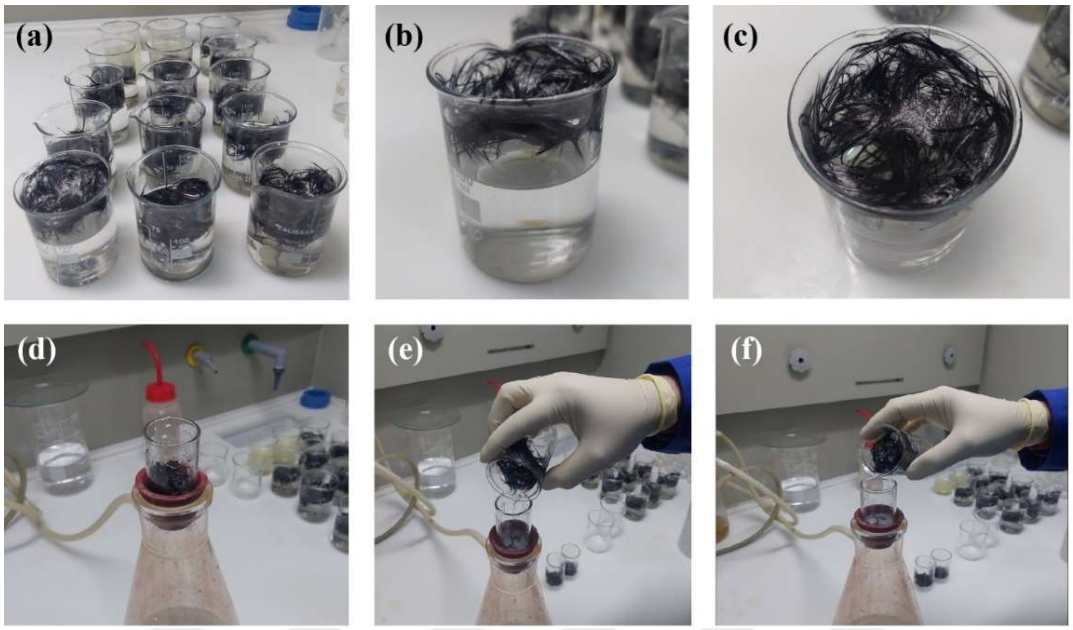


Figure 2-19: Application steps of fiber content measurement (a), (b) and (c) are remaining fibers after epoxy resin is completely dissolved (d), (e) and (f) are washing steps of the carbon fiber

2.4.6 Void Content Measurements

Void content measurements of composite laminates are conducted as per ASTM D2734-16 Test Method A. The procedure for calculating the void content is outlined as follows. Calculations are performed for five specimens from each laminate. To determine the void content, the theoretical density is first calculated using constituent densities and measured fiber weight fractions, as defined in Equation 2-1.

$$T_d = \frac{100}{\frac{R}{D} + \frac{r}{d}} \qquad (2-1)$$

In Equation 2-1, *R*, *r*, *D*, and *d* represent the weight percentage of resin, weight percentage of fiber, density of resin, and density of fiber, respectively. After the thoretical density is computed for each specimen, the void fraction is calculated using equation 2-2.

$$V = \frac{T_d - M_d}{T_d} * 100 \qquad (2-2)$$

V, T_d and M_d stand for voids (in percentage), theoretical density, and measured density, respectively.

2.4.7 Scanning Electron Microscopy (SEM)

Scanning electron microscopy (SEM) is exclusively utilized to measure fiber diameters in this study, as described in Section 2.2.1. SEM is chosen because optical microscopy lacks the resolution required at high magnification for accurate fiber diameter measurement. For this purpose, a Thermo Fisher Scientific (USA) Phenom XL Tabletop SEM is used. The specimens scanned for SEM analysis are the ones used in optical microscopy investigations.

2.4.8 Micro Computed Tomography (Micro-CT)

A statistical void analysis is performed on four laminates to investigate how void amount, distribution, orientation, and shape change with processing parameters and the type of woven fabric used. For this analysis, a Comet Yxlon (Germany) FF85CT micro computed tomography device equipped with a directional micro-focus tube and a flat panel detector is used. Specimens of all four material sets are examined.

The scan voltage and tube current are set to 80.0 kV and 900 μA, respectively. Scans average 90 minutes, with 0.1° rotation step and an exposure of 1.5 seconds per step. The scans are reconstructed using VGSTUDIO MAX software to analyze the structures. By employing the porosity/inclusion analysis module of the software, both quantitative and qualitative analysis of the voids are conducted. Minimum voxel resolution for the scans is 25 μm. For a proper void study, lower voxel resolutions can be further aimed but for better resolution, nanofocus tubes with lower scanning voltages can be used.

The pore analysis provides data on void characteristics such as radius, volume, spatial location, surface area, and projected lengths in three directions. From these measurements, parameters such as sphericity, spatial distribution, elongation factors, and roundness of cross sections are computed and presented in detail in the Results and Discussion section.

2.4.9 Glass Transition Temperature Measurements using Rotational Rheometer Analysis with Torsion Module

The glass transition temperature (Tg) is an important material property used to verify whether a composite material is fully cured. For this purpose, two specimens from each laminate are analyzed using rotational rheometer with a built-in torsion module in accordance with ASTM D7028. Specimens measuring 55 mm in length and 13.7 mm in width are used in thethermal analyses. During the tests, the heating rate is maintained at 5°C/min, with a loading frequency of 1 Hz, and a strain rate of 0.01%. The shear modulus is constantly measured, and the transition region, observed as temperature increased, is used to determine the glass transition temperature (Tg).

CHAPTER 3

RESULTS AND DISCUSSION

In this study, two types of woven carbon fabric (plain and twill woven) reinforced epoxy matrix prepreg are used. First, the epoxy matrix is mechanically and physically characterized to obtain necessary mechanical properties for modeling and simulation work. For the carbon fiber properties, technical data sheet information is used since necessary testing equipment was unreachable. Second, composite laminates are manufactured, a micromechanical characterization is performed to obtain microstructural information. Finally, a mechanical and physical characterization to composite coupons is conducted to validate the models developed. Naming and labeling of the material types are same with the one in the Experimental Work section.

- **V-P**: **V**acuum oven cured **p**lain woven fabric/epoxy composite
- **V-T**: **V**acuum oven cured **t**will woven fabric/epoxy composite
- **A-P**: **A**utoclave oven cured **p**lain woven fabric/epoxy composite
- **A-T**: **A**utoclave oven cured **t**will woven fabric/epoxy composite

3.1 Constituent Characterization

Uniaxial tensile tests are performed on six epoxy resin coupons according to ASTM D638-14. Results of these tests are given in Figure 3-1 and tabulated in Table 3-1.

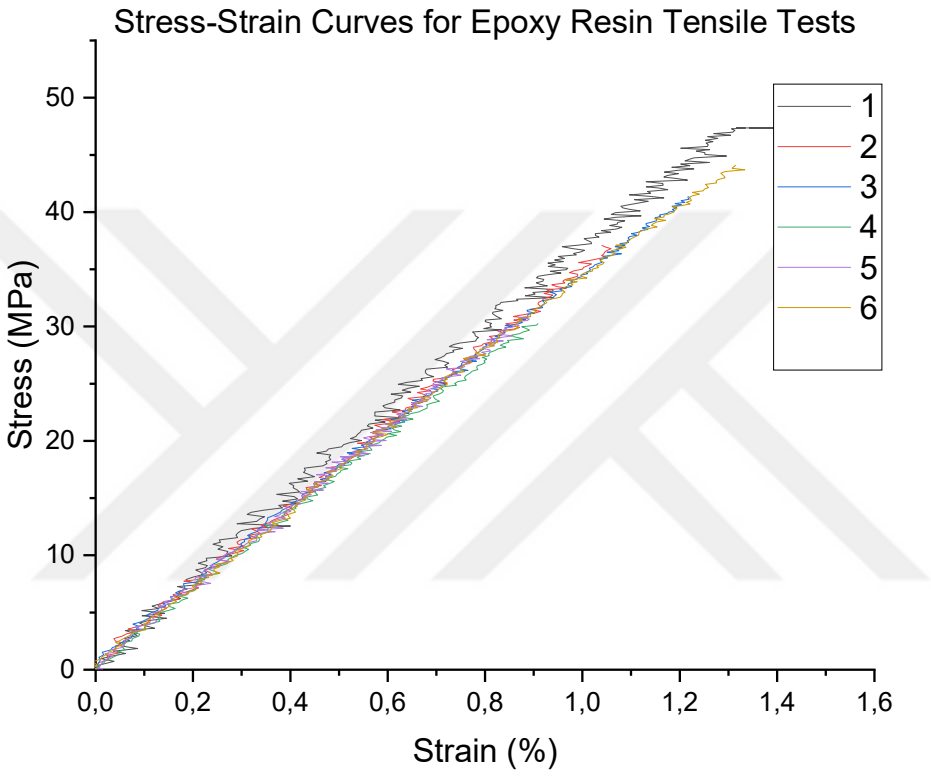


Figure 3-1: Stress-strain curves for epoxy resin tensile tests

Table 3-1: Ultimate tensile strength, strain, elastic modulus and Poisson's ratio values for epoxy resin

	Ultimate Tensile Strength [MPa]	Ultimate Tensile Strain [%]	Elastic Modulus [GPa]	Poisson's ratio
1	47.41	1.41	3.52	0.39
2	37.16	1.06	3.46	0.38
3	41.42	1.22	3.35	0.38
4	30.26	0.91	3.36	0.36
5	31.18	0.89	3.46	0.37
6	44.11	1.33	3.36	0.37
Average	38.53	1.14	3.42	0.38
SD	5.91	0.18	0.06	0.01
CoV [%]	15.27	16.25	1.76	2.03

The average ultimate tensile strength and strain are found to be 38.5 MPa and 1.14 %, respectively, which are within the expected range for the materials. However, the coefficient of variation for these is higher than anticipated as indicated in Table 3.1. This variability is consistent with high-T_g resins and fully cured degree epoxy resins, as stated in [39].

The parameters required for the modeling study, elastic modulus and Poisson's ratio, are measured to be 3420 MPa and 0.375, respectively. Measured properties for the structural epoxy resin are as anticipated and compatible with other commercially available similar resins.

Also, a density measurement for the epoxy resin is conducted and results are tabulated in Table 3-2. Also, the density measurement gives a result consistent with the other epoxy resins used for similar applications. There might be a difference in densities of neat epoxy resin measured and epoxy in the prepreg due to different production routes, however this difference is evaluated to be minimal and neglected.

Table 3-2: Density measurements for epoxy resin

Specimen	Density
1	1.188
2	1.190
3	1.188
4	1.191
5	1.190
Average	1.189
SD	0.001
CoV [%]	0.101

As mentioned before, any mechanical characterization to carbon fibers is not conducted and manufacturer technical data sheet information is used for the models. This data is tabulated in Table 2-1 [40].

3.2 Microstructural Investigation

3.2.1 Microstructural Investigation Using Optical Microscopy

As described in Section 2.4.1, a microscopic investigation of all four different sets of specimens in warp and weft direction is conducted and results are presented and discussed in this section. First, warp and weft widths are determined, as shown in Figures 3-2 and 3-3 for plain woven and twill woven fabrics, respectively. Statistical results are tabulated in Table 3-3.

Table 3-3: Warp and weft widths for both fabrics

	Plain Fabric		Twill Fabric	
	Warp width [µm]	**Weft width [µm]**	**Warp width [µm]**	**Weft width [µm]**
Average	1556.3	1641.8	1693.8	1697.6
CoV [%]	3.7	8.4	2.6	4.6

When Table 3-3 is investigated, it is seen that warp and weft dimensions for the twill fabric are almost identical. In contrast, for plain fabric, warp yarns are approximately 5.5% narrower than the weft yarns. This difference arises from the fabric weaving process. During weaving, warp yarns are subjected to tension while weft yarns are woven around them. The smaller difference observed in twill fabric is attributed to the lower tension forces during its processing [41, 42].

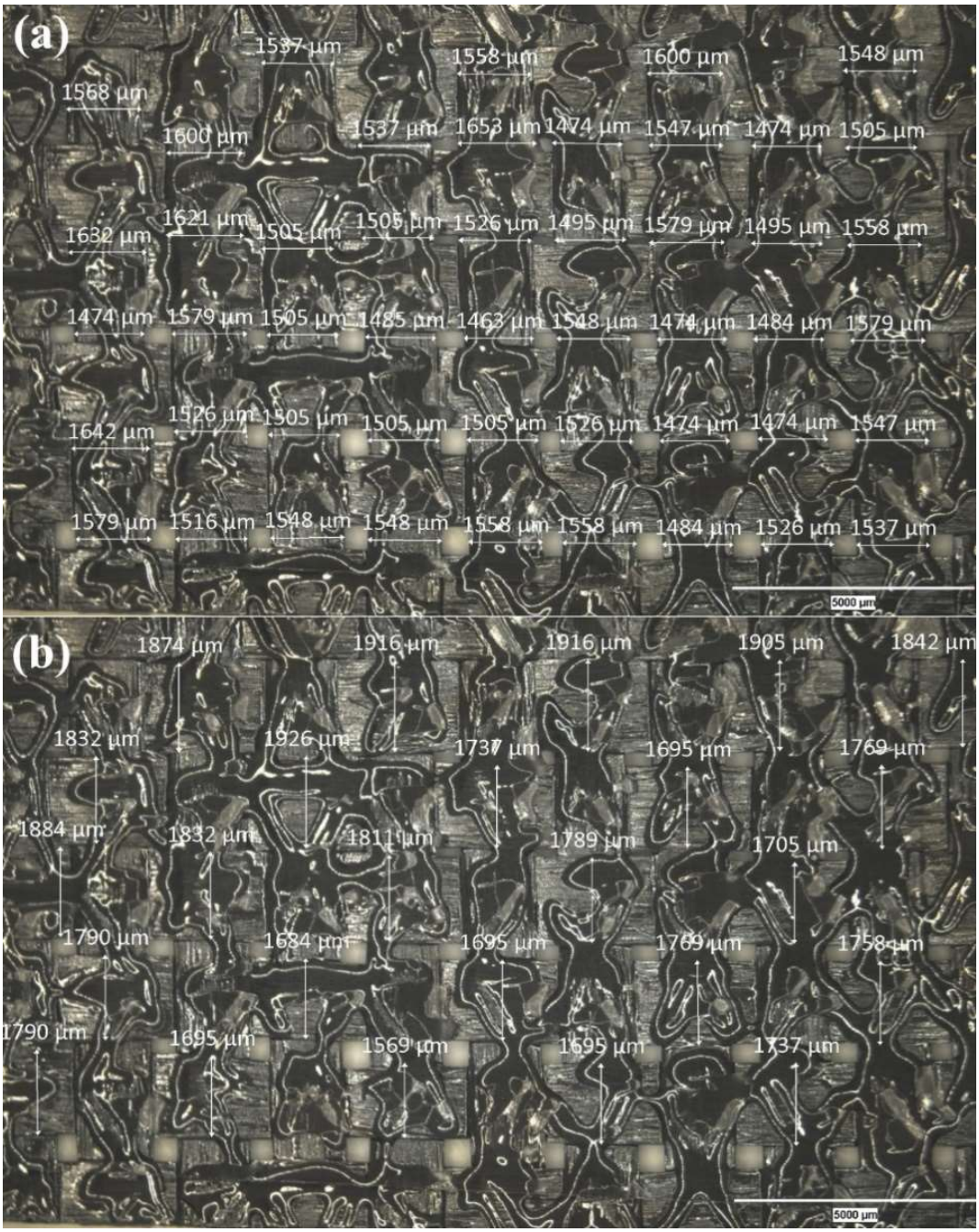


Figure 3-2: Yarn width measurements for (a) warp yarns of plain woven fabric, (b) weft yarns of plain woven fabric

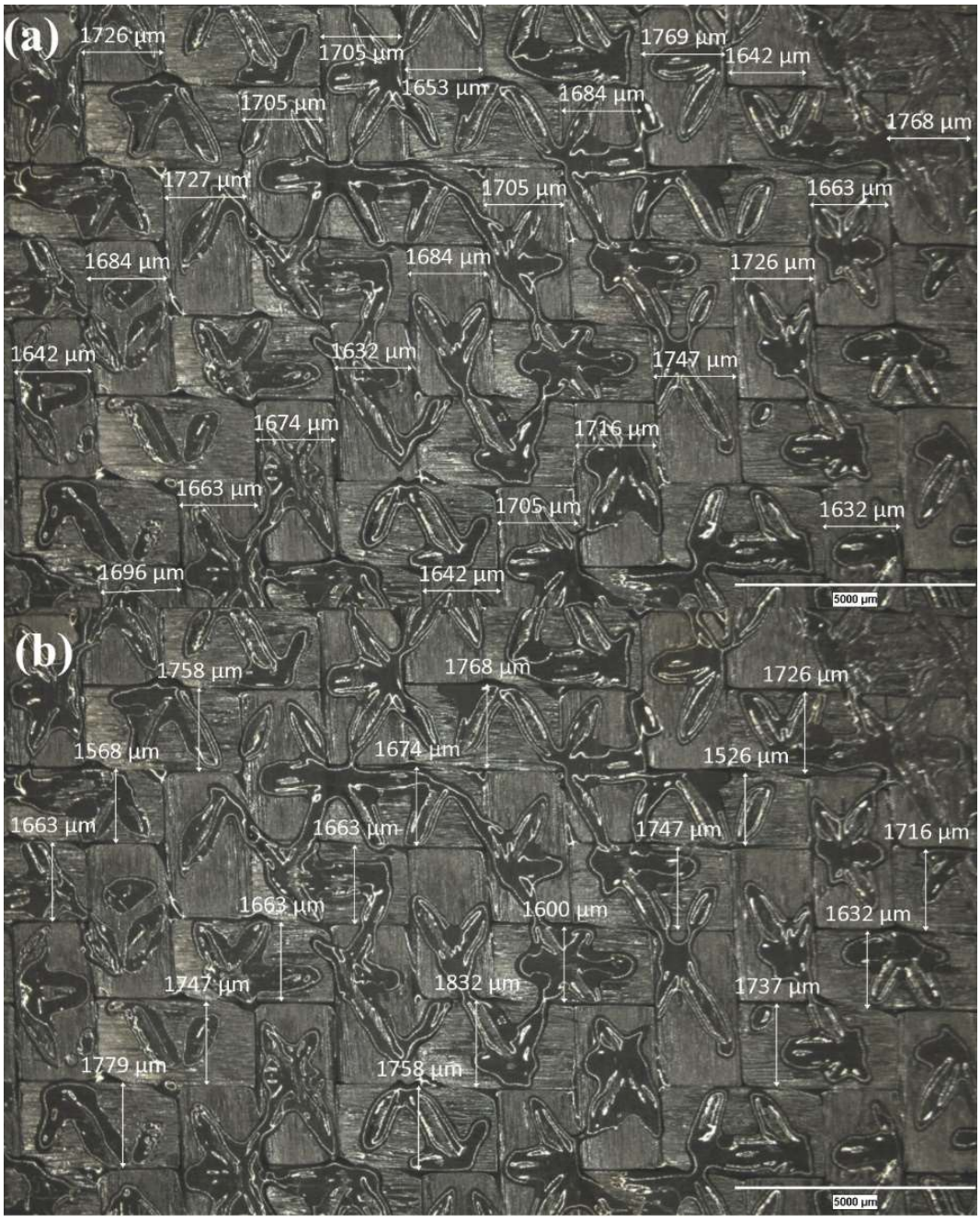


Figure 3-3: Yarn width measurements for (a) warp yarns of twill woven fabric and (b) weft yarns of twill woven fabric

After determining the yarn widths, the cross-sectional geometries of the yarns were examined under an optical microscope to measure the height and width of the cross sections. Bakelite-mounted specimens are used for these measurements. Figures for cross section measurements of yarns from both warp and weft direction for all sets

of materials are presented in Appendix C. The results for these parameters are summarized in Tables 3-4 and 3-5.

Table 3-4: Warp and weft dimensions for plain woven fabric composites

	Warp		Weft	
	Height [µm]	**Width [µm]**	**Height [µm]**	**Width [µm]**
Vacuum	159.1	1601	155.2	1651.6
Autoclave	151.1	1621.2	152.1	1677.3
Difference [%]	-5.03	1.26	-2.00	1.56

Table 3-5: Warp and weft dimensions for twill woven fabric composites

	Warp		Weft	
	Height [µm]	**Width [µm]**	**Height [µm]**	**Width [µm]**
Vacuum	159.2	1670.2	146.4	1705.6
Autoclave	140.2	1722.4	141.9	1733.2
Difference [%]	-11.90	3.13	-3.06	1.62

As shown in Tables 3-4 and 3-5, a decrease in height and an increase in the width of the yarns are observed in autoclave specimens compared to vacuum specimens. This phenomenon is attributed to the high pressure applied during autoclave curing and is expected.

3.2.2 Fiber Diameter Measurements by SEM

Fiber diameter is another key input parameter for the micromechanical models. Measurements are conducted on the cross-sections of the mounted materials. Since both plain and twill woven fabrics are produced from the same batch, a single average fiber diameter is calculated for both. The average fiber diameter is found to be 6.84 µm.

While most fibers have circular geometry, some anomalies with elliptical or non-circular geometries are observed. These anomalies may arise during melt-spinning

process, where fibers are melt-spun and extruded into molds. Variations in the extrusion process, such as irregular openings, can affect the fiber geometry [43]. Although differences in fiber cross-section geometry can influence mechanical performance, they are assumed negligible for the purpose of this study, and all fibers are modeled as circular. The fiber cross-sections of fibers are shown in Figure 3-4.

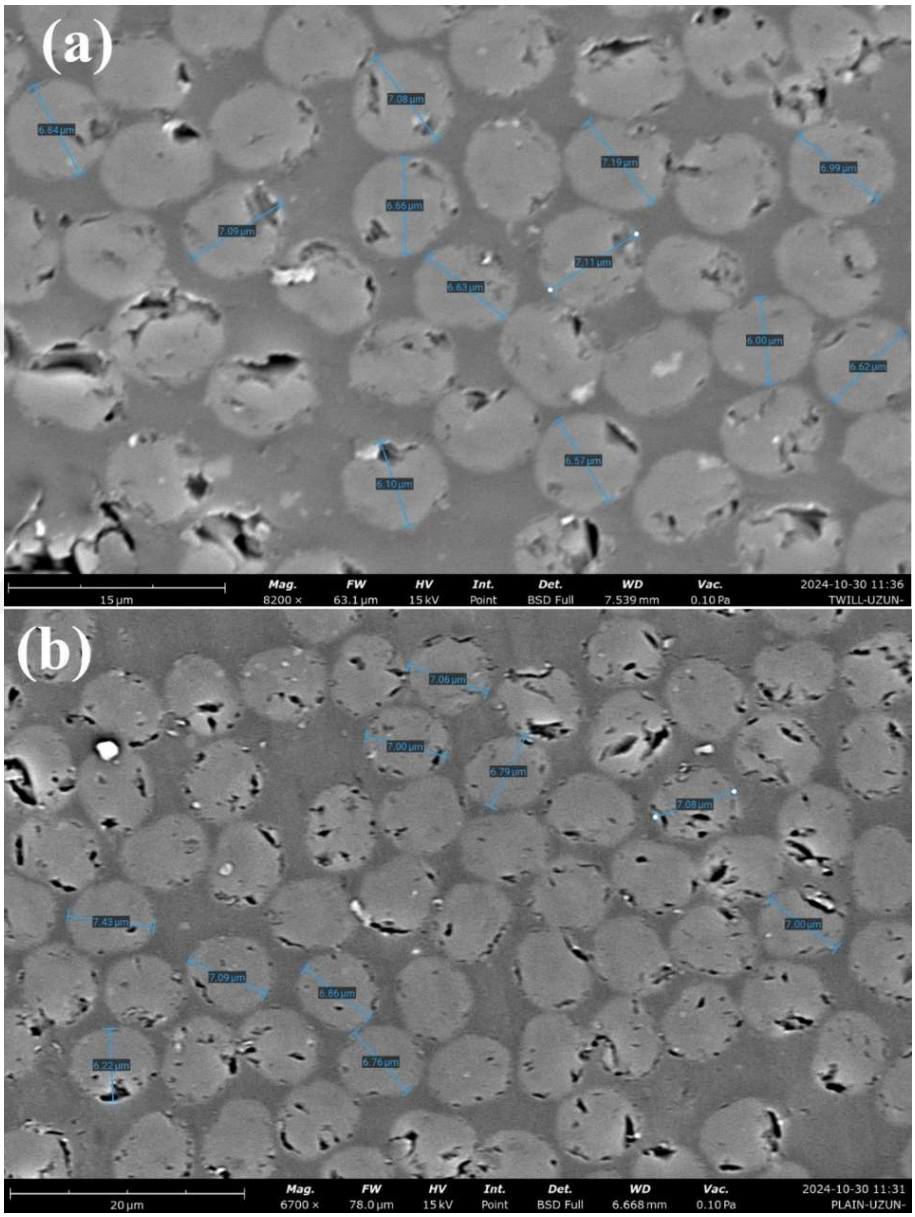


Figure 3-4: Fiber diameter measurements from different regions of materials.

3.2.3 Void Analysis Using Micro-CT

To assess the effect of different curing routes and fabric types on void amount, distribution, and morphology, computed micro tomography scans are performed and analyzed. The results of these scans are presented below.

All voids are assumed to have an elliptical shape, with their semi-major, semi-medium, and semi-minor axes are determined first. The volume of each void is also calculated. Morhological factors, such as elongation and cross-sectional roundness, are also computed and tabulated. A detailed statistical analysis of voids for all laminates is given in Appendix A.

3.2.3.1 Void Size Analysis

The void analysis procedure begins by categorizing voids based on their semi-major, semi-medium, and semi-minor axes. Through an assignment process, each void is individually identified and distinguished, and the sizes of characteristic axes are measured. A representation of voids showing their semi-major, semi-medium, and semi-minor axes is provided in Figure 3-5. The distribution of semi-major, semi-medium, and semi-minor axis lengths are given in Figures 3-6, 3-7, and 3-8, respectively.

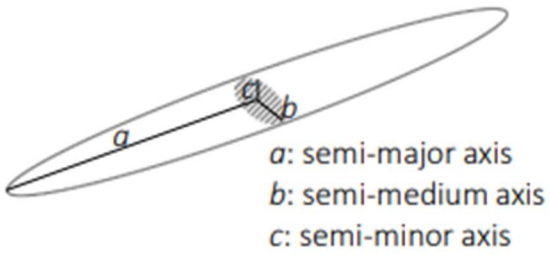


Figure 3-5: Elliptical voids and its axes representation [44]

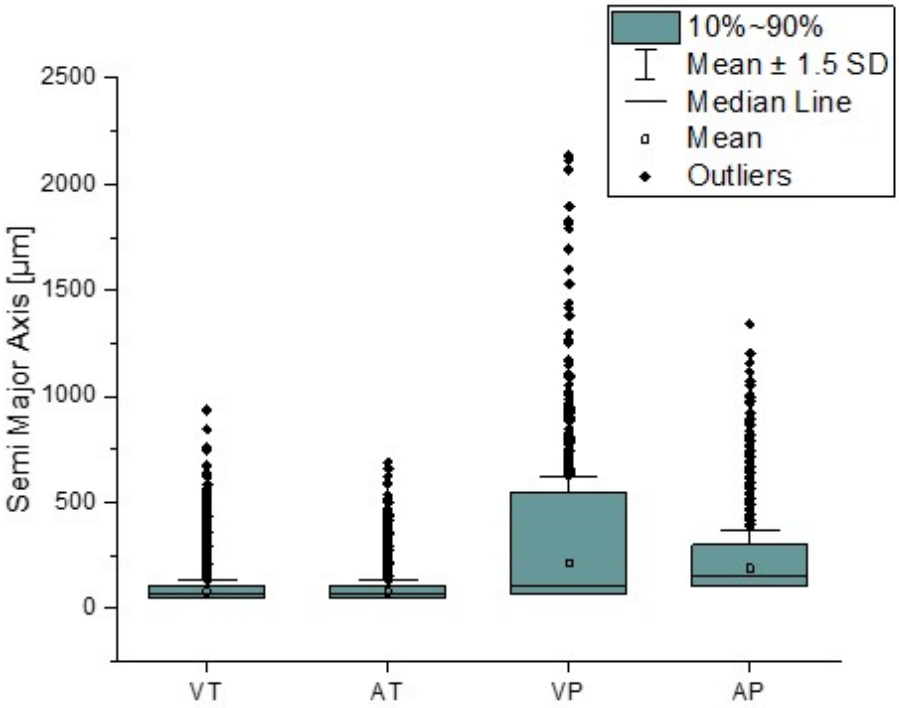


Figure 3-6: Semi major axis length distribution for all laminates

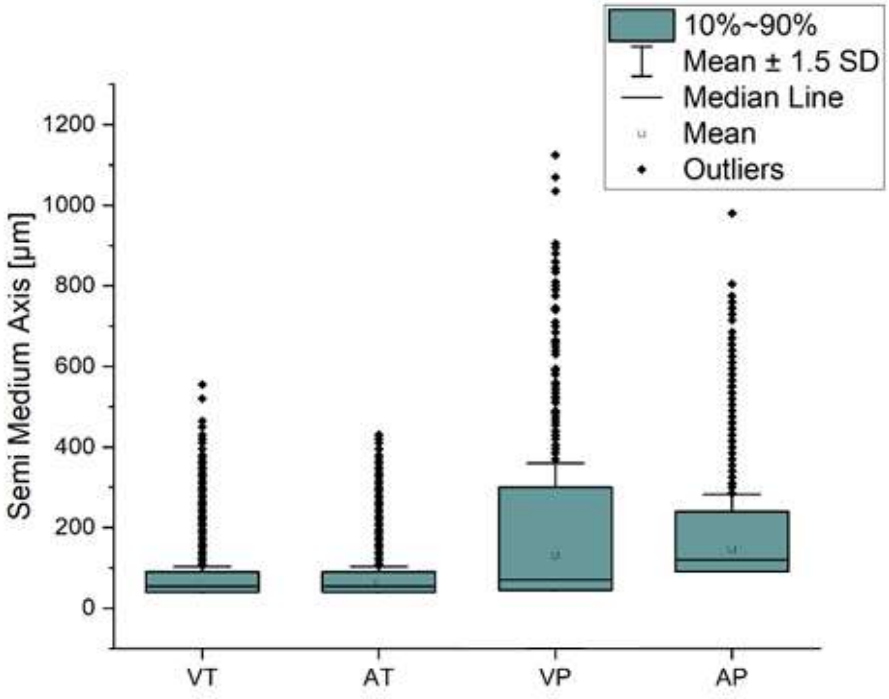


Figure 3-7: Semi medium axis length distribution for all laminates

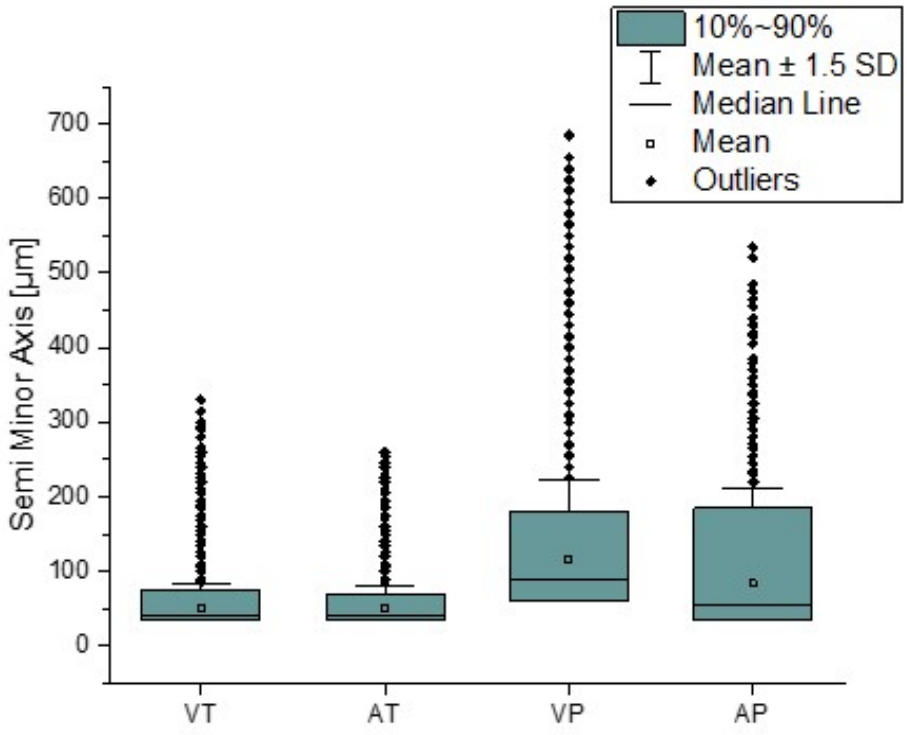


Figure 3-8: Semi minor axis length distribution for all laminates

Statistics about voids are given in box chart plots. In the Figures 3-6 to 3-10, boxes represent data points that fall between 10% and 90% when a sorting is made according to values. Line inside the box represents median value whereas square represents the mean value. Data points that stand higher than the standard deviation line is called outliers which are not compatible with the main data. Consistent trends are observed in the size analyses of voids across all three characteristic length distributions. The void sizes in plain woven laminates are significantly larger than those in twill woven laminates. This difference is primarily attributed to the capillary number and resin flow characteristics, which are affected by the fabric structure [45]. Plain weaves typically have a more open structure between interlacing yarns and adjacent plies, leading to formation of larger voids compared to twill weave. It is also stated by Anda et al. [46] that fabrics with higher threads per inch (TPI) tend to have smaller pores. The twill fabric studied in this work has a higher TPI than the plain fabric.

3.2.3.2 Void Shape Analysis

A statistical analysis procedure of void shapes is performed to evaluate their influence on mechanical properties. The results of this analysis are later incorporated into material models. In this study, the aspect ratio serves as a key input parameter for material modeling, and aspect ratio distribution is created for all four sets of materials. To represent the aspect ratio of void volumes, two parameters are introduced: the geometric mean of transversal axes and elongation factor.

The geometric mean of transversal axes represents the cross-sectional area of voids in the longitudinal direction. It is chosen over the arithmetic mean because mathematically, a circle with a radius equal to the geometric mean of transversal axes of an ellipse has the same cross-sectional area [44]. The elongation factor, defined as the ratio of the semi major axis to the geometric mean of transversal axes, represents the aspect ratio for this analysis. The distribution of the geometric mean of transversal axes and elongation factor values for all laminate sets are shown in Figures 3-9 and 3-10.

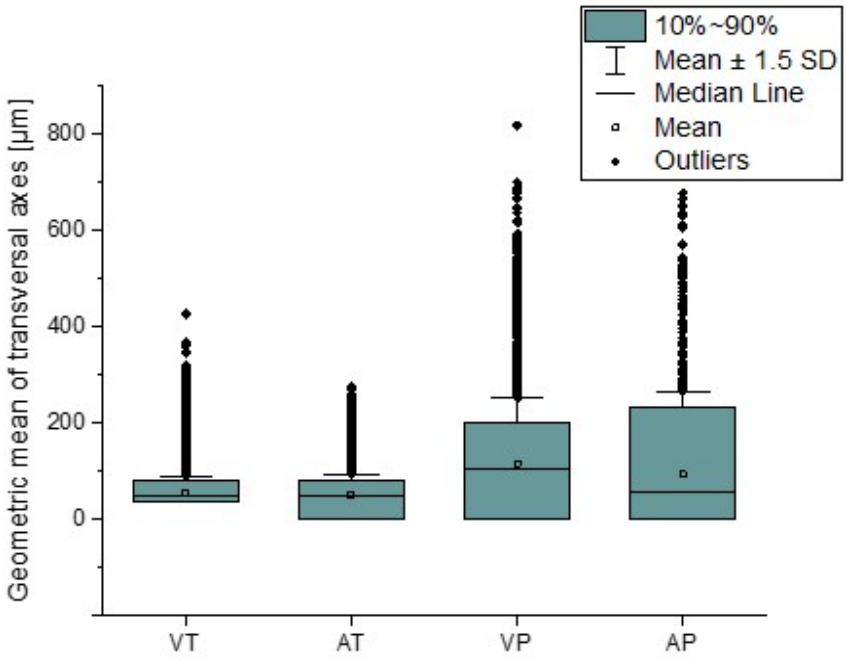


Figure 3-9: Geometric mean of transversal axes distribution for all laminates

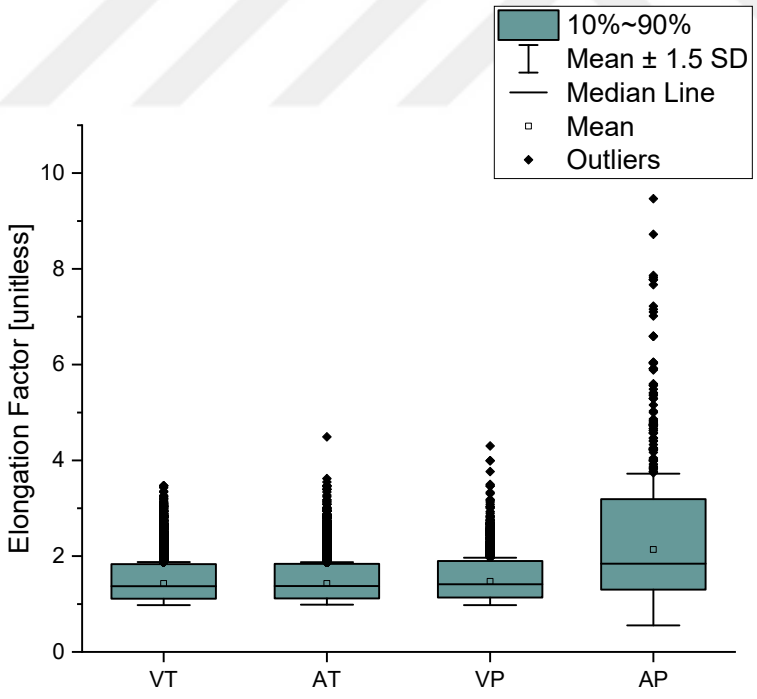


Figure 3-10: Elongation factor distribution for all laminates

The results from Figures 3-9 and 3-10 indicate that voids of plain-woven laminates have larger cross-sections compared to twill woven laminates. This observation aligns with the size analysis of voids in the previous section, where the underlying reasons for this phenomenon are discussed. When comparing voids across curing media, it is evident that voids in autoclave-cured laminates are more elongated in both materials. This effect is more apparent in plain woven laminates and can be explained as follows. Plain woven laminates have a more open structure compared to twill woven laminates, providing greater space between the fibers or yarns. This openness creates larger areas where voids can form. During the curing process, external pressure, as in autoclave curing, and heat compress or reshape these voids. In an open structure like a plain weave, the surrounding materials provide less constraint on voids, allowing them to deform more and elongate more freely under pressure. As a result, autoclave-cured laminates exhibit more elongated voids, with the effect being more pronounced in plain woven laminates due to their more open srturcute.

In this study, elongation factor values are treated as a parameter analogous to the aspect ratio and are implemented to micromechanical models. A binning method is used to categorize voids nased on their elongation factor. For each material, ten bins are defined, and the relative frequency of voids in each bin is evaluated. The results for plain woven and twill woven laminates are presented in Figures 3-11 and 3-12, respectively. The analysis shows that most captured voids have smaller elongation factors, while voids with larger elongation factors are rare and often absent from the distribution histograms, indicating that the majority of voids have a shape resembling a circle.

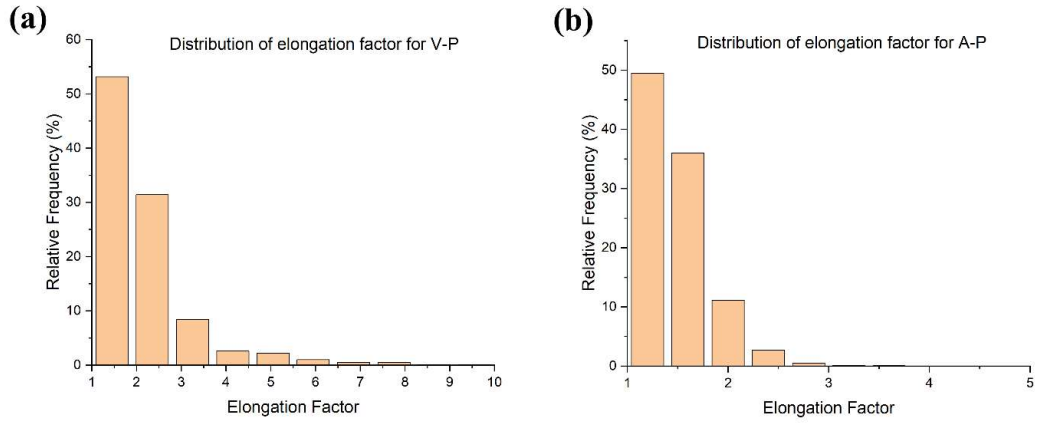


Figure 3-11: Elongation factor distributions for V-P and A-P

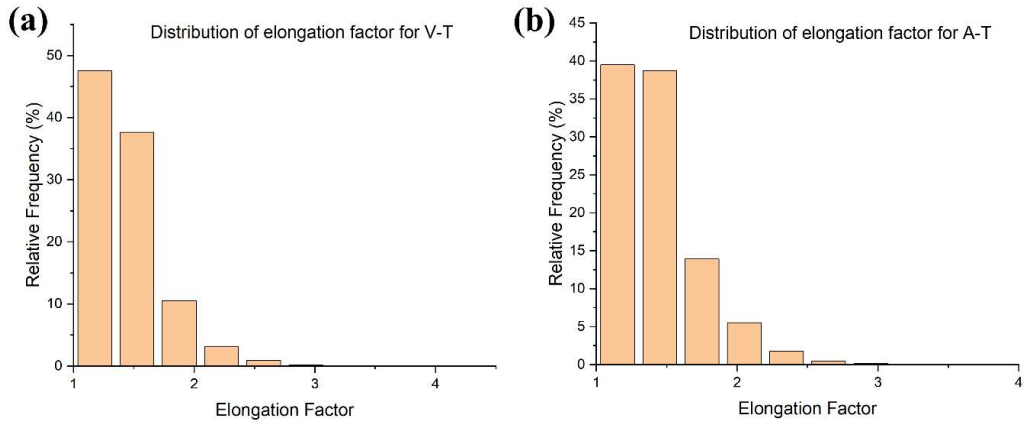


Figure 3-12: Elongation factor distributions for V-T and A-T

3.2.3.3 Void Orientation Analysis

Void orientation studiues are typically conducted by projecting all voids onto three orthogonal axes, with the orientation determined by the direction of the major axis. In fibrous composite materials, voids are generally aligned along the nominal fiber directions due to thermal loadings during heating, curing, and cooling, which arise from the mismatch in thermal properties of resin and fiber.

In this study, void orientations could not be computed accurately because voids have small aspect ratios and lack a distinct orientation bias. Therefore, an alternative methodology is adopted for simulation. For the implementation of the voids, A lower-upper boundary approach is implemented, where the lower boundary assumes all voids are oriented perpendicular to loading direction, and the upper boundary assumes all voids are oriented parallel to the loading direction.

3.3 Composite Characterization

Finally, extensive characterization work is performed on the manufactured composite laminates to determine their mechanical and physical properties and validate the developed models. In this section, the obtained results are tabulated and discussed.

3.3.1 Physical Properties of Composites

In this section, the density and fiber content measurements of the manufactured laminates are presented and discussed. The results for composite density and fiber weight fraction measurements are provided in Table 3-6.

Table 3-6: Density, fiber weight and fiber volume fraction measurements of composites

Laminate	Density [g/cm3]	Fiber Weight Fraction [%]	Fiber Volume Fraction [%]
V-P	1.419 ± 0.004	50.96 ± 0.59	40.99 ± 0.56
A-P	1.454 ± 0.004	53.04 ± 1.10	43.02 ± 1.09
V-T	1.469 ± 0.003	56.50 ± 0.24	46.47 ± 0.24
A-T	1.489 ± 0.004	59.00 ± 0.39	49.03 ± 0.39

It is observed that curing composite laminates under high pressure in autoclave curing effectively reduces excess voids in the materials. This reduction in void content leads to an increase in density and fiber weight fraction for 4.96% and 4.08%,

respectively, for plain woven composites. For twill woven composites, the corresponding increases are 1.36% and 4.42%, respectively. The difference between the increasing ratio of density in plain woven and twill woven composites can be attributed to the more open structure in plain composites allowing for more significant void reduction under pressure. On the other hand, the tighter structure of the twill weave composites naturally results in fewer voids initially. While high-pressure curing still improves the material, the change is less pronounced because the baseline void content is already lower.

The increase in density can be attributed to the reduction in void volume within the material; however, the increase in fiber weight fraction requires investigation. The primary reason for this phenomenon is the higher compaction forces during autoclave curing, which results in some resin being absorbed by consumables used in the vacuum bagging process, such as peel ply and breather fabric [47]. Furthermore, some of the resin is removed during the curing process itself. Given that the initial resin content and fiber content in both types of laminates are relatively similar, these results suggest that the relative amount of resin at similar rates in both plain and twill laminates. This removal equally increases the proportion of fiber mass, even though the changes in structural density differ.

The increase in density and fiber weight fraction is expected to enhance the mechanical properties of woven laminates. Additionally, void volumes are determined experimentally using density and fiber weight fractions of composites. Results are tabulated in Table 3-7.

Table 3-7: Void content measurements for laminates

Specimen	V-T	A-T	V-P	A-P
1	1.15	1.04	2.26	0.77
2	1.10	1.02	2.88	1.28
3	1.57	0.93	2.17	1.06
4	1.65	0.81	2.46	0.82
5	1.22	1.46	2.88	1.10
Average [%]	1.34	1.05	2.53	1.01

3.3.2 Tensile Properties of Composites

In this section, the tensile test results of composite coupons are presented. These results are primarily used to validate material models and simulations. Additionally, the differences in mechanical properties caused by different processing routes are analyzed and discussed. Tensile test results for vacuum oven and autoclave cured woven plain composites are tabulated in Tables 3-8 and 3-9, respectively. Stress strain curves of corresponding materials are shown in Figure 3-13.

Table 3-8: Tensile test results for vacuum oven cured plain woven composite

VP	Ultimate Tensile Strength [MPa]	Ultimate Tensile Strain [%]	Elastic Modulus [GPa]	Poisson's Ratio
1	435.8	0.94	38.41	0.0703
2	483.1	1.03	37.92	0.0707
3	518.1	1.05	42.76	0.0664
4	540.3	1.06	40.67	0.0609
5	498.4	1.05	44.96	0.0536
6	478.4	0.98	46.93	0.0556
Average	492.4	1.02	41.94	0.0629
SD	30.43	0.04	3.05	0.0062
CoV [%]	6.18	3.77	7.26	9.90

Table 3-9: Tensile test results for autoclave cured plain woven composite

AP	Ultimate Tensile Strength [MPa]	Ultimate Tensile Strain [%]	Elastic Modulus [GPa]	Poisson's Ratio
1	548.1	1.18	46.33	0.0665
2	555.8	1.19	49.33	0.0643
3	523.0	1.11	47.76	0.0672
4	550.6	1.17	47.06	0.0731
5	518.4	1.10	45.73	0.0779
6	556.8	1.19	45.42	0.0742
Average	542.1	1.16	46.94	0.0705
SD	14.34	0.03	1.23	0.0045
CoV [%]	2.64	2.82	2.61	6.35

Analysis of the results revealed that, compared to vacuum oven curing, the ultimate tensile strength, ultimate tensile strain, and elastic modulus of autoclave-cured plain woven laminates increase by 10.11%, 13.63% and 11.91%, respectively. Since the fiber volume fraction only increases 4.08% in autoclave curing, it can be concluded that the improvement in mechanical properties is not solely attributable to this factor. The lower void volume fraction in autoclave-cured laminates, as shown in Table 3-8, also contributes significantly to enhanced mechanical reliability, as the variations in properties are considerably smaller. These findings indicate that, compared to vacuum oven curing, autoclave curing not only improves mechanical properties but also reduces variations within the laminate, resulting in a more reliable structure.

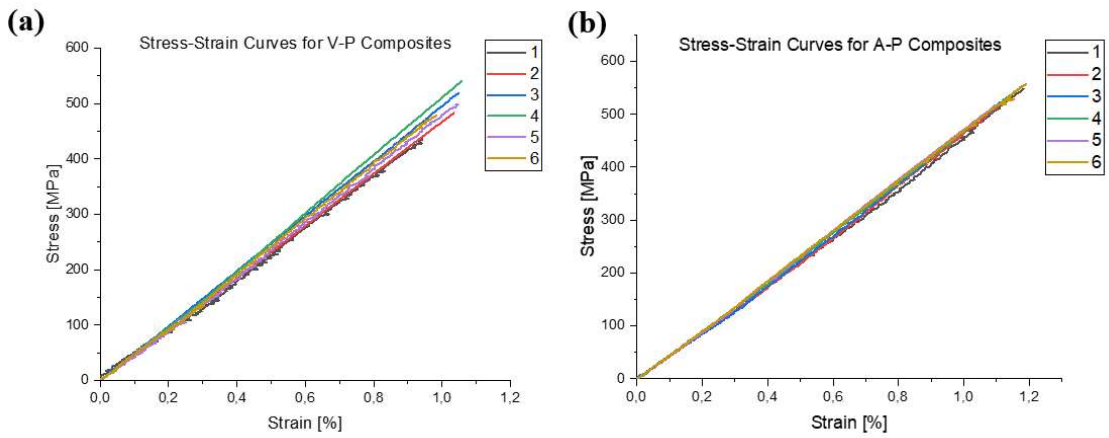


Figure 3-13: Stress-strain curves for plain woven composites (a) vacuum oven cured, (b) autoclave cured

Tensile test results for twill woven fabrics are also analyzed for both curing media. The results for vacuum oven-cured (V-T) and autoclave-curved (A-T) are given in Tables 3-11 and 3-12, respectively. The corresponding stress-strain curves are shown in Figure 3-14.

Table 3-10: Tensile test results for vacuum oven cured twill woven composite

VT	Ultimate Tensile Strength [MPa]	Ultimate Tensile Strain [%]	Elastic Modulus [GPa]	Poisson's Ratio
1	670.1	1.24	50.82	0.0731
2	720.1	1.29	52.12	0.0597
3	643.9	1.12	50.33	0.0454
4	627.9	1.13	52.13	0.0506
5	620.6	1.12	52.99	0.0537
6	566.3	1.04	51.75	0.0598
Average	641.5	1.16	51.69	0.057
SD	43.56	0.08	0.82	0.01
CoV [%]	6.79	6.69	1.58	14.22

Table 3-11: Tensile test results for autoclave cured twill woven composite

AT	Ultimate Tensile Strength [MPa]	Ultimate Tensile Strain [%]	Elastic Modulus [GPa]	Poisson's Ratio
1	610.3	1.11	53.17	0.0577
2	632.1	1.13	55.34	0.0487
3	690.3	1.22	52.18	0.0612
4	692.8	1.22	54.61	0.0536
5	698.0	1.23	51.78	0.0533
6	674.9	1.17	52.57	0.0611
Average	666.4	1.18	53.28	0.056
SD	30.85	0.05	1.19	0.00
CoV [%]	4.63	3.87	2.24	7.47

Autoclave curing results in a 3.88%, 1.72%, and 3.08% increase in ultimate tensile strength, ultimate tensile strain, and elastic modulus, respectively, while Poisson's ratio decreases by 1.75%. The improvement in this material is not as significant as those observed in plain woven composites. This is attributed to the smaller reduction in void volume fraction compared to the plain woven case.

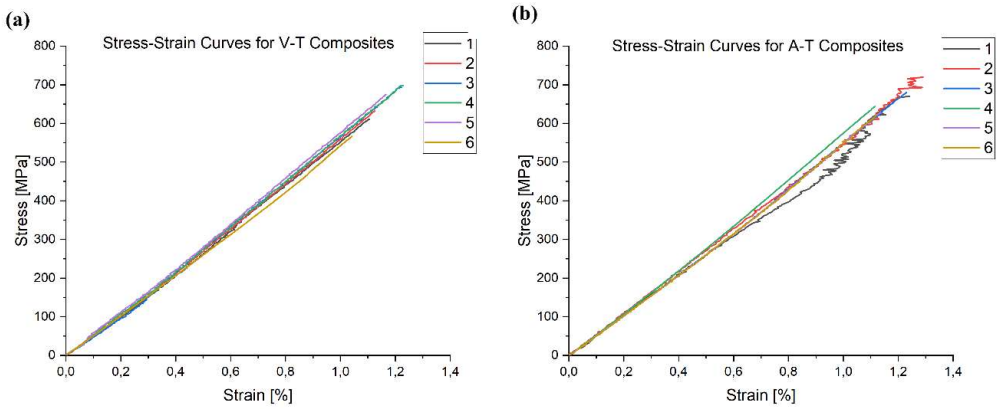


Figure 3-14: Stress-strain curves for twill woven composites (a) vacuum oven cured, (b) autoclave cured

3.3.3 Flexural Properties of Composites

This section presents the results of three-point bending tests conducted at the coupon level. Differences in the flexural properties of composites due to varying curing techniques are discussed. For all sets of composites, eight coupons are tested, as described in Section 2.4.3. For plain woven composites, the results of flexural tests are given in Tables 3-12 and 3-13 for vacuum oven and autoclave curing, respectively.

Table 3-12: Three-point bending test results for vacuum oven cured plain woven composite

V-P	Maximum Force [N]	Maximum Flexural Stress [MPa]	Maximum Displacement [mm]	Flexural Modulus [GPa]	Slope of Load-Displacement Curve [N/mm]
1	1126.1	627.8	3.10	35.9	447.2
2	1074.9	621.8	3.28	35.9	469.1
3	1060.0	605.6	3.10	37.4	493.4
4	1082.8	624.8	3.25	34.3	469.7
5	1048.0	599.2	3.04	35.0	486.1
6	1036.3	593.9	2.82	36.4	484.3
7	1061.2	606.3	2.88	36.3	482.4
8	1100.1	631.8	3.20	37.4	491.0
Average	1073.7	613.9	3.08	36.1	477.9
SD	27.2	13.4	0.16	1.0	14.3
CoV [%]	2.5	2.2	5.04	2.7	3.0

Table 3-13: Three-point bending test results for autoclave cured plain woven composite

A-P	Maximum Force [N]	Maximum Flexural Stress [MPa]	Maximum Displacement [mm]	Flexural Modulus [GPa]	Slope of Load-Displacement Curve [N/mm]
1	1093.9	684.4	3.44	38.3	445.7
2	1077.2	685.1	3.60	38.0	425.7
3	970.8	639.6	3.70	37.7	402.6
4	997.9	682.0	3.35	39.4	398.5
5	974.5	638.7	3.36	38.5	414.3
6	1046.6	642.0	3.30	37.0	439.4
7	977.7	674.1	3.63	40.1	397.4
8	1012.6	689.8	3.49	41.2	413.8
Average	1018.9	666.9	3.48	38.8	417.2
SD	45.1	21.2	0.14	1.3	17.1
CoV [%]	4.4	3.2	3.90	3.34	4.11

The results show improvements of 8.6%, 13.0%, and 7.5% in maximum flexural stress, maximum displacement, and flexural modulus, respectively, despite decreases in maximum force and slope of load-displacement curve. The

improvement in mechanical properties with lower forces can be attributed to the reduced thickness of laminates, consequently the coupons, when cured in autoclave. Autoclave-cured specimens exhibited a 6.4% decrease in thickness for plain woven composite laminates. These findings confirm that curing woven composites in autoclave improves flexural properties even when using an out-of-autoclave prepreg.

For twill woven composites, results of flexural tests are given in Tables 3-14 and 3-15 for vacuum oven and autoclave curing, respectively. The increases in maximum flexural stress, maximum displacement, and flexural modulus for this case are 3.5%, 11.8%, and 2.9%, respectively. Similar to the tensile test results, the improvements in mechanical properties are less pronounced than those observed in plain woven laminates. This is again attribute to the smaller difference in void percentage between V-T and A-T laminates.

Table 3-14: Three-point bending test results for vacuum oven cured twill woven composites

V-T	Maximum Force [N]	Maximum Flexural Stress [MPa]	Maximum Displacement [mm]	Flexural Modulus [GPa]	Slope of Load-Displacement Curve [N/mm]
1	1179.5	754.2	3.10	45.5	586.1
2	1163.0	732.2	2.91	43.2	574.7
3	1189.0	760.0	3.01	44.4	576.4
4	1234.2	768.7	2.44	44.1	595.1
5	1185.7	737.3	2.87	43.3	586.3
6	1245.5	824.8	3.17	46.7	572.8
7	1186.0	730.2	2.82	43.2	593.2
8	1234.9	789.9	3.07	43.9	568.3
Average	1202.2	762.2	2.92	44.3	581.6
SD	29.0	30.3	0.21	1.2	9.3
CoV [%]	2.4	4.0	7.34	2.6	1.6

Table 3-15: Three-point bending test results for autoclave cured twill woven composites

A-T	Maximum Force [N]	Maximum Flexural Stress [MPa]	Maximum Displacement [mm]	Flexural Modulus [GPa]	Slope of Load-Displacement Curve [N/mm]
1	1094.4	790.9	3.41	46.3	504.5
2	1131.6	814.1	3.35	46.3	510.2
3	1137.2	756.2	3.12	44.2	546.6
4	1084.7	781.6	3.39	46.6	511.5
5	1146.2	795.0	3.20	46.7	538.9
6	1173.0	772.0	3.16	44.2	554.9
7	1197.3	792.8	3.23	43.5	541.6
8	1117.7	810.9	3.30	46.7	505.9
Average	1135.3	789.2	3.27	45.6	526.7
SD	35.3	18.0	0.10	1.3	19.3
CoV [%]	3.1	2.3	3.08	2.8	3.7

3.3.4 Rheological Behavior of Composites

The thermomechanical behavior of the manufactured laminates is analyzed using rotational rheometer under torsion loading with temperature as decribed in the Experimental Work section. The primary goal of this analysis is to ensure laminates are fully cured and meet the glass transition temperature (Tg) and shear modulus requirements specified in the manufacturer technical data sheet. A similar trend is observed for all laminates as shown in Figure 3-15. In the plot, *G'*, *G''*, and *tanθ* represent the storage (elastic) modulus, loss (plastic) modulus, and their ratio, respectively. A *tanθ* value smaller than 1 indicates an elastic response. Tg is measured by drawing two parallel lines to linear regimes of the graph and the temperature value where two lines intersect is called glass transition temperature. *Tg* is determined to be around 90°C, which does not align with the material technical data sheet with expected value of 100°C. Sudden drop in storage modulus in low temperatures are generally not expected. This may be due to test fixture is not completely cooled down to room temperature at the start of the test and specimen is

exposed to higher temperatures than the desired values and it may be the fact behind the lower Tg value than the expected one.

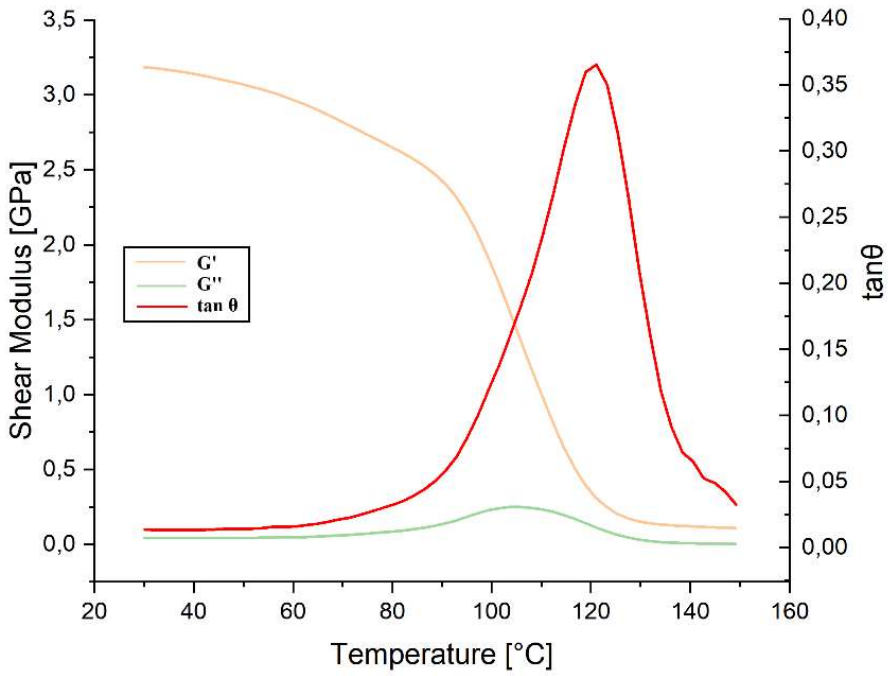


Figure 3-15: Typical thermomechanical response of composite laminates in rotational rheometer.

CHAPTER 4

MODELING, SIMULATIONS AND VALIDATION

In this thesis, modeling and simulation studies are performed on composite laminates in a multi-scale framework. The elastic properties of four different laminates are predicted using micromechanical modeling. Two different approaches are employed, as described earlier. The first approach involves mean-field homogenization with the Mori-Tanaka scheme to analytically calculate the elastic properties, while the second approach utilizes finite element homogenization of composite laminates.

Both techniques are implemented using the commercial software Digimat, an integrated environment that enables the construction of representative volume elements, assignment of necessary material properties, application of desired boundary conditions, and post-processing of simulation results. Specifically, the Digimat-MF and Digimat-FE modules are utilized for the analytical and numerical approaches, respectively. This section outlines the modeling steps and discusses simulation results for the laminate composites, specifying both inputs and outputs. The inputs are sourced from technical data sheets, as well as the microstructural characterization and mechanical tests detailed in the Experimental Work section. Naming and labeling of the material types are same with the one in the Experimental Work and Results and Discussion sections.

- **V-P**: **V**acuum oven cured **p**lain woven fabric/epoxy composite
- **V-T**: **V**acuum oven cured **t**will woven fabric/epoxy composite
- **A-P**: **A**utoclave oven cured **p**lain woven fabric/epoxy composite
- **A-T**: **A**utoclave oven cured **t**will woven fabric/epoxy composite

4.1 Procedure for Mean Field Homogenization Technique

For this technique, a mechanical analysis type is selected, as coupled analysis is not required. Mean field homogenization using the Mori-Tanaka scheme is chosen for reasons outlined in the Introduction section. Other homogenization schemes, such as Double inclusion and Taylor, could also be employed, however since it is known that M-T scheme offers several advantages such as accuracy, computational efficiency and versatility, it is chosen over its competitors. A total unitless time interval of 1 is used, with a minimum unitless time increment of 0.005 and a maximum unitless time increment of 0.1 for this analysis. Additional integration parameters are given in Appendix B.

The analysis procedure begins with identifying the constituent materials. The composites used in this study are composed of two materials: epoxy and carbon. Their respective material models and parameters are given in Table 4-1.

Table 4-1: Material models and parameters for analysis

Properties	**Epoxy**	**Carbon Fiber**
Constitutive model	Elastic	Elastic
Symmetry	Isotropic	Transversely isotropic
Density [g/cm^3]	1.19	1.78
Poisson's ratio	0.375	0.2
Axial Young's modulus [GPa]	3.45	240
In-plane Young's modulus [GPa]	3.45	15
Transverse shear modulus [GPa]	1.25	8.96
Transverse Poisson's ratio	0.375	0.33

After determining the material properties, the next step involves generating the microstructure. This requires various geometrical and dimensional information data, which are obtained from SEM and optical microscopy images of different cross-sections. To define the 2D fabric microstructure, the yarn and matrix phases are first identified. While matrix identification is achieved through material assignment, yarn

identification is more complex and requires both geometrical and material property inputs. Yarn properties are also computed in this step.

Input parameters for computing yarn properties include yarn material, linear density or filament count, fiber diameter, yarn height, and yarn width. Using this data, the yarn properties are determined. Following this step, the microstructure generation takes place. To accurately create the microstructure in the representative volume element (RVE), a 2D woven fabric model is used. In this stage, the fabric weave pattern is constructed using the software interface, with parameters such as warp yarn count per unit length, weft yarn count per unit length, yarn spacing ratio, and yarn crimp provided as inputs.

All these parameters are derived from microstructural investigations and are tabulated in the Results and Discussion section. The yarn spacing ratio (YSR), defined as the distance between warp and weft yarns, is illustrated in Figure 4-1 and ranges between 0 and 1. The micrographs show that warp and weft yarns have no clearance between them. Therefore, for all MFH analysis, the YSR value is set to 0.

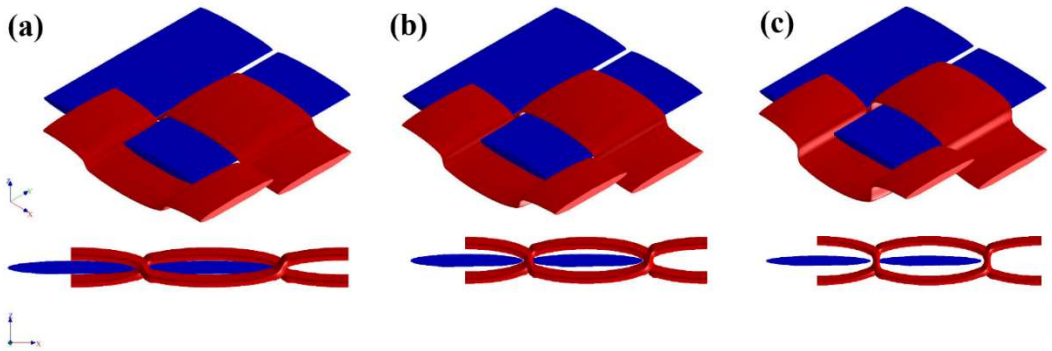


Figure 4-1: Isometric and cross section view with varying yarn spacing ratio. (a) YSR is 0, (b) YSR is 0.25 (c) YSR is 0.5

The yarn crimp ratio (YCR), on the other hand, quantifies how weft and warp yarns wrap each other. A YCR value of 0 means warp yarns are perfectly linear, while weft yarns exhibit a sinusoidal behavior around them. Conversely, a value of 1 indicates that weft yarns are linear, and warp yarns follow a sinusoidal path. An intermediate value of 0.5 represents a balanced behavior, where both yarns wrap and crimp around

each other at the transition points. The third description is valid for the materials used in this study, with a YCR of 0.5. This value is used in all analyses, and the corresponding views are shown in Figure 4-2.

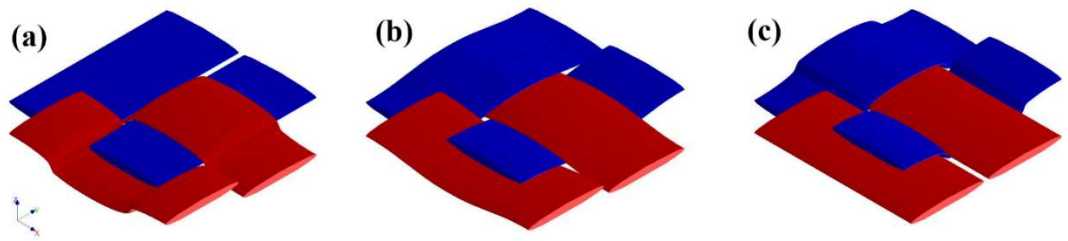


Figure 4-2: Yarn crimp ratio varying from 0 to 1. In (a), warp yarns are linear and weft yarns crimp around them (YCR=0), in (b) both warp and weft yarns crimp equally (YCR=0.5), in (c) weft yarns are linear and warp yarn crimp around them (YCR=1)

After the parameters mentioned above are input into the model and a representative unit cell is generated, the loading type and direction are identified as boundary conditions. At this stage, the pre-processing for modeling and simulation using the MFH approach is complete, and the simulations are executed. The analysis time for this approach is typically less than 1 second, with material constants computed instantly. The output includes stiffness and compliance matrices for the global material, and as well as all elastic constants.

The advantages of this approach include its robustness, and its short pre-processing time compared to competing approaches. It is also computationally more effective and requires less detailed information about the microstructure. However, because it relies on statistical averaging, this approach does not offer a detailed and highly accurate representation of material behavior. This approach may become insufficient when addressing extreme heterogeneity or when local effects are significant [48]. Additionally, it does not provide the local stress distributions in the material [49].

4.2 Procedure for Finite Element Homogenization Technique

This technique employes the well-known finite element method combined with an averaging technique to estimate the effective properties of composite materials. The finite element analysis is performed using the FE module within the Digimat software is used. This module offers capabilities for RVE generation, meshing, solving, and post-processing, providing an end-to-end solution.

The analysis begins with selecting an appropriate RVE type, either 2D or 3D. The 2D RVE type offers computational efficiency and simplicity, and for certain types of composites, it can yield satisfactory results. However, for complex structures, its simplicity may overlook critical details, making it insufficient [50, 51]. The 3D RVE type, on the other hand, is preferred for woven composite materials as it better captures the geometry and interactions within the structure. Its primary advantage over 2D RVE is its ability to represent load transfer between interlacing yarns [52]. Therefore, 3D RVE is used throughout the study, and differences between the two types are further examined at the end of this chapter.

The finite element homogenization (FEH) modeling procedure begins with the identification of material models and properties. The same inputs used in the MFH technique, as tabulated in Table 4.1, are applied here. Yarn, weave, and microstructure inputs are also consistent with the MFH approach. The primary differences lie in the generation of the generating RVE, meshing, and solving processes.

For the meshing, two options are available: non-conformal (voxel) and conformal meshes. Each method has its strengths and weaknesses. Voxel meshes offer several advantages over conformal meshes. These advantages are ease of meshing complex geometries, computational efficiency, and simpler refinement [53]. However, they can sometimes yield less accurate results due to the absence of interface nodes, which affect conformity and may reduce simulation accuracy [54]. Both meshing techniques are employed in this study, and the results are presented later.

After meshing, the loading type must be identified. For the finite element (FE) analysis, a periodic boundary condition (BC) is employed, as it generally provides more accurate predictions compared to Dirichlet and Mixed boundary conditions [55]. Periodicity can be applied in-plane or out-of-plane, generating RVEs periodically in two and three dimensions, respectively. The former is preferred for multi-layer analyses, while the latter is suited for single-layer analysis [56].

A limitation of periodic BCs is that, when used with conformal meshes, the nodes on opposite faces must align to prevent convergence issues. A schematic of periodic BCs is shown Figure 4.3, and this method is employed throughout the study.

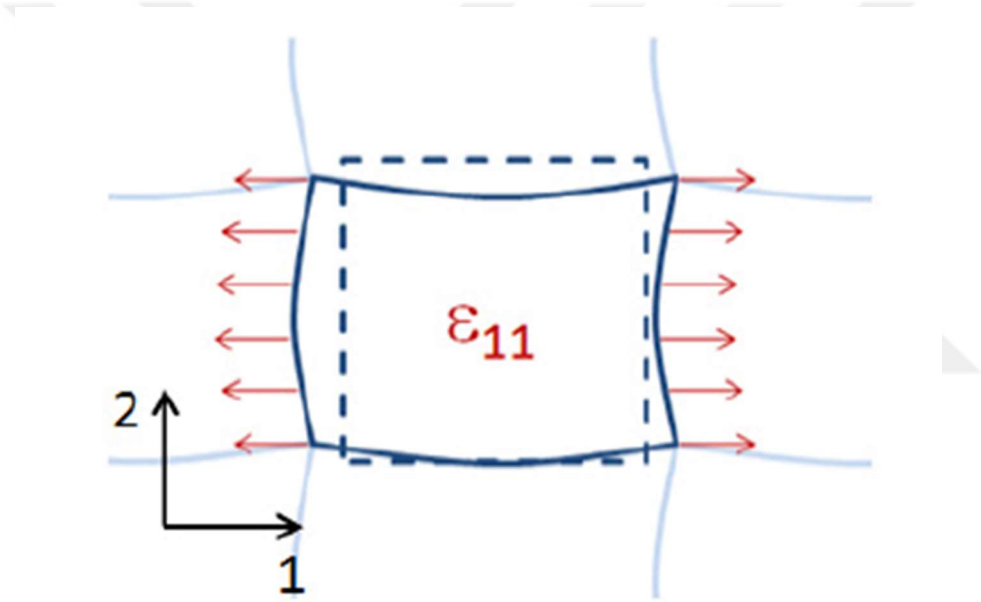


Figure 4-3: Representation of periodic BC [57]

.

Similar to MFH, FE homogenization studies provide elastic stiffness and compliance matrices, as well as all elastic material properties, as output. The main calculation logic behind FE homogenization is given in Equations 1 and 2 [58], which represent the volume averages of stresses and strains within the RVE.

$$\sigma_M^* = \frac{1}{V}\int_V \sigma_m \, dV \qquad (4-1)$$

$$\varepsilon_M^* = \frac{1}{V}\int_V \varepsilon_m \, dV \qquad (4-2)$$

Volume-averaged equations for each loading case yield six equations, which are solved to obtain the elastic stiffness matrix. In these equations, the subscripts *M* and *m* represent macro and micro properties, respectively.

4.3 Modeling and Simulation Work for Plain Woven Composites

This section presents the models, parameters, and simulation results for plain woven composites. Initially, simulations are conducted without the voids, which are subsequently included to evaluate their effects. The material properties of the constituents, epoxy and carbon fiber, are provided in Table 4-1 are consistently used throughout the modeling and simulation process. Inputs for the MFH and FEH analyses are detailed in Table 4-2.

Table 4-2: Material, yarn and geometry properties for plain woven composites

Input	Value
Material properties	Given in Table 4-1
RVE type	3D
Fabric type	2D woven
Fiber diameter	6.84 μm
Yarn height	Given in Table 3-4
Yarn width	Given in Table 3-4
Filament count	3000
Warp yarn count	5 yarns/cm
Weft yarn count	5 yarns/cm
Yarn spacing ratio	0
Yarn crimp	0.5

The difference between vacuum-oven and autoclave-cured composites, when voids are neglected, arises from yarn geometry. The woven fabric unit cell is depicted from different perspectives in Figure 4-4. First step of micromechanical modeling is to compute properties of yarn that forms woven composite material. A yarn phase is a composite material itself which consists of same matrix and fiber materials to form the woven composite material. To model the yarn phase, yarn density, which is generally expressed in tex (grams/km) or as the number of fibers in a yarn, fiber data, which is diameter of fibers which are assumed to be circular, and yarn cross-section data which is assumed to be elliptical are necessary. Based on these three inputs, it is possible to compute fiber fraction and material properties of the yarn itself using MFH tools. Computed yarn properties, dry areal weight of fiber, and unit cell sizes for both materials are presented in Table 4-3.

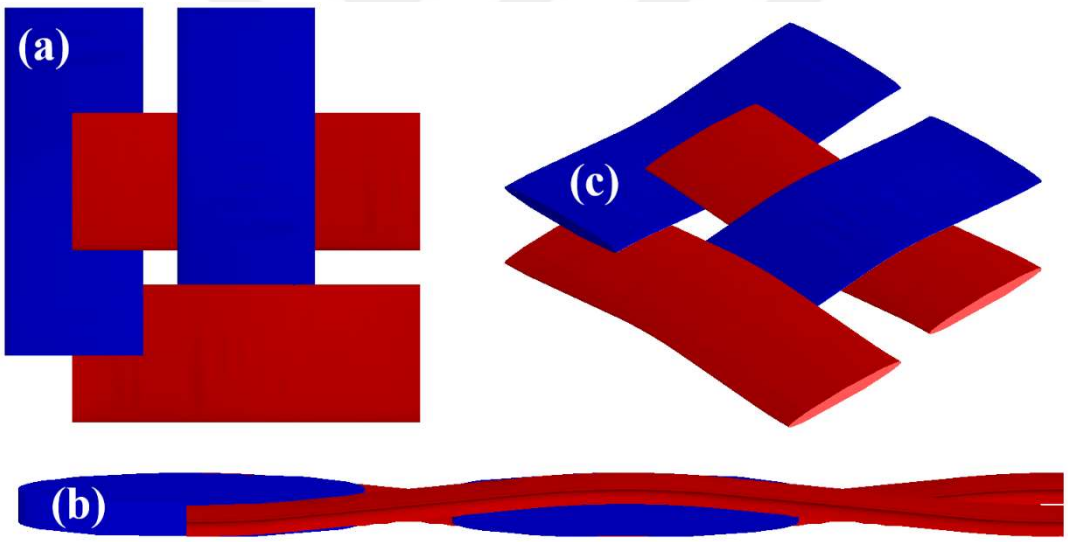


Figure 4-4: Top view (a), side view (b) and isometric view (c) of the unit cell of woven plain fabric

Table 4-3: Computed yarn properties and geometric parameters for vacuum-oven and autoclave cured plain woven composites

	V-P	A-P
RVE size [mm]	4 × 4 × 0.314	4 × 4 × 0.3
Dry areal weight [gsm]	206.2	206.2
Axial elastic modulus [GPa]	140.2	148.3
In-plane elastic modulus [GPa]	7.7	8.1
In-plane Poisson's ratio	0.436	0.423
Transverse Poisson's ratio	0.348	0.346
Transverse shear modulus [GPa]	3.2	3.4

Up to this point, the same parameters are used for both MFH and FEH simulations. While this information is sufficient to perform MFH analysis, FEH simulations requires additional steps including RVE generation and meshing steps, as mentioned earlier. For meshing the RVEs, voxel-based meshes are used by default, however, a comparison for conformal and voxel-based meshes is presented later. For voxel meshing, the unit cell is divided into 200 segments in the in-plane directions and 50 segments in the through-thickness direction. The results of MFH and FEH analysis for V-P and A-P are tabulated in Tables 4.4 and 4.5 respectively.

Table 4-4: Simulation and experimental results for V-P composite

	MFH-VP	FEH-VP (voxel)	FEH-VP (conformal)	Experimental
E_{11} [GPa]	45.98	42.88	42.81	42.0±3.0
E_{22} [GPa]	45.98	42.36	42.31	42.0±3.0
E_{33} [GPa]	7.43	7.40	7.41	-
ν_{12}	0.041	0.11	0.11	0.06±0.006
ν_{13}	0.54	0.49	0.49	-
ν_{23}	0.54	0.49	0.49	-
G_{12} [GPa]	2.56	2.34	2.34	-
G_{13} [GPa]	2.42	2.06	2.05	-
G_{23} [GPa]	2.42	2.06	2.05	-

Table 4-5: Simulation and experimental results for A-P composite

	MFH-AP	FEH-AP (voxel)	FEH-AP (conformal)	Experimental
E_{11} [GPa]	48.12	47.48	46.36	47.0±1.0
E_{22} [GPa]	48.12	47.19	45.92	47.0±1.0
E_{33} [GPa]	7.56	7.75	7.66	-
ν_{12}	0.04	0.11	0.11	0.06±0.006
ν_{13}	0.53	0.48	0.48	-
ν_{23}	0.53	0.48	0.48	-
G_{12} [GPa]	2.67	2.52	2.46	-
G_{13} [GPa]	2.46	2.21	2.11	-
G_{23} [GPa]	2.46	2.21	2.11	-

Both MFH and FEH provide a good approximation for elastic modulus predictions. For in-plane elastic properties, MFH predicts higher values for both E_{11} and E_{22} values compared to FEM predictions and experimental results. FEH simulations using voxel and conformal meshing yield very similar results. However, slight differences are observed in FEH simulations for the 1 and 2 loading directions, attributed to variations in the meshing structure for each direction.

In contrast, Poisson's ratio approximations are less accurate than those for the elastic modulus. MFH and FEH respectively underestimate and overestimate the experimental values, and neither approach provides results that closely match the measurements.

4.3.1 Implementation of Voids to Material Models

In this section, voids are incorporated into the micromechanical material models, and the results are presented. The void parameters include void volume fraction, aspect ratio distribution, and orientation, with the relevant details provided in the Results and Discussion section. The influence of void characteristics on the elastic property predictions of composite material is examined.

As previously mentioned, a two-case methodology is used to account for void orientation. In this approach, a lower bound is determined for voids oriented perpendicular to the loading direction, while an upper bound is determined for voids oriented parallel to loading directions. This methodology is employed because the voids lack a distinct orientation due to their low aspect ratios, meaning their orientation is not entirely present or meaningful within the structure. The simulation results after the incorporating voids are presented in Tables 4-6 and 4-7 for V-P and A-P composites, respectively, where deviations from experimental values are indicated in parentheses.

Table 4-6: V-P simulation results with voids included

	MFH-Lower	**MFH-Upper**	**FEH-Lower**	**FEH-Upper**	**Experimental**
E_{11} [GPa]	43.3 (+3.1%)	44.4 (+5.7%)	41.4 (-1.4%)	42.3 (+0.7%)	42.0±3.0
E_{22} [GPa]	43.3 (+3.1%)	44.4 (+5.7%)	41.2 (-1.9%)	42.1 (+0.2%)	42.0±3.0
ν_{12}	0.043 (-31.8%)	0.042 (-33.3%)	0.112 (+76.9%)	0.110 (+74.6%)	0.06±0.006
Computation Time (s)	0.006		1429		-

Table 4-7: A-P simulation results with voids included

	MFH-Lower	**MFH-Upper**	**FEH-Lower**	**FEH-Upper**	**Experimental**
E_{11} [GPa]	47.1 (+0.2%)	47.4 (+0.9%)	46.0 (-2.1%)	46.7 (-0.6%)	47±1
E_{22} [GPa]	47.1 (+0.2%)	47.4 (+0.9%)	45.9 (-2.3%)	46.5 (-1.1%)	47±1
ν_{12}	0.041 (-34.9%)	0.041 (-34.9%)	0.112 (+76.9%)	0.110 (+74.6%)	0.063±0.006
Computation Time (s)	0.006		1395		-

Both MFH and FEH approaches predict in-plane elastic modulus with very high precision; however, this accuracy does not extand to Poisson's ratio. The lower values predicted by MFH may result from simplified microstructural interactions that overlook fiber-matrix interactions. FEH, by contrast, provides a more detailed representation of geometry and structure, capturing intricate interactions. However, the complexity of the model often results in higher predicted values for Poisson's ratio. Similar trends with both MFH and FEM results are also observed in the study published by Bastovansky et al. [59].

4.3.2 Mesh Convergence Study

A mesh convergence study is conducted to evaluate the reliability of meshes used in FEH analyses. For both voxel and conformal meshes, two different mesh sizes are adapted, and results are compared for vacuum oven-cured plain woven composites. For the contact algorithm between yarns and matrix and interlacing yarns, a general contact with tangential friction coefficient of 0.1 as a default value is maintained for all finite element simulations. The applied voxel and conformal meshes are illustrated in Figure 4-5 Details about the different meshes, corresponding results, and computational times are summarized in Table 4-8.

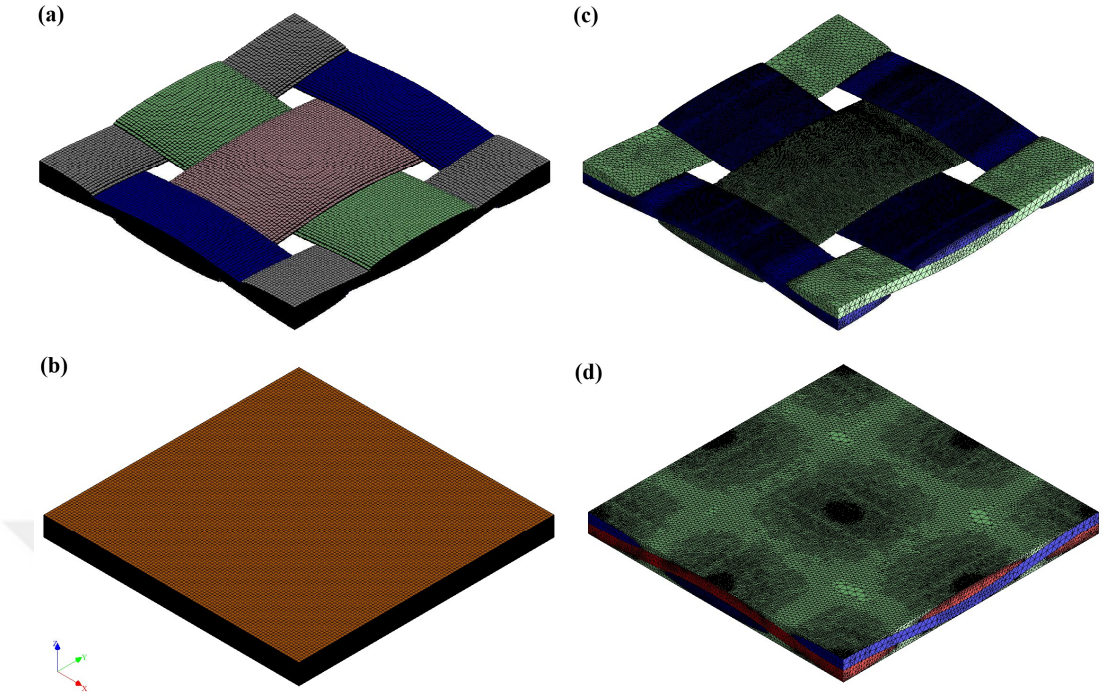


Figure 4-5: Applied meshes for the finite element analysis of V-P composite. (a) voxel meshed fiber structure without matrix (b) voxel meshed composite structure with matrix (c) conformal meshed fiber structure without matrix (d) conformal meshed composite structure with matrix

Table 4-8: Variation of mechanical properties with different meshes for V-P composites

	Element number	**E_{11} [GPa]**	**E_{22} [GPa]**	**ν_{12}**	**Computation time (s)**
Voxel - 1	500000	42.9	42.4	0.112	388
Voxel - 2	2000000	42.8	42.4	0.112	1429
Conformal - 1	343104	42.8	42.3	0.112	1312
Conformal - 2	1609492	42.7	42.3	0.112	5621

Voxel meshes employ 100x100x50 and 200x200x50 voxel structures, respectively. The analysis shows that the computed elastic properties are largely insensitive to mesh type and fineness. However, computation times are significantly influenced by the type and level of mesh detail. Voxel meshes demonstrate superior computation efficiency while maintaining accuracy in the results.

4.3.3 Three-Point Bending Simulations for Plain Woven Composites

After the orthotropic elastic properties of woven composite laminates are obtained through micromechanical models, their bending behavior is simulated using a multi-scale approach. The bending simulations are performed with Marc Mentat 2024 software [60]. An exact three-point bending test setup is modeled within the software to evaluate whether the load-displacement response from the simulations aligns with experimental results. Structural analysis is conducted under a dynamic transient load case, with a total load case duration of 125 seconds and a time step of 0.5 seconds, resulting in 250 steps. The modeled test setup for this simulation is given in Figure 4-6. The specimen, highlighted in red, is assigned an orthotropic elastic material model with properties derived from finite element homogenization micromechanical modeling. Assigned material properties for V-P and A-P composites are given in Table 4-4 and Table 4-5 and an average value of lower and upper boundaries is used for each elastic modulus, shear modulus and Poisson's ratio.

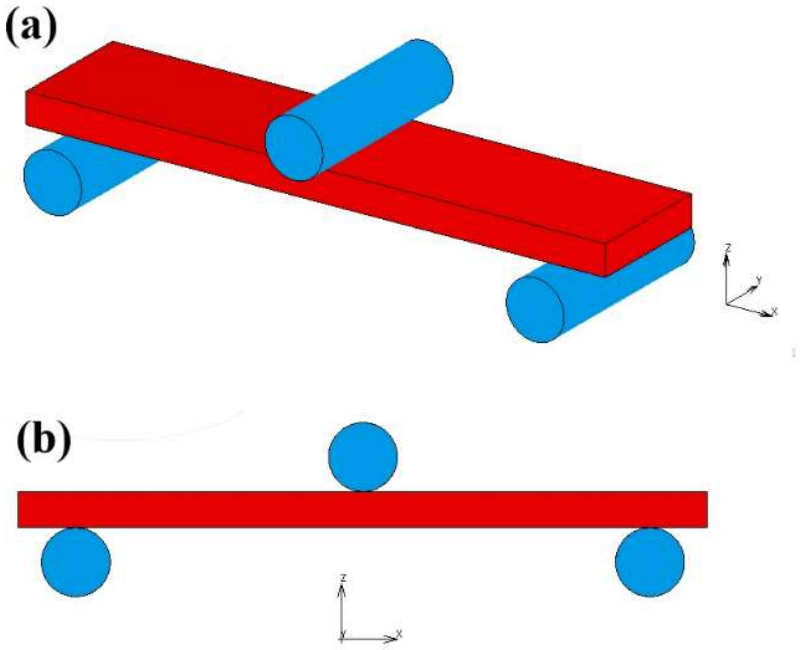


Figure 4-6: Three-point bending test simulation setup (a) isometric view (b) front view

All supports have diameters of 6 mm and they are assigned with rigid material properties, as specified ASTM D7264. The specimen dimensions for V-P composites are 13 mm in width, 60 mm in length, and 3.15 mm in thickness. For A-P coupons, the width and length remain the same as V-P, but the thickness is 2.95 mm. The lower supports are positioned 5 mm inward from the edges of the coupons, ensuring 10% offset as required by the test standard, resulting support span of 50 mm in the model. Material properties obtained from FEH micromechanical modeling and simulation work, including void implementation, are assigned to both V-P and A-P composite specimens.

Boundary conditions are applied as follows: the lower supports are fixed with zero displacement boundary conditions, while the top support is assigned an initial velocity of -1 mm/s in the z-direction to apply force and bend the specimen. All supports are modeled as rigid materials. Contact assignments are necessary in the models to define the interacting regions during the simulations and to calculate the forces generated at thes contact points. A friction coefficient of 0.3 is specified for

the contact problem, with additional testing of coefficients between 0.1 and 0.5 showing that model responses are insensitive to this parameter.

In the post-processing phase, reaction force and displacement values are extracted and compared with the experimental results. Linear tetrahedral meshes are generated using Patran software. Due to the 50000-node limit in the student version, the finest mesh structure below the threshold is utilized. The mesh is shown in Figure 4-7.

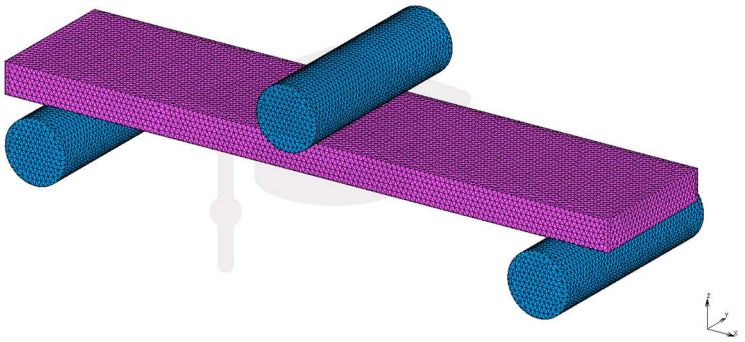


Figure 4-7: Meshed structure for three point-bending simulation of V-P

The results of three-point bending FE simulations are shown in Figure 4-8. As previously mentioned, the slopes of the computed curves are compared with the experimental slope of load-displacement curves. Slopes are computed from the region that falls into between 0.5 and 1.0 mm for displacement as in the experimental case. A linear regression is used to determine the slopes of the curves. The FE results yield slopes of 208.6 N/mm and 160.2 N/mm for V-P and A-P composites, respectively. These values are significantly lower than the experimental values, which are 477.9 N/mm and 417.2 N/mm. Some of the elastic properties obtained from micromechanical modeling studies are not validated such as E33, shear modulus values and Poisson's ratio values in 13 and 23 directions. The deviation in load-displacement curves may be due to inaccurate results from the invalidated material properties from micromechanical modeling. The resulting stress fields in the composite beam are illustrated in Figure 4-9.

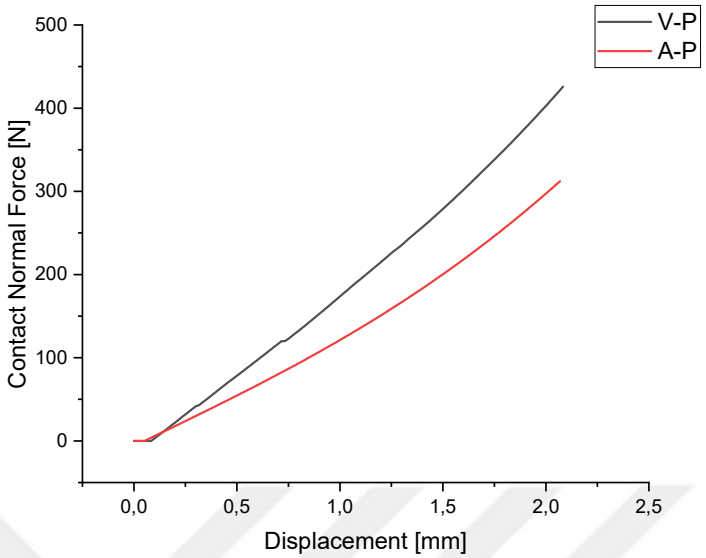


Figure 4-8: Three-point bending simulation results for plain woven composites

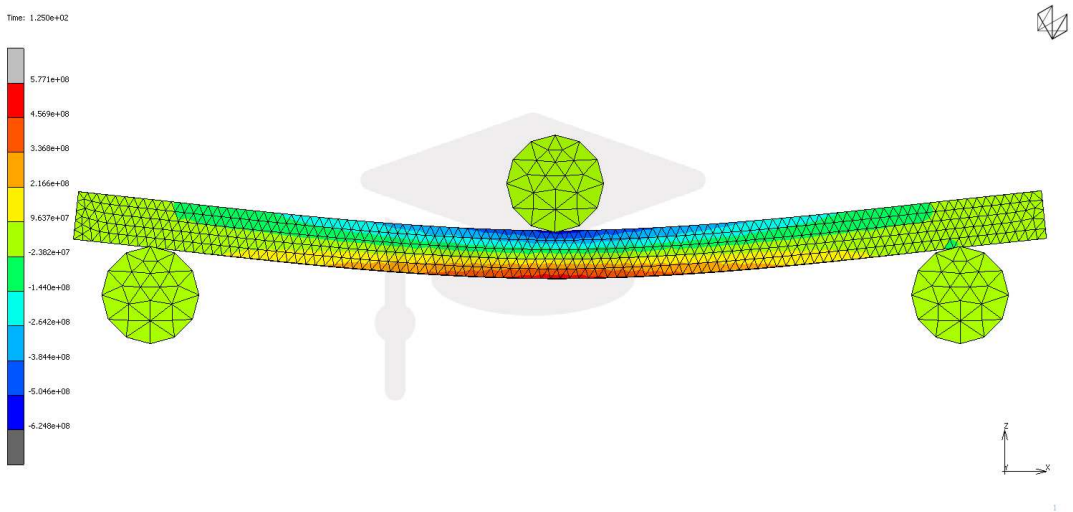


Figure 4-9: Major principal value of stress distribution in V-P composite beam

Since FE simulation results are not compatible with experimental test results, element quality is questioned and a simulation trial with linear hexahedral elements sized 0.5 mm is performed. Total displacement in this analysis is 2.08 mm. All other simulation parameters are kept constant with the first case. The slope of load and

displacement curve of this simulation is computed as 231.7 N/mm. Resulting stress fields are shown in Figure 4-10.

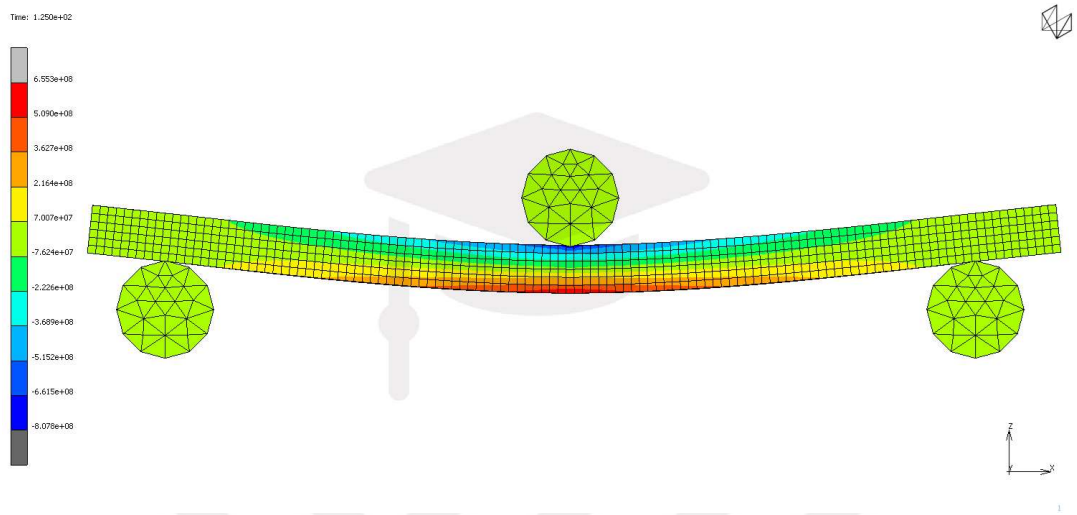


Figure 4-10: Major principle value of stress distribution in V-P composite beam with hexahedral elements

Another trial using static analysis is conducted since both transient dynamic analysis with both tetrahedral and hexahedral element types do not yield results compatible with experimental ones. For this analysis, the middle support that applys the load to the specimen is removed from the model because Marc Mentat 2024 does not support velocity boundary condition for static analyses. Instead, another boundary condition is presented into the model where a displacement is applied on to nodes in the middle sections on top surface. A total displacement of 3 mm is applied. The slope of reaction force and displacement curve is computed as 216.4 N/mm for V-P composite. The resulting value is close to the first case, which is 208.6 N/mm. The stress field in the composite specimen is shown in Figure 4-11.

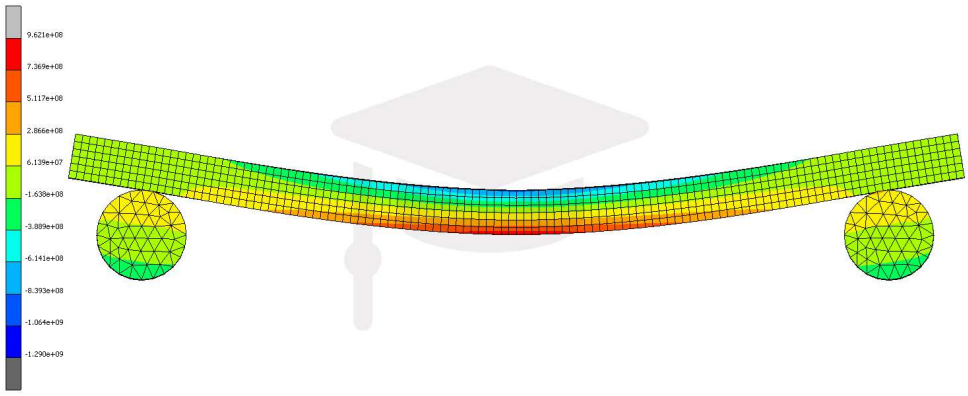


Figure 4-11: Major principle value of stress distribution for V-P composite beam in static analysis with hexahedral elements

4.4 Modeling and Simulation Work for Twill Woven Composites

This section presents models, parameters, and simulation results for twill-woven composite laminates. Like the analysis of plain woven composites, results are initially presented without void effects, followed by simulations that incorporate voids to examine their impact on mechanical property degradation. The inputs for twill-woven fabric simulations in MFH and FEH analyses are provided in Table 4-9 are utilized throughout the micromechanical modeling process.

Table 4-9: Material, yarn and geometry properties for twill woven composites

Input	Value
Material properties	Given in Table 4.1
RVE type	3D
Fabric type	2D woven
Fiber diameter	6.84 μm
Yarn height	Given in Table 3.6
Yarn width	Given in Table 3.6
Filament count	3000
Warp yarn count	5.89 yarns/cm
Weft yarn count	5.89 yarns/cm
Yarn spacing ratio	0
Yarn crimp	0.5

Woven twill fabric unit cells are illustrated in Figure 4-12. Compared to plain woven fabric, twill woven fabric features less space between yarns and a tighter structure. For twill fabric composites, the computed yarn properties, along with material and geometric specifications, are detailed in Table 4-10.

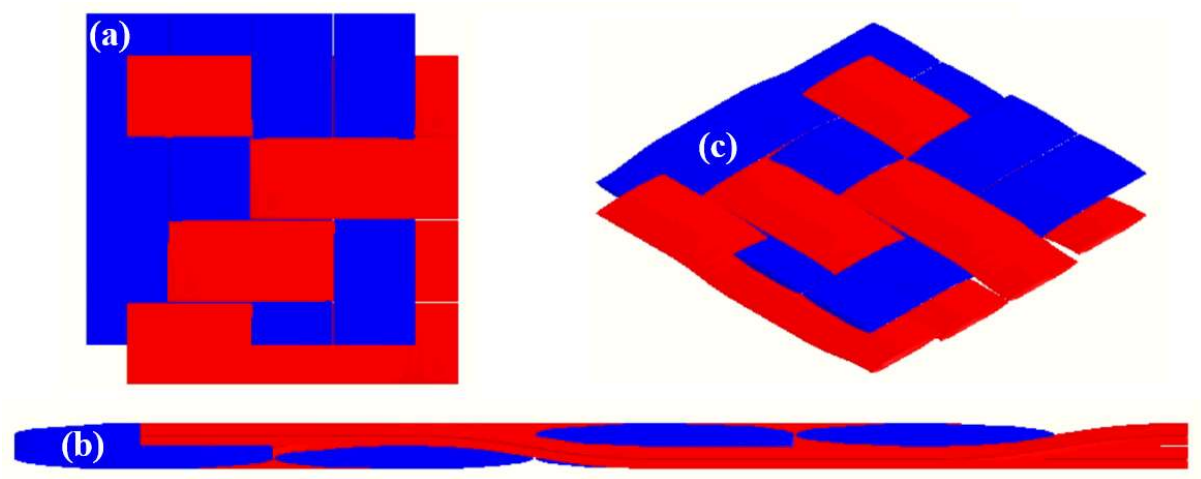


Figure 4-12: Top view (a), side view (b) and isometric view (c) of the unit cell of woven twill fabric

Table 4-10: Computed yarn properties and geometric parameters for V-T and A-T composites

	V-T	**A-T**
RVE size [mm]	6.80 × 6.80 × 0.306	6.91 × 6.91 × 0.282
Dry areal weight [gsm]	242.3	242.3
Axial elastic modulus [GPa]	138.2	146.3
In-plane elastic modulus [GPa]	7.7	8.0
In-plane Poisson's ratio	0.439	0.427
Transverse Poisson's ratio	0.348	0.347
Transverse shear modulus [GPa]	3.1	3.2

The unit cell size for A-T is 8% smaller than that of V-T, aligning with the experimental cured ply thickness measurements of real laminates. The computed dry areal weight of the fabrics is again very close to the experimental value of 245 gsm.

Computed yarn mechanical properties are used in meso-scale composite RVE simulations. Results for the V-T and A-T composites without void effects are presented in Table 4-11 and Table 4-12, respectively.

Table 4-11: Simulation and experimental results for V-T composite

	MFH-VT	**FEH-VT (voxel)**	**FEH-VT (conformal)**	**Experimental**
E_{11} [GPa]	55.2	51.1	51.4	51.7±0.8
E_{22} [GPa]	55.2	50.4	50.6	51.7±0.8
E_{33} [GPa]	8.0	7.9	8.0	-
ν_{12}	0.038	0.084	0.085	0.057±0.01
ν_{13}	0.519	0.489	0.491	-
ν_{23}	0.519	0.489	0.491	-
G_{12} [GPa]	2.82	2.59	2.63	-
G_{13} [GPa]	2.66	2.26	2.28	-
G_{23} [GPa]	2.66	2.26	2.28	-

Table 4-12: Simulation and experimental results for A-T composite

	MFH-AT	**FEH-AT (voxel)**	**FEH-AT (conformal)**	**Experimental**
E_{11} [GPa]	57.5	55.0	55.1	53.3±1.2
E_{22} [GPa]	57.5	54.2	54.3	53.3±1.2
E_{33} [GPa]	8.2	8.2	8.2	-
ν_{12}	0.037	0.079	0.078	0.056±0.01
ν_{13}	0.515	0.481	0.483	-
ν_{23}	0.515	0.481	0.484	-
G_{12} [GPa]	2.9	2.8	2.8	-
G_{13} [GPa]	2.7	2.4	2.4	-
G_{23} [GPa]	2.7	2.4	2.4	-

MFH estimations for elastic modulus are again higher than both FEH estimations and experimental results. This discrepancy arises because MFH methods cannot

accurately capture detailed local field variations within the RVE, leading to higher predicted values. Additionally, the exclusion of voids in the models contributes to higher predictions compared to experimental results for both modeling techniques. Poisson ratio estimations remain less accurate than those for elastic modulus. Similar to the plain woven case, MFH predicts lower values, while FEH predicts higher values for Poisson's ratio.

4.4.1 Implementation of Voids to Material Models

Results after the inclusion of voids are tabulated in Table 4-13 and Table 4-14 for V-T and A-T composites, respectively.

Table 4-13: V-T simulation results with voids included

	MFH-Lower	**MFH-Upper**	**FEH-Lower**	**FEH-Upper**	**Experimental**
E_{11} [GPa]	53.6 (+3.7%)	54.0 (+4.4%)	49.5 (-4.2%)	50.2 (-2.9%)	51.7±0.8
E_{22} [GPa]	53.6 (+3.7%)	54.0 (+4.4%)	49.4 (-4.4%)	50.1 (-3.1%)	51.7±0.8
ν_{12}	0.039 (-31.6%)	0.038 (-33.3%)	0.085 (+49.1%)	0.083 (+45.6%)	0.057±0.01
Computation Time (s)	0.008		1451		-

Table 4-14: A-T simulation results with voids included

	MFH-Lower	**MFH-Upper**	**FEH-Lower**	**FEH-Upper**	**Experimental**
E_{11} [GPa]	55.8 (+4.7%)	56.2 (+5.4%)	52.6 (-1.3%)	53.9 (+1.1%)	53.3±1.2
E_{22} [GPa]	55.8 (+4.7%)	56.2 (+5.4%)	52.2 (-2.1%)	53.6 (+0.6%)	53.3±1.2
ν_{12}	0.038 (-32.1%)	0.038 (-32.1%)	0.080 (+42.8%)	0.078 (+39.3%)	0.056±0.01
Computation Time (s)	0.008		1396		-

After incorporating voids, as detailed in Table 4-13 and Table 4-14, the simulation results show better alignment with the experimental results. Although the MFH still predicts slightly higher values than the experimental results, the estimations are now within a 5% margin of error. In contrast, the FEH results demonstrate excellent compatibility, falling well within the standard deviation range of the experimental elastic modulus values. However, FEH requires significantly more computational resources, with a computation time 181 times longer MFH. Additionally, FEH necessitates the creation of a refined mesh structure, which adds to its complexity. Given these factors, MFH can be considered a successful and efficient approach, especially when accounting for its underlying assumptions.

4.4.2 Three-Point Bending Simulations for Twill Woven Composites

A similar methodology to predict the flexural behavior of twill woven composites is employed, as decribed in Section 4.3.3. All aspects of the model, except the specimen geometry, material properties, and support span, remain unchanged and are not elaborated upon here. The specimen dimensions for V-T composites are 13 mm in width, 55 mm in length, and 2.83 in thickness. For A-T composites, the width and length are identical to those of V-T, but the thickness is 2.71 mm. Additionally, 5 mm clearance is present on both sides of the specimen in the width direction, resulting in a 45 mm support span between the centers. Material properties are assigned based on the results obtained from FEH with void implementation for both V-T and A-T composites.

The results of three-point bending FE simulations for twill woven composites are presented in Figure 4-13. Slopes are computed from the region that falls into between 0.5 and 1.0 mm for displacement as in the experimental case. A linear regression is used to determine the slopes of the curves. The slopes of curves are 201.39 N/mm and 197.10 N/mm for V-P and A-P, respectively. These computed values, however, do not align with the experimental results, which are 581.6 N/mm and 526.7 N/mm respectively. Some of the elastic properties obtained from micromechanical

modeling studies are not validated such as E33, shear modulus values and Poisson's ratio values in 13 and 23 directions. The deviation in load-displacement curves may be due to inaccurate results from the invalidated material properties from micromechanical modeling. The corresponding stress fields in the composite beam are illustrated in Figure 4-14.

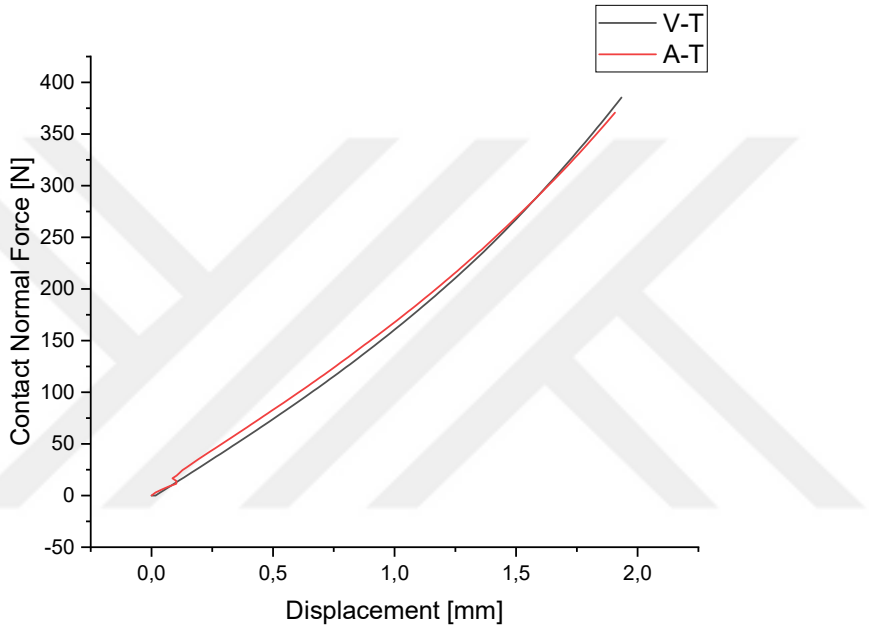


Figure 4-13: Three-point bending simulation results for twill woven composites

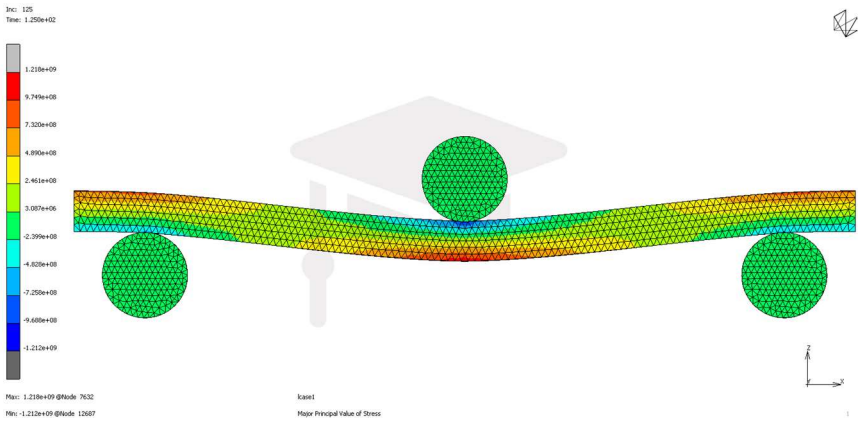


Figure 4-14: Major principal value of stress distribution in V-T composite beam

CHAPTER 5

CONCLUSION

This study focuses on the manufacturing of different woven carbon fabric/epoxy composite laminates and their micromechanical modeling using a multi-scale approach.

This study concludes that the curing technique significantly influences the final microstructure and mechanical properties of material. The effects of curing media on yarn geometry, void characteristics, and mechanical properties are analyzed. It is observed that plain woven composites are more sensitive to curing under simultaneous pressure and vacuum compared to twill woven composites. Improvements exceeding 10% are noted in the ultimate tensile strength, elastic modulus, and maximum flexural strength of plain woven composites. While twill woven composites also show improvements after autoclave curing, the magnitude of these enhancements is lower than those observed in plain woven composites.

Micro-CT scans are used to extract and analyze the void distribution, size, and shape characteristics of composite laminate. The results show that autoclave curing reduces the void fraction, increases the aspect ratio, and shrinks the voids in both plain and twill woven composites. Additionally, twill woven composites exhibit a higher quantity of voids compared to plain woven composites, but the average void size is significantly smaller. The highest volume fraction observed is in vacuum oven-cured plain woven composites, attributed to the more open structure between the yarns. The gathered void characteristics are subsequently incorporated into material models to account for the degradation in material properties caused by these voids.

It can be generally concluded that both modeling strategies, MFH and FEH, are capable of estimating the in-plane elastic modulud values of woven composites when the microstructure is accurately represented. The largest deviations from experimental values in elastic modulus are 5.7% for MFH and 4.4 for FEH, demonstrating satisfactory predictions of the effective elastic modulus for woven composites. Considering that MFH requires significantly less computation time and is less complex than FEH, it emerges as a promising alternative to the well-established finite element analysis approach.

In contrast, the estimation of in-plane Poisson's ratio using both methods is less accurate compared to their performance in predicting elastic modulus. The MFH method underestimates Poisson's ratio, with results ranging between 32.1% and 34.9% lower than experimental values. Conversely, the FEH method overestimates Poisson's ratio, with deviation ranging from 39.3% to 76.9% higher than experimental values.

A mesh convergence study is conducted using non-conforming (voxel) and conforming meshes, and the simulation results are analyzed. Both mesh types produce similar results, making voxel meshes favorable due to their easier implementation and reduced computational time.

For the three-point bending simulations, the slopes of contact normal force-displacement curves are compared with the experimental load-displacement results. While the simulation results did not closely match the experimental data, the observed trend between vacuum-cured and autoclave-cured composites are accurately computed.

REFERENCES

[1] Bacarezza, O., Abe, D., Aliabadi, M. H., & Kopula Ragavan, N. (2012). Micromechanical Modeling of Advanced Composites. Journal of Multiscale Modelling, 04(02), 1250005. doi:10.1142/s1756973712500059

[2] Structure and Properties of High-Performance Fibers. (2016). In Elsevier eBooks. https://doi.org/10.1016/c2014-0-03711-2

[3] González, C., Vilatela, J. J., Molina-Aldareguía, J. M., Lopes, C. S., & LLorca, J. (2017). Structural composites for multifunctional applications: Current challenges and future trends. Progress in Materials Science, 89, 194–251. doi:10.1016/j.pmatsci.2017.04.005

[4] Chowdhury, I. R., & Summerscales, J. (2024). Woven Fabrics for Composite Reinforcement: A Review. Journal of Composites Science, 8(7), 280. https://doi.org/10.3390/jcs8070280

[5] Kundalwal, S. I. (2017). Review on micromechanics of nano- and micro-fiber reinforced composites. Polymer Composites. doi:10.1002/pc.24569

[6] Huang, T., Wang, Y., & Wang, G. (2017). Review of the Mechanical Properties of a 3D Woven Composite and Its Applications. Polymer-Plastics Technology and Engineering, 57(8), 740–756. doi:10.1080/03602559.2017.1344857

[7] Y. Mahadik, S.R. Hallett, Finite element modelling of tow geometry in 3D woven fabrics, Composites Part A: Applied Science and Manufacturing, https://doi.org/10.1016/j.compositesa.2010.05.001.

[8] Vassiliadis, S., Kallivretaki, A., Domvoglou, D., & Provatidis, C. (2011). Mechanical Analysis of Woven Fabrics:The State of the Art. Advances in Modern Woven Fabrics Technology. doi:10.5772/25255

[9] Mirzanajotova, M. and Alieva, D. (2021). Investigation of the unevenness of the pile height length in complex fabrics. Theoretical and Practical Aspects of Modern Scientific Research 1. https://doi.org/10.36074/logos-30.04.2021.v1.49

[10] Perumalraj, R., Dasaradhan, B., & Nalankilli, G. (2010). Copper, stainless steel, glass core yarn, and ply yarn woven fabric composite materials properties. Journal of Reinforced Plastics and Composites, 29(20), 3074-3082. https://doi.org/10.1177/0731684410365007

[11] Mori, M. and Matsudaira, M. (2007), "The Effect of Weave Density on Fabric Handle and Appearance of Men's Suit Fabrics", Research Journal of Textile and Apparel, Vol. 11 No. 3, pp. 71-78. https://doi.org/10.1108/RJTA-11-03-2007-B010

[12] Alias, A. H., Paridah, M. T., Abdan, K., Sapuan, S. M., Wahab, M. S., Berkalp, Ö. B., … & Lee, S. (2018). Effects of fabric counts and weave designs on the properties of laminated woven kenaf/carbon fibre reinforced epoxy hybrid composites. Polymers, 10(12), 1320. https://doi.org/10.3390/polym10121320

[13] Subramanyam, S. P., Kotikula, D. K., Bennehalli, B., Babbar, A., Alamri, S., Duhduh, A. A., … & Kotecha, K. (2024). Plain-woven areca sheath fiber-reinforced epoxy composites: the influence of the fiber fraction on physical and mechanical features and responses of the tribo system and machine learning modeling. ACS Omega. https://doi.org/10.1021/acsomega.3c08164

[14] Sulardjaka, S., Iskandar, N., Nugroho, S., Alamsyah, A., & Prasetya, M. (2022). The characterization of unidirectional and woven water hyacinth fiber reinforced with epoxy resin composites. Heliyon, 8(9), e10484. https://doi.org/10.1016/j.heliyon.2022.e10484

[15] Kolcavová Sirková, B., Vysanska, M., & Jezik, K. (2023). Experimental study on the morphology of three dimensional multilayered interlaced basalt woven reinforcements for composites. Journal of Engineered Fibers and Fabrics, 18. https://doi.org/10.1177/15589250231214488

[16] Peirce, F. T. (1937). 5—The Geometry of Cloth Structure. Journal of the Textile Institute Transactions, 28(3), T45–T96. doi:10.1080/19447023708658809

[17] Li, M., Wang, P., Boussu, F., & Soulat, D. (2020). Effect of Fabric Architecture on Tensile Behaviour of the High-Molecular-Weight Polyethylene 3-Dimensional Interlock Composite Reinforcements. Polymers, 12(5), 1045. https://doi.org/10.3390/polym12051045

[18] Park, S. Y., Choi, C. H., Choi, W. J., & Hwang, S. S. (2018). A Comparison of the Properties of Carbon Fiber Epoxy Composites Produced by Non-autoclave with Vacuum Bag Only Prepreg and Autoclave Process. Applied Composite Materials. doi:10.1007/s10443-018-9688-y

[19] J. Schlimbach, A. Ogale, 14 - Out-of-autoclave curing process in polymer matrix composites, Editor(s): Suresh G. Advani, Kuang-Ting Hsiao, In Woodhead Publishing Series in Composites Science and Engineering, Manufacturing Techniques for Polymer Matrix Composites (PMCs), Woodhead Publishing, 2012, Pages 435-480, https://doi.org/10.1533/9780857096258.3.435.

[20] Voigt, W. (1889) Ueber die Beziehung zwischen den beiden Elasticitatsconstanten isotroper Körper, Annalen der Physik, 274, 573–587.

[21] Reuss, A. (1929). Berechnung der Fließgrenze von Mischkristallen auf Grund der Plastizitatsbedingung f¨ur Einkristalle, ZAMM — Journal of Applied Mathematics and Mechanics/Zeitschrift für Angewandte Mathematik und Mechanik, 9, 49–58

[22] S. Nemat-Nasser and M. Hori. Micromechanics: overall properties of heterogeneous solids. Elsevier Science, 1993.

[23] John Douglas Eshelby. The determination of the elastic field of an ellipsoidal inclusion, and related problems. Proceedings of the Royal Society of London. Series A, Mathematical and physical sciences, 1957, 241 (1226), pp.376-396. ff10.1098/rspa.1957.0133ff. ffhal-03619957f

[24] Digimat MF Users Manual

[25] Mori, T., & Tanaka, K. (1973). Average stress in matrix and average elastic energy of materials with misfitting inclusions. Acta Metallurgica, 21(5), 571–574. doi:10.1016/0001-6160(73)90064-3

[26] Wu, L., Zulueta, K., Major, Z., Arriaga, A., & Noels, L. (2020). Bayesian inference of non-linear multiscale model parameters accelerated by a deep neural network. Computer Methods in Applied Mechanics and Engineering, 360, 112693. https://doi.org/10.1016/j.cma.2019.112693

[27] Cai, L., Zhao, K., Huang, X., Ye, J., & Zhao, Y. R. (2020). Effective elastic modulus of foamed long glass fiber reinforced polypropylene: experiment and computation. Proceedings of the Institution of Mechanical Engineers, Part L: Journal of Materials: Design and Applications, 235(1), 202-215. https://doi.org/10.1177/1464420720958029

[28] Benveniste, Y. (1987). A new approach to the application of Mori-Tanaka's theory in composite materials. Mechanics of Materials, 6(2), 147–157. doi:10.1016/0167-6636(87)90005-6

[29] Gommers, B., Verpoest, I., & Van Houtte, P. (1998). The Mori–Tanaka method applied to textile composite materials. Acta Materialia, 46(6), 2223–2235. doi:10.1016/s1359-6454(97)00296-6

[30] Benveniste, Y., Dvorak, G. J., & Chen, T. (1991). On diagonal and elastic symmetry of the approximate effective stiffness tensor of heterogeneous media. Journal of the Mechanics and Physics of Solids, 39(7), 927–946. doi:10.1016/0022-5096(91)90012-d

[31] Ferrari, M. (1991). Asymmetry and the high concentration limit of the Mori-Tanaka effective medium theory. Mechanics of Materials, 11(3), 251–256. doi:10.1016/0167-6636(91)90006-l

[32] Suquet, P. (1985). Local and global aspects in the mathematical theory of plasticity, Plasticity Today: Modelling, Methods and Applications, 279–310.

[33] Adumitroaie, A., & Barbero, E. J. (2011). Beyond plain weave fabrics – I. Geometrical model. Composite Structures, 93(5), 1424–1432. doi:10.1016/j.compstruct.2010

[34] Kwon, J., Choi, J., Huh, H., & Lee, J. (2016). Evaluation of the effect of the strain rate on the tensile properties of carbon–epoxy composite laminates. Journal of Composite Materials, 51(22), 3197-3210. https://doi.org/10.1177/0021998316683439

[35] Zhang, H., Wang, Z., Lin, Y., & Fan, X. (2019). Hot deformation behavior of a 2024 aluminum alloy sheet and its modeling by fields-backofen model considering strain rate evolution. Metals, 9(2), 243. https://doi.org/10.3390/met9020243

[36] Chen, J., Liu, J. Y., & Ge, H. (2011). Effect of emulsifier of sizing agent on properties of sizing agent and carbon fibers. Advanced Materials Research, 306-307, 727-730. https://doi.org/10.4028/www.scientific.net/amr.306-307.727

[37] Zhang, D., Zhang, B., Shi, F., Li, M., Zhang, Z., & Gu, Y. (2011). Chemical interaction between carbon fibers and surface sizing. Journal of Applied Polymer Science, 124(3), 2127-2132. https://doi.org/10.1002/app.35226

[38] Liu, X., & Yu, W. (2018). Multiscale Modeling of Viscoelastic Behaviors of Textile Composites Using Mechanics of Structure Genome. 2018 AIAA/ASCE/AHS/ASC Structures, Structural Dynamics, and Materials Conference. doi:10.2514/6.2018-0899

[39] Misumi, J., Ganesh, R., Sockalingam, S., & Gillespie, J. W. (2016). Experimental characterization of tensile properties of epoxy resin by using micro-fiber specimens. Journal of Reinforced Plastics and Composites, 35(24), 1792–1801. doi:10.1177/0731684416669248

[40] DowAksa 3K A-38 Carbon Fiber Technical Data Sheet

[41] Umair, M., Shaker, K., Ahmad, N., Hussain, M., Jabbar, M., & Nawab, Y. (2017). Simultaneous Optimization of Woven Fabric Properties Using Principal Component Analysis. Journal of Natural Fibers, 14(6), 846–857. doi:10.1080/15440478.2017.1279994

[42] Baldua, R. K., Rengasamy, R. S., & Kothari, V. K. (2015). Effect of feed yarn parameters on air-jet textured yarn properties. Fibers and Polymers, 16(2), 463–470. doi:10.1007/s12221-015-0463-5

[43] Thomason, J. (2023). The Influence of Fibre Cross Section Shape and Fibre Surface Roughness on Composite Micromechanics. Micro, 3(1), 353-368. https://doi.org/10.3390/micro3010024

[44] Mehdikhani, M., Straumit, I., Gorbatikh, L., & Lomov, S. V. (2019). Detailed characterization of voids in multidirectional carbon fiber/epoxy composite laminates using X-ray micro-computed tomography. Composites Part A: Applied Science and Manufacturing, 105532. doi:10.1016/j.compositesa.2019.10

[45] Matsuzaki, R., Naito, M., Seto, D., Todoroki, A., & Mizutani, Y. (2016). Analytical prediction of void distribution and a minimum-void angle in anisotropic fabrics for radial injection resin transfer molding. Express Polymer Letters, 10(10), 860-872. https://doi.org/10.3144/expresspolymlett.2016.80

[46] Anda, I. R. d., Wilkins, J. W., Robinson, J. F., Royall, C. P., & Sear, R. P. (2022). Modeling the filtration efficiency of a woven fabric: the role of multiple lengthscales. Physics of Fluids, 34(3). https://doi.org/10.1063/5.0074229

[47] Chowdhury, I.R.; Summerscales, J. Cool-Clave—An Energy Efficient Autoclave. J. Compos. Sci. 2023, 7, 82. https://doi.org/ 10.3390/jcs7020082

[48] Doghri, I., Ghezal, M. I. E., & Adam, L. (2016). Finite strain mean-field homogenization of composite materials with hyperelastic-plastic constituents. International Journal of Plasticity, 81, 40-62. https://doi.org/10.1016/j.ijplas.2016.01.009

[49] Lomov, S. V., Ivanov, D., Verpoest, I., Zako, M., Kurashiki, T., Nakai, H., … & Hirosawa, S. (2007). Meso-fe modelling of textile composites: road map, data flow and algorithms. Composites Science and Technology, 67(9), 1870-1891. https://doi.org/10.1016/j.compscitech.2006.10.017

[50] Li, H., Li, S., & Wang, Y. (2011). Prediction of effective thermal conductivities of woven fabric composites using unit cells at multiple length scales. Journal of Materials Research, 26(3), 384-394. https://doi.org/10.1557/jmr.2010.51

[51] Araújo, F. C. d., D'Azevedo, E., & Gray, L. J. (2010). Boundary-element parallel-computing algorithm for the microstructural analysis of general composites. Computers &Amp; Structures, 88(11-12), 773-784. https://doi.org/10.1016/j.compstruc.2010.03.001

[52] Koumpias, A., Τσερπές, K., & Pantelakis, S. (2014). Progressive damage modelling of 3d fully interlaced woven composite materials. Fatigue &Amp; Fracture of Engineering Materials &Amp; Structures, 37(7), 696-706. https://doi.org/10.1111/ffe.12142

[53] Sartorti, R. and Düster, A. (2023). Remeshing and data transfer in the finite cell method for problems with large deformations. Pamm, 23(3). https://doi.org/10.1002/pamm.202300088

[54] Duczek, S., Duvigneau, F., Würkner, M., & Gabbert, U. (2017). The finite cell method: polygonal and tetrahedral cells. Pamm, 17(1), 295-296. https://doi.org/10.1002/pamm.201710117

[55] Biabanaki, S. and Khoei, A. (2011). A polygonal finite element method for modeling arbitrary interfaces in large deformation problems. Computational Mechanics, 50(1), 19-33. https://doi.org/10.1007/s00466-011-0668-4

[56] Jia, X., Xia, Z., & Gu, B. (2012). Micro/meso-scale damage analysis of three-dimensional orthogonal woven composites based on sub-repeating unit cells. The Journal of Strain Analysis for Engineering Design, 47(5), 313-328. https://doi.org/10.1177/0309324712444671

[57] Digimat FE Users Manual

[58] Bacarreza, O., Wen, P., & Aliabadi, M. H. (2015). Micromechanical Modeling of Textile Composites. Computational and Experimental Methods in Structures, 1–74. doi:10.1142/9781783266180_0001

[59] Bastovansky R, Smetanka L, Kohar R, Mishra RK, Petru M. Comparison of Mechanical Property Simulations with Results of Limited Flexural Tests of Different Multi-Layer Carbon Fiber-Reinforced Polymer Composites. Polymers. 2024; 16(11):1588. https://doi.org/10.3390/polym16111588

[60] Marc Mentat (Version 2024). Hexagon AB, Stockholm, Sweden, 2024.

APPENDICES

A. Statistics about void information in composite laminates

	Laminate	Mean	Standard deviation	CoV (%)	Skewness (no unit)
Semi minor axis (µm)	VT	102.8	41.7	41.4	2.9
	AT	100.8	41.5	41.2	2.8
	VP	163.1	168.2	103.1	2.9
	AP	231.4	142.7	61.7	3.2
Semi medium axis (µm)	VT	128.1	54.5	43.6	3.5
	AT	125.0	54.0	43.2	3.4
	VP	261.9	305.2	116.6	3.0
	AP	295.6	179.8	60.8	3.1
Semi major axis (µm)	VT	162.2	73.6	46.5	4.2
	AT	157.8	72.2	45.8	3.8
	VP	432.0	535.6	124.0	3.3
	AP	379.9	243.6	64.1	3.3
Volume (µm^3)	VT	518741.2	1171951.5	225.9	28.0
	AT	515537.0	1047531.8	203.2	19.0
	VP	19424315.1	62830527.9	323.5	4.5
	AP	9385492.1	27851049.4	296.7	8.2
Geometric mean of transversal semi-axes (µm)	VT	115.9	47.1	40.6	3.2
	AT	111.8	45.8	41.0	3.1
	VP	260.2	156.8	60.3	3.2
	AP	203.9	217.7	106.8	2.8
Elongation factor	VT	1.41	0.30	21.05	1.40
	AT	1.46	0.31	20.98	1.40
	VP	1.47	0.33	22.46	1.51
	AP	2.14	1.06	49.40	2.68
Cross-section roundness factor	VT	0.82	0.14	16.67	-0.40
	AT	0.82	0.14	16.62	-0.39
	VP	0.80	0.15	18.54	-0.47
	AP	0.70	0.18	26.03	-0.14

		Kurtosis	Minimum	Maximum	50%	95%
Semi minor axis (µm)	VT	15.5	30.0	660.0	80.0	170.0
	AT	14.5	30.0	630.0	80.0	180.0
	VP	9.4	40.0	1300.0	110.0	560.0
	AP	12.9	60.0	1370.0	180.0	510.0
Semi medium axis (µm)	VT	24.0	60.0	1110.0	110.0	220.0
	AT	21.8	60.0	1150.0	110.0	220.0
	VP	9.7	50.0	2250.0	140.0	950.0
	AP	11.7	90.0	1960.0	240.0	650.0
Semi major axis (µm)	VT	37.9	60.0	1870.0	140.0	280.0
	AT	27.4	60.0	1380.0	140.0	280.0
	VP	13.5	110.0	4270.0	210.0	1600.0
	AP	13.8	150.0	2680.0	300.0	833.0
Volume (µm^3)	VT	1378.3	182926.8	87050304.9	320122.0	1303353.7
	AT	563.6	182926.8	50396341.5	320122.0	1303353.7
	VP	22.9	343795.6	560257846.7	709078.4	141875834.5
	AP	112.1	1680201.6	750840100.8	2730327.6	34696163.5
Geometric mean of transversal semi-axes (µm)	VT	18.9	45.8	855.9	100.0	193.6
	AT	17.2	45.8	816.7	100.0	194.4
	VP	12.5	90.0	1638.7	207.8	583.8
	AP	8.0	44.7	1451.2	114.9	726.5
Elongation factor	VT	3.12	1.00	4.49	1.37	2.01
	AT	2.96	1.00	4.49	1.37	2.00
	VP	4.14	1.00	4.30	1.41	2.12
	AP	9.49	1.00	9.47	1.84	4.33
Cross-section roundness factor	VT	-0.52	0.23	1.00	0.82	1.00
	AT	-0.55	0.21	1.00	0.82	1.00
	VP	-0.35	0.25	1.00	0.83	1.00
	AP	-0.55	0.18	1.00	0.67	1.00

B. Integration Parameters for MFH Analyses

Time interval	
Final time	1
Maximum time increment	0.1
Minimum time increment	0.005
Homogenization scheme controls	
Relative tolerance	0.0001
Target tolerance	0.000001
Acceptable tolerance	0.00001
Maximum number of iterations	20
Number of iterations before control	20
Loading equilibrium controls	
Target tolerance	0.000001
Acceptable tolerance	0.01
Tolerance threshold	0.00001
Maximum number of iterations	20
Number of iterations before control	4
Initialization with previous step	Checked
Integration scheme	
Integration parameter	0.5
Orientation	
Number of angle incremenets	12
Tolerance on trace of orientation tensor	0.1

C. Yarn Cross Section Images

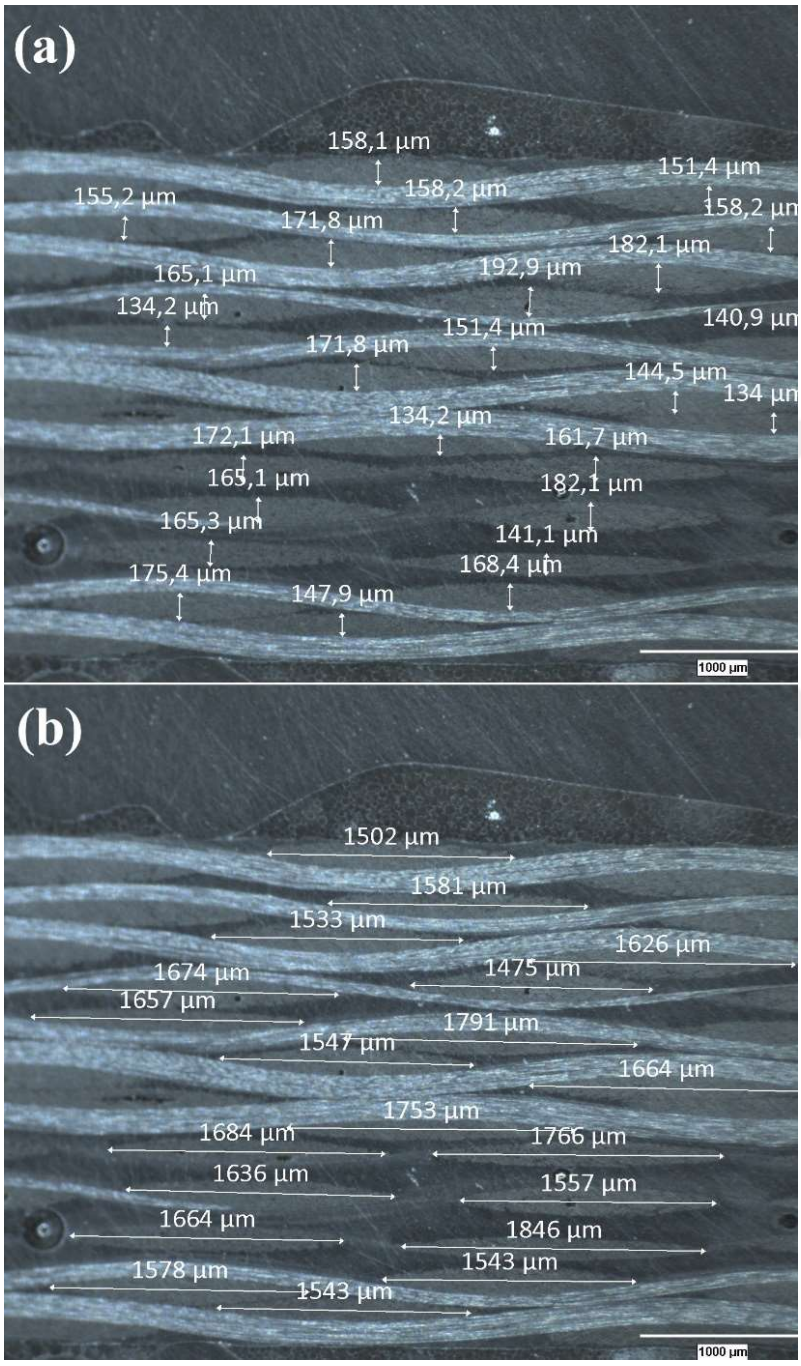


Figure 5-1: Yarn cross section images for vacuum cured plain woven composite. (a) height measurements of warp direction, (b) width measurements of warp direction

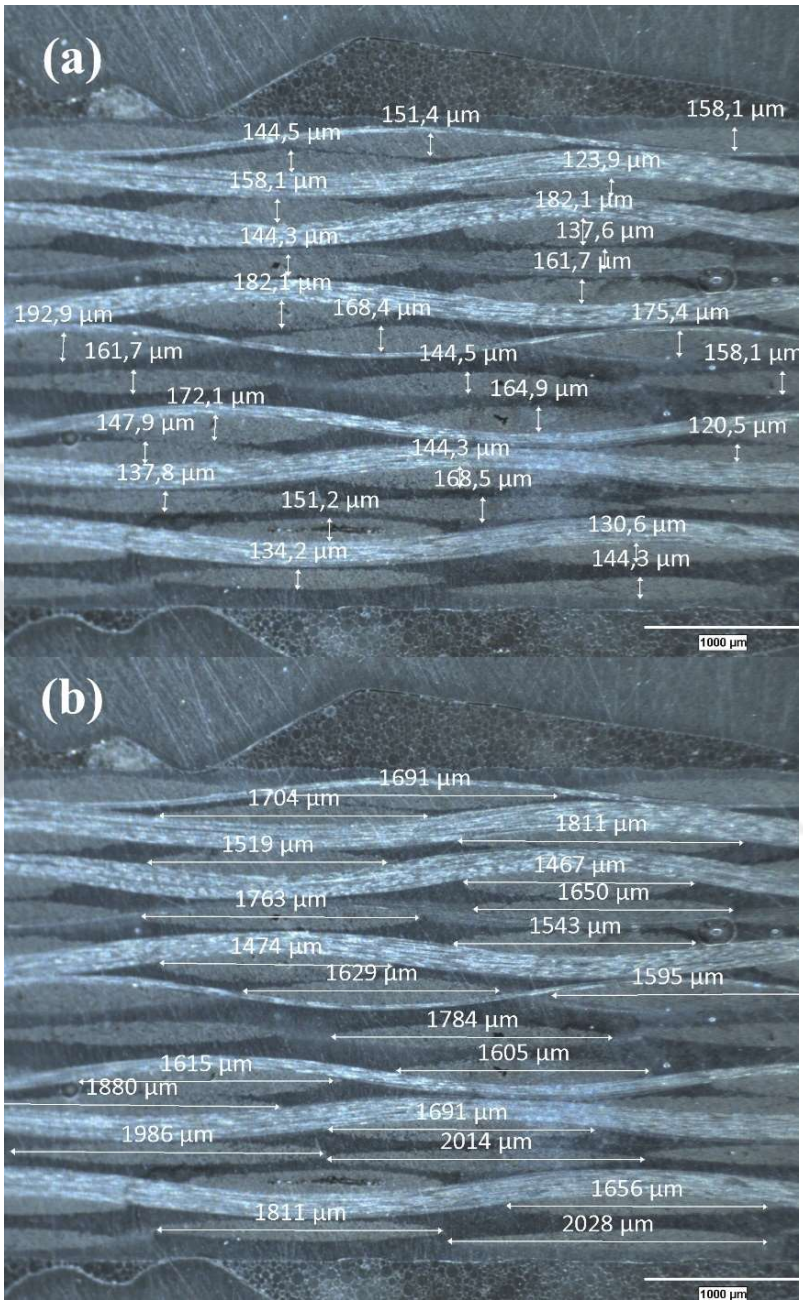


Figure 5-2: Yarn cross section images for vacuum cured plain woven composite. (a) height measurements of weft direction, (b) width measurements of weft direction.

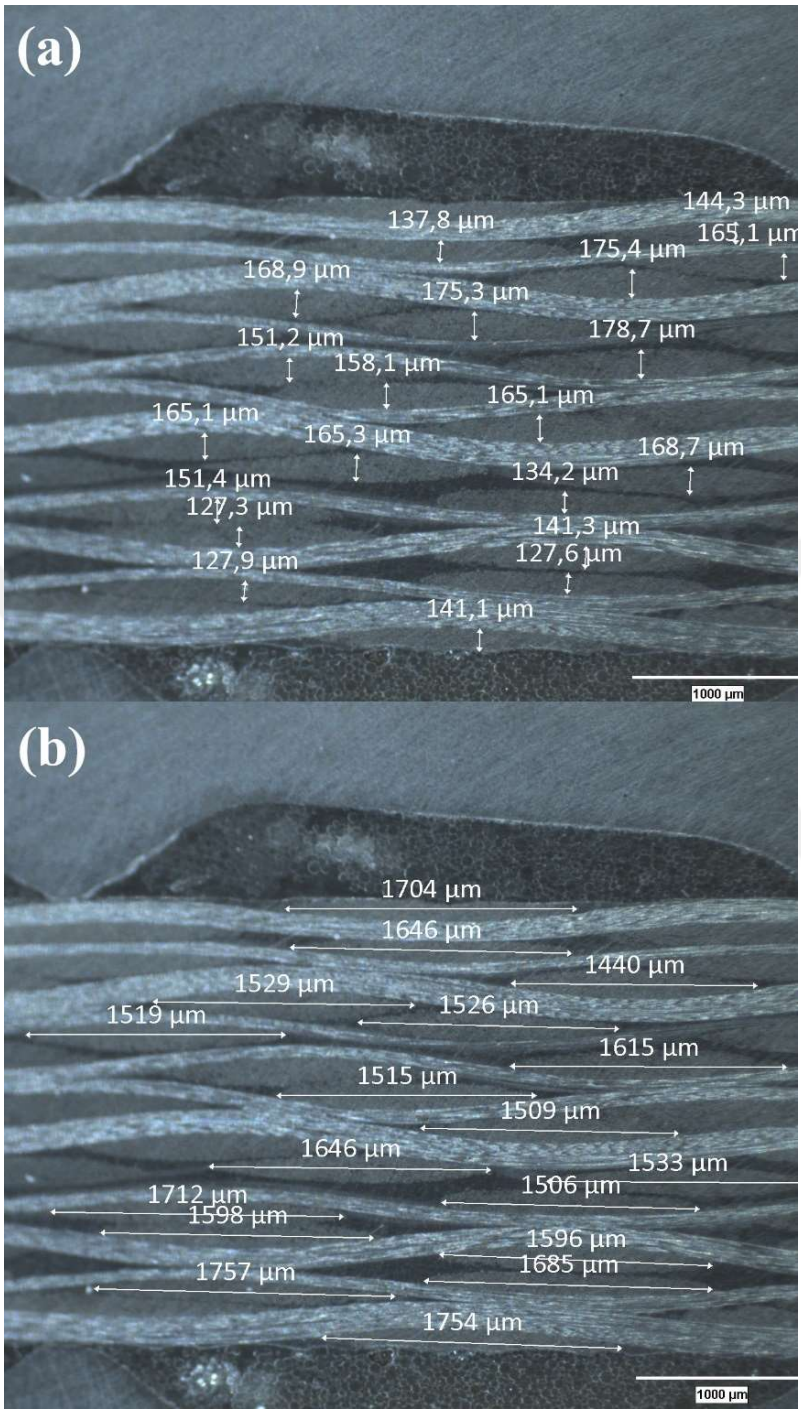


Figure 5-3: Yarn cross section images for autoclave cured plain woven composite. (a) height measurements of warp direction, (b) width measurements of warp direction

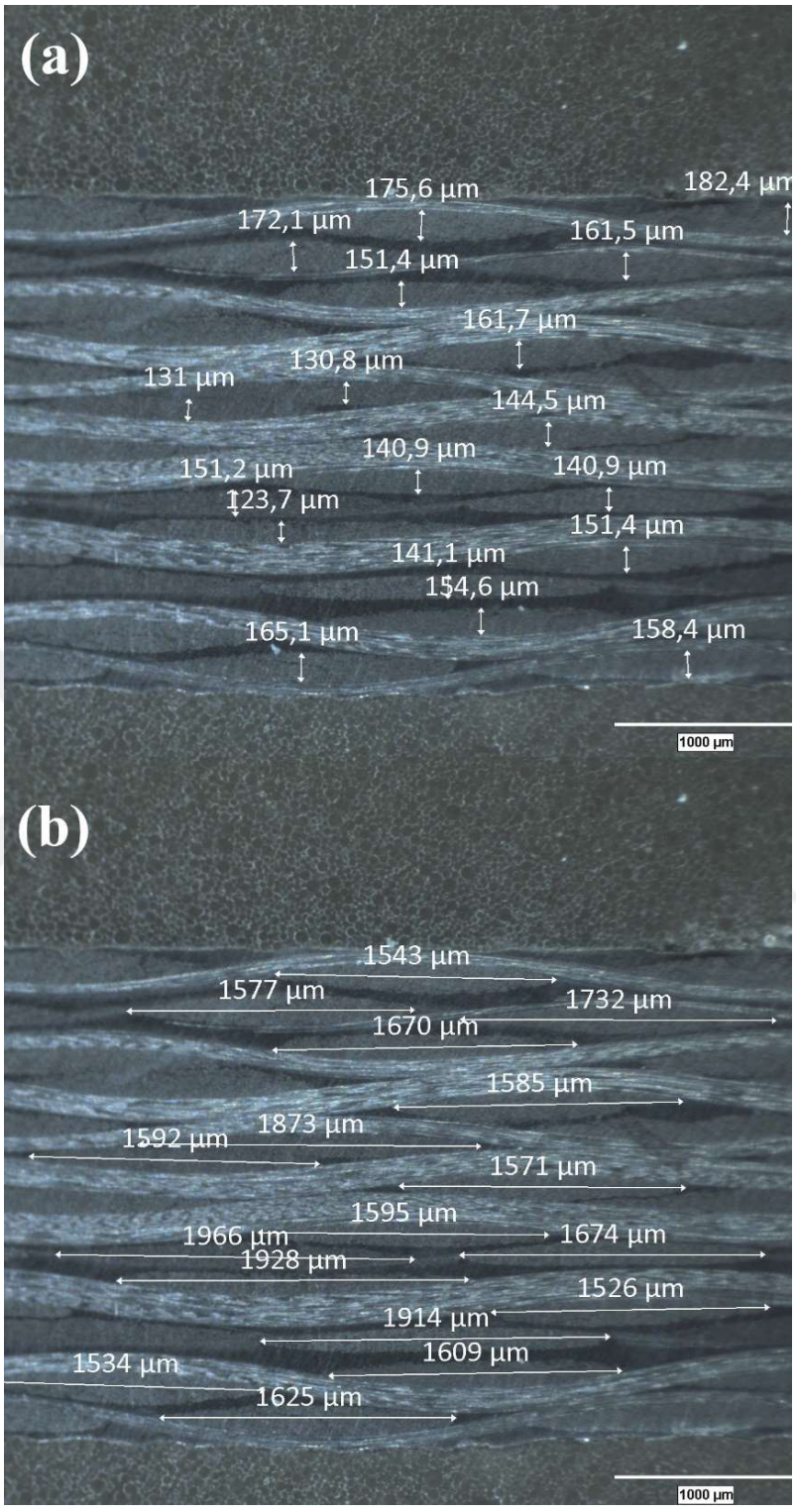


Figure 5-4: Yarn cross section images for autoclave cured plain woven composite. (a) height measurements of weft direction, (b) width measurements of weft direction.

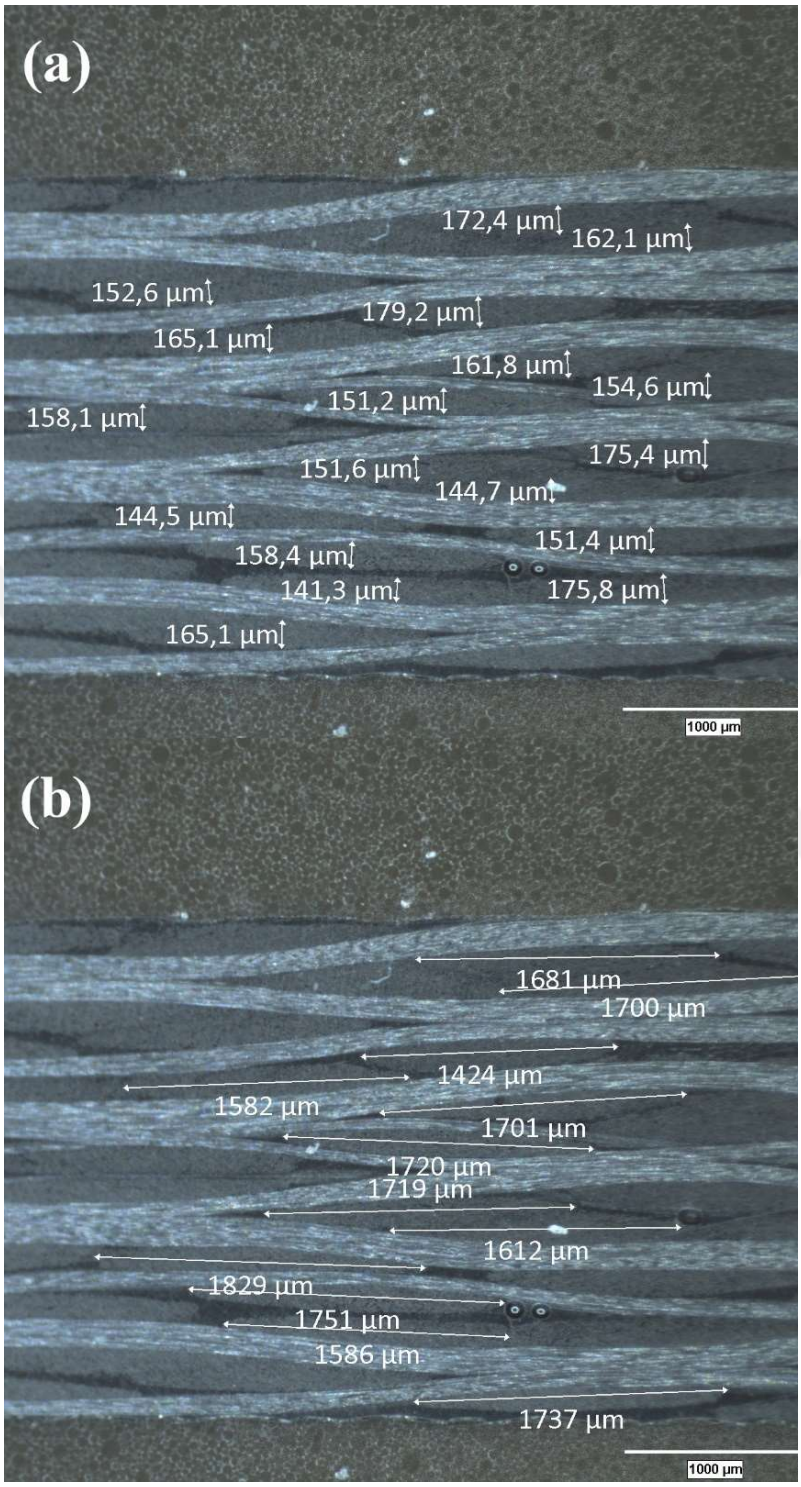


Figure 5-5: Yarn cross section images for vacuum cured twill woven composite. (a) height measurements of warp direction, (b) width measurements of warp direction

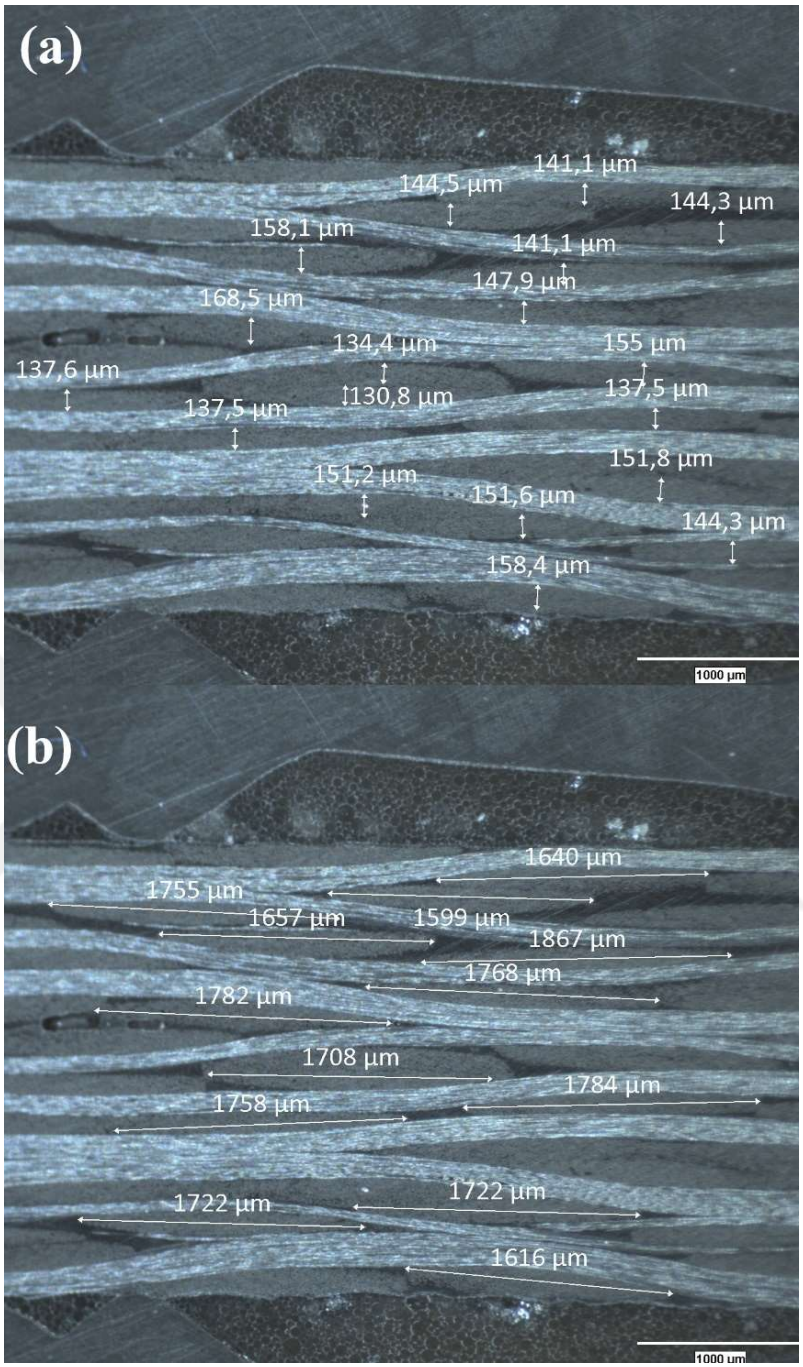


Figure 5-6: Yarn cross section images for vacuum cured twill woven composite. (a) height measurements of weft direction, (b) width measurements of weft direction.

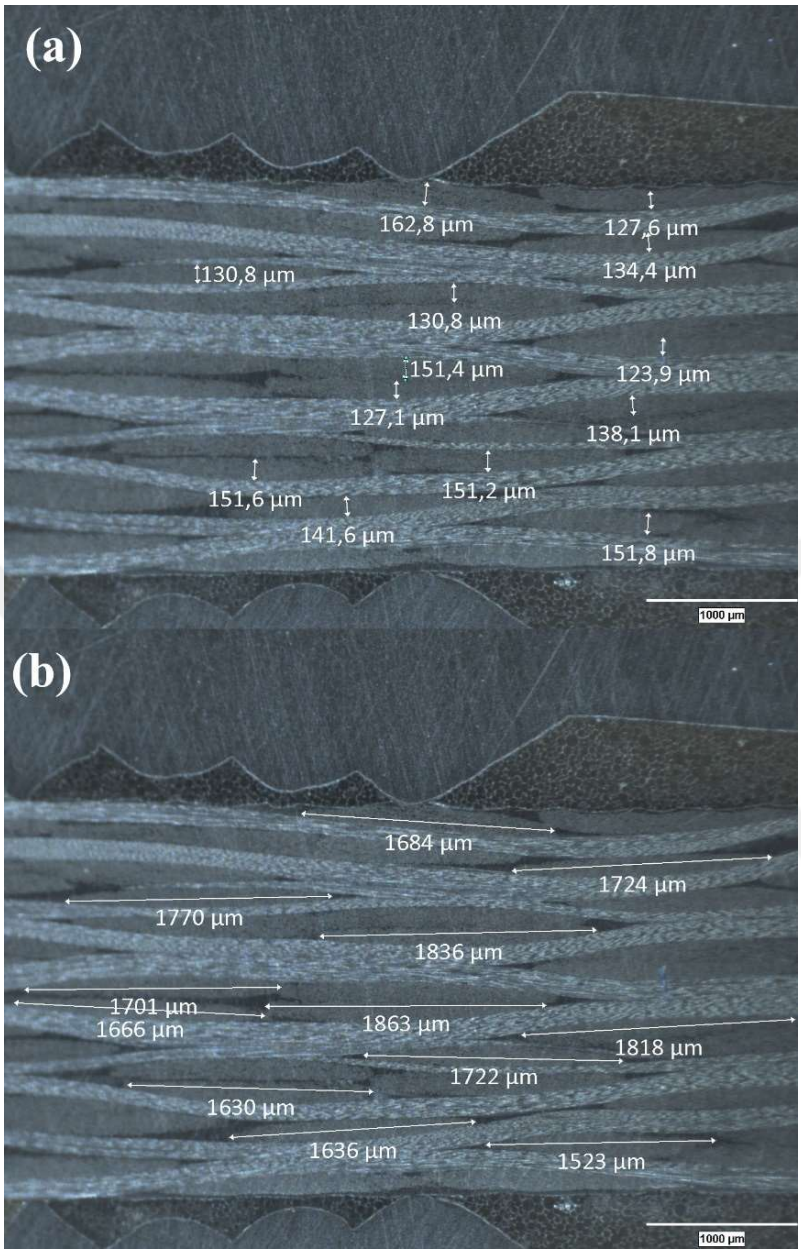


Figure 5-7: Yarn cross section images for autoclave cured twill woven composite. (a) height measurements of warp direction, (b) width measurements of warp direction

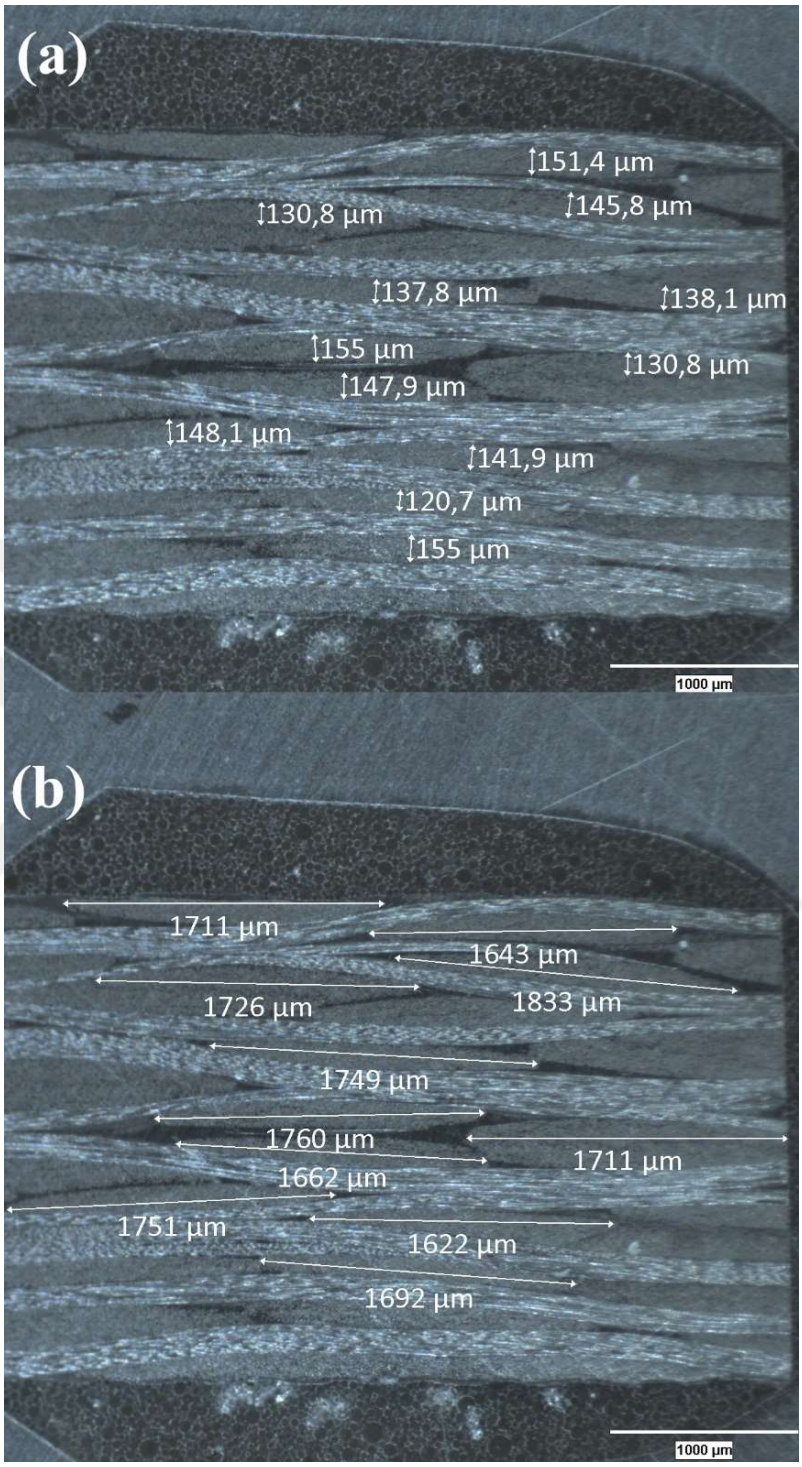


Figure 5-8: Yarn cross section images for autoclave cured twill woven composite. (a) height measurements of weft direction, (b) width measurements of weft directio